Order Number 8821630

Precision measurement of parity nonconservation in atomic cesium

Noecker, Martin Charles, Ph.D.

The University of Michigan, 1988

U·M·I

300 N. Zeeb Rd.
Ann Arbor, MI 48106

PRECISION MEASUREMENT

OF PARITY NONCONSERVATION

IN ATOMIC CESIUM

by

Martin Charles Noecker

A dissertation submitted in partial fulfillment
of the requirements for the degree of
Doctor of Philosophy
(Physics)
in The University of Michigan
1988

Doctoral Committee:

Professor John Ward, Co-Chairman
Professor Carl Wieman, Co-Chairman, The University of Colorado
Professor S. M. Blinder
Professor Yukio Tomozawa
Professor Jens Zorn

RULES REGARDING THE USE OF

MICROFILMED DISSERTATIONS

Microfilmed or bound copies of doctoral dissertations submitted to The University of Michigan and made available through University Microfilms International or The University of Michigan are open for inspection, but they are to be used only with due regard for the rights of the author. Extensive copying of the dissertation or publication of material in excess of standard copyright limits, whether or not the dissertation has been copyrighted, must have been approved by the author as well as by the Dean of the Graduate School. Proper credit must be given to the author if any material from the dissertation is used in subsequent written or published work.

Dedicated to Carol, John, and Peggy,

whose love, patience and support

have made this work possible.

ACKNOWLEDGEMENTS

I am deeply indebted to Professor Wieman for teaching me the art of experimental science. I am also grateful to Sarah Gilbert, Richard Watts, Carol Tanner, and B. Pat Masterson for the tremendous help they have given me and the things they have taught me. This work was made possible by their contributions and those of others, including David Crosby and Richard Weppner (doing the tough jobs), Gabi Weinreich (helping us gain control of the LSI computer), and numerous undergraduate assistants (doing the tedious work). I am also grateful to John Cooper for his invaluable contributions in developing an explanation of our line asymmetry.

I would like to thank Joyce Cox, my "guardian angel," for quickly and cheerfully doing the legwork I needed done in Ann Arbor. Alan Dunwell offered plenty of assistance with the JILA computer facilities as I typed most of this thesis, and Leslie Haas typed in the numerous equations that appear in this thesis. Les Thurston produced many of the figures; several others were prepared with the aid of Dana Anderson.

This work was supported by grants from the National Science Foundation and the Research Corporation.

TABLE OF CONTENTS

LIST OF TABLES

Table

LIST OF FIGURES

Figure

LIST OF APPENDICES

CHAPTER I

INTRODUCTION

This thesis describes work I performed in carrying out a high-precision measurement of parity non-conservation (PNC) arising from the weak neutral-current interaction in atomic cesium. Measurements of this effect in cesium and other atoms by other groups have been seriously limited by poor signal-to-noise ratio and systematic uncertainty. Our previous measurement of this effect was a substantial improvement over those in both respects; this work constitutes a similar advance over our previous measurement.

While making this measurement, we have discovered an interesting effect resulting from the high laser fields we use in our resonant cavity. Despite the obvious physical symmetry of our apparatus, the line shapes observed on the weak transitions we use show a striking asymmetry. This thesis will include a discussion of the tests we have made on this effect and an explanation of its origin.

The major part of this thesis will cover the parity nonconservation measurement, including a thorough study of the systematic effects considered in that measurement. Chapter One covers the history of the parity nonconservation field, presenting the general theoretical background behind atomic PNC measurements and discussing earlier experiments. Chapter Two presents a more detailed theoretical discussion of the cesium atom as a basis for studying

this experiment. Chapter Three contains a basic description of the apparatus we used in the experiment, with emphasis on the specific improvements we made since our first measurement. Chapter Four reviews the systematic effects and our approaches for reducing or eliminating them. In Chapter Five I will present the results of the measurements and discuss the implications.

The final chapter of the thesis reviews our studies of the line shape asymmetry. I present a brief background of other studies of this type of effect, the results of several different tests we performed to diagnose the effect, and our explanation of the mechanism that causes the line asymmetry.

1.1 Weak Neutral Currents in Atoms

One of the most exciting successes of modern elementary particle theory is the unification of the electromagnetic and weak interactions in the electroweak gauge theory of Weinberg, Salam, and Glashow[1]. Starting from the SU(2) × U(1) gauge symmetry, they showed that the electromagnetic and weak interactions can be expressed in terms of a weak mixing angle θ_W and four particles – the photon, the charged particles $W^{\pm}$, and the neutral Z^0. The massive W and Z particles mediate the weak charged-current and neutral-current interactions, respectively. The observation of the W and Z particles in experiments at CERN[2] marked a great success of this theory.

The electroweak theory successfully predicted the existence of weak neutral-current interactions, first observed in experiments with high-energy neutrinos[3]. Another experiment using polarized electrons

scattered off deuterium[4] demonstrated the existence of neutral-current interactions between electrons and nucleons.

Bouchiat and Bouchiat[5] proposed in 1974 that this interaction might be observable in atoms. In the non-relativistic limit, the weak neutral current interaction in an atom can be written as a perturbing hamiltonian

$$\mathcal{H}_{PNC} = \frac{G_F}{2\sqrt{2}\, m_e c}\left\{(\vec{\sigma}_e\cdot\vec{p}_e)\delta^3(\vec{r}_e)\left[C_{1P}Z + C_{1N}N\right]\right. \tag{1-1}$$

$$\left. + (\vec{p}_e - i\vec{\sigma}_e\times\vec{p}_e)\delta^3(\vec{r}_e)\cdot\left[C_{2P}\vec{\sigma}_p + C_{2N}\vec{\sigma}_N\right] + (\text{hermitian conjugate})\right\}$$

where the subscripts e, p, and n refer to the electrons, protons, and neutrons, respectively; Z and N are the numbers of protons and neutrons in the nucleus; and G_F is the Fermi coupling constant. In this expression, clearly the first term dominates; in that term, the contributions from all nucleons add directly, yielding the factors of Z and N. The four constants C_{1P}, C_{1N}, C_{2P}, and C_{2N} are empirical coupling constants with model-specific predicted values. The "weak charge" Q_W is defined as

$$Q_W \equiv 2(N\cdot C_{1N} + Z\cdot C_{1P}) \tag{1-2}$$

In the Weinberg-Salam ("standard") model, these coupling constants

are given by

$$C_{1P} = \frac{1}{2}\,(1 - 4\,\sin^2\theta_W) \qquad C_{1N} = -\frac{1}{2}$$

$$C_{2P} = +\frac{g_A}{2}\,(1 - 4\,\sin^2\theta_W) \qquad C_{2N} = -\frac{g_A}{2}\,(1 - 4\,\sin^2\theta_W) \tag{1-3}$$

where $g_A = 1.25$ is the axial vector coupling constant of β decay. These expressions show that in the electroweak theory, the neutron contribution is expected to dominate, since the currently accepted value of $\sin^2\theta_W$ is about 0.23.[6] The standard model thus predicts

$$Q_W = Z(1 - 4\,\sin^2\theta_W) - N \tag{1-4}$$

However, if the mass of the W-boson is taken as the normalization point, we get the revised weak charge value[7]

$$Q_W = Z\cdot(0.974 - 3.908\cdot\sin^2\theta_W) - N\cdot(0.974) \tag{1-5}$$

The Bouchiats also showed that this hamiltonian causes a mixing of atomic states of opposite parity. This mixing is

$$\langle n'\ell' | \mathcal{H}_{PNC} | n\ell \rangle \propto \left[R_{n'\ell'}(r) \frac{dR_{n\ell}(r)}{dr} \right] \Bigg|_{r=0} \tag{1-6}$$

Since $R_{n\ell} \propto r^{\ell} Z^{\ell+\frac{1}{2}}$ for small r, this hamiltonian only mixes S and P states, and gives a matrix element proportional to Z^2. Combining this with the factor of N multiplying C_{1N}, we find that the mixing amplitude is roughly proportional to Z^3.

Because the S and P states of the atom are no longer pure parity eigenstates, there is a small electric dipole (E1) transition amplitude between states that are nominally of the same parity. This amplitude for S states is given by

$$A_{PNC} = \langle \overline{n'S\alpha'} | -e\vec{\epsilon}\cdot\vec{r} | \overline{nS\alpha} \rangle = \sum_{n''} \left\{ \frac{\langle n'S\alpha' | \mathcal{H}^{\dagger}_{PNC} | n''P \rangle \langle n''P | -e\vec{\epsilon}\cdot\vec{r} | nS\alpha \rangle}{E_{n'S} - E_{n''P}} + \frac{\langle n'S\alpha' | -e\vec{\epsilon}\cdot\vec{r} | n''P \rangle \langle n''P | \mathcal{H}_{PNC} | nS\alpha \rangle}{E_{nS} - E_{nP}} \right\} \qquad (1\text{–}7)$$

where α and α' refer to the initial and final angular quantum numbers. The Bouchiats incorporated all of the radial integrals into a constant $E1_{PNC}$:

$$A_{PNC} = i\ \mathrm{Im}(E1_{PNC})\ \vec{\epsilon}\cdot\langle \alpha' | \vec{\sigma} | \alpha \rangle \qquad (1\text{–}8)$$

This transition amplitude is very small: the oscillator strength is about 3×10^{-22} in cesium. Thus it is impossible to observe a transition rate due only to this mixing. The Bouchiats therefore proposed that it might be possible to observe the interference between the PNC amplitude and a larger parity-conserving amplitude. In this case, a large parity-conserving amplitude would give rise to an observable steady rate with a small modulation due to interference

with the PNC amplitude:

$$R = |A_{PC} + e^{i\psi}A_{PNC}|^2 \qquad (1\text{-}9)$$
$$= |A_{PC}|^2 - 2\,A_{PC}\cdot \mathrm{Im}(A_{PNC})\cdot \sin\psi + |A_{PNC}|^2$$

in the case that the parity-conserving amplitude is pure real (note that the PNC amplitude is pure imaginary). The phase factor $e^{i\psi}$ is an experimentally arranged phase shift that brings the two amplitudes into phase so they can interfere. Since the second term is linear in A_{PNC}, it is much larger than the A_{PNC}^2 rate term, and therefore might be observable. The PNC interference term would be distinguishable from parity-conserving terms by its reversal under a parity inversion of the experiment.

This proposal initiated a large number of atomic parity non-conservation experiments attempting to measure weak neutral current effects. The early experiments gave inconclusive and conflicting results, causing a downturn in outside interest in the field. However, recent experiments have shown much better consistency. In the next section, I will summarize the current status of several of these experiments. The present experiment, by far the most precise of all, offers a serious challenge (in some measurements) to the largest accelerators available today.

1.2 Status of atomic PNC measurements

Bismuth and Lead: The first measurements of PNC in atoms were performed in bismuth (Z=83). Several groups have undertaken the

measurement of the very small optical rotation (10^{-7} radians per absorption length) that results from the interference of the PNC amplitude with the M1 amplitude. These experiments use either the $^4S_{3/2} \rightarrow {}^2D_{3/2}$ transition (876 nm) or the $^4S_{3/2} \rightarrow {}^2D_{5/2}$ line (648 nm) in a cell. A similar experiment has also been conducted in atomic lead on the J=0 → J=1 line (1.28 μm) in the 6P ground state. A summary of the results appears in Table 1.

The early bismuth results show a large scatter, even between measurements by a single group. Although most of the more recent measurements show better agreement, the Novosibirsk measurements on the bismuth 648 nm line still stand in strong disagreement with the results from other groups. In addition, theoretical predictions have varied widely from one calculation to the next, due to the complexity of the electronic structure of these atoms (there are three equivalent P electrons outside a closed shell). It may be some time before the wavefunction calculations are well understood.

Hydrogen: Hydrogen experiments offer the attractive possibility of PNC measurements in which theoretical uncertainties do not exist; however, they suffer from the great disadvantage of roughly Z^3 suppression of the PNC amplitude relative to heavier atoms. The experiments that have been constructed[8,9] recover some of that loss by using level crossings in the n=2 state at moderately high magnetic fields; this reduces the energy denominators in the perturbation expression for the PNC amplitude to near zero ($\Delta E \approx \hbar\Gamma$).

Unfortunately, the systematic contributions are enhanced by this same factor, overwhelming the PNC signal. These experiments have

Table 1

Experimental Results in Bismuth and Lead

Atom (λ)	Group	Reference	$R \equiv Im(El_{PNC})/M1 \times 10^8$
Bismuth (876 nm)	Seattle	[12] (1976)	(−8 ± 3)
		[13] (1977)	−0.7 ± 3.2
		[14] (1979)	−2.4 ± 1.4
			−10.2 ± 3.1
			−11.8 ± 3.9
			−9.8 ± 2.4
		[15] (1981)	−9.7 ± 2.5
			−10.8 ± 1.9
		[16] (1984)	−10.4 ± 1.7
	Oxford	[17] (1987)	−10.1 ± 1.0
Bismuth (648 nm)	Oxford	[12] (1976)	(+10 ± 8)
		[18] (1977)	+2.7 ± 4.7
		[19] (1981)	−9 ± 2
		[20] (1987)	−9.3 ± 1.4
	Novosibirsk	[21] (1978)	−18 ± 5
		[22] (1979)	−20.1 ± 3.2
		[23] (1980)	−20.2 ± 2.7
	Moscow	[24] (1980)	−2.3 ± 1.3
		[25] (1984)	−8.5 ± 1.5
Lead (1.28μ)	Seattle	[26] (1983)	−9.5 ± 2.6

also suffered from low signal-to-noise due to the low density of metastable atoms. To date, the results have not provided significant tests of the Weinberg-Salam theory.

Thallium and Cesium: All of these experiments observe the interference between the PNC amplitude and an induced amplitude due to the application of an external electric field. In this case, the electric field causes a small Stark-effect mixing of S and P states which then produces a small parity-conserving "Stark-induced" E1 transition amplitude between two states of the same parity. The thallium experiments use the $6P_{\frac{1}{2}} \rightarrow 7P_{\frac{1}{2}}$ transition at 293 nm, whereas the cesium experiments use the $6S_{\frac{1}{2}} \rightarrow 7S_{\frac{1}{2}}$ transition at 540 nm.

When the magnetic sublevels are not resolved, the overall rate is not affected by the PNC. The individual $\Delta m = \pm 1$ transitions are not easily resolved when the atoms are in a cell: the Doppler width is around 750 MHz in cesium and 1.6 GHz in thallium. Rather than using high magnetic fields, all of these experiments (except for ours) have observed the PNC as a polarization of the excited state due to the difference in transition rates for $\Delta m = \pm 1$ transitions. The Berkeley group has done a more recent thallium measurement[29] in high magnetic fields (4 kG) to resolve the Zeeman structure. The Paris experiment is now working with stimulated emission processes for use in the detection of the excited state polarization.[10]

Our measurements in cesium were both taken with the Zeeman structure resolved; but since our experiment uses atoms in an atomic beam, the magnetic field we need is only 74 gauss. As a result, mixing of hyperfine states by the magnetic field (which can generate

PNC-mimicking rate terms – see Section 4.3) is much smaller. Table 2 lists the measurements in cesium and thallium.

The chief benefit of using cesium and thallium is their relative simplicity among heavy atoms. Cesium has a single valence electron outside a noble-gas core; this core is much less susceptible to polarization than in lead and bismuth. As a result, theoretical calculations of the wavefunctions (necessary for the interpretation of the final results) are much less complicated. Thallium is almost as good: its valence 7P electron moves around a filled 6S shell and a noble-gas core. Unfortunately, it is not so good an approximation to ignore polarization of the 6S orbitals by the P electron; indeed, these three electrons must be treated together in many-body perturbation theory in high-precision calculations.[11]

1.3 Status of Theoretical Work

Interpretation of the experimental PNC results depends on a precise theoretical understanding of the atomic wavefunctions. The experimental result contains information on both the elementary interactions and on the atomic structure; in order to extract information about the weak neutral current interaction between the electrons and nucleons, we must use our other available knowledge of the atom to set a precise estimate of the atomic structure factors. Using the definition in Eq.1–2, we can write the matrix element of

Table 2

Experimental Results in Thallium and Cesium

Atom	Group	Reference	$Im(E1_{PNC})/\beta$ (mV/cm)
Thallium	Berkeley	[27]* (1979)	-3.2 ± 1.5
		[28]* (1981)	$-1.74 \pm 0.47\ ^{+0.20}_{-0.13}$
		[29] (1984)	$-1.73 \pm 0.26 \pm 0.07$
Cesium	Paris	[30] (1982)	$-1.34 \pm 0.22 \pm 0.11$
		[31] (1984)	$-1.78 \pm 0.26 \pm 0.12$
			$-1.56 \pm 0.17 \pm 0.12$
		[32] (1986)	-1.52 ± 0.18
	Boulder	[33] (1985)	-1.65 ± 0.13
		This work	-1.575 ± 0.033

* these values were originally measurements of $2Im(E1_{PNC})/M1$. We have scaled them by the factor $M1/\beta = -1.24(12)$ V/cm determined from Refs. [34] and [35]. The fractional uncertainties are only slightly larger than in the original results.

the first term in Eq.1–1 as

$$\frac{G_F}{4\sqrt{2}\, m_e c} \langle f|(\vec{\sigma}_e \cdot \vec{p}_e)\delta^3(\vec{r}_e) + (h.c.)|i\rangle \cdot Q_W \qquad (1\text{–}10)$$

This expression shows a clear separation of the atomic structure factor from the elementary particle theory factor Q_W.

Since the expression in Eq.1–10 (or equivalently, Eq.1–6) does not appear in the calculation of any other measurable quantity in the atom, we do not have any parity-conserving quantity (like an energy splitting) which serves as a direct measure of this atomic matrix element. Instead, experiment and theory must work together to reduce uncertainties in the relevant theoretical parameters so that an accurate determination of the PNC amplitude can be made. So, for example, measurements of S-state hyperfine splittings help determine the amplitude of the S wave-functions at the nucleus (because the hyperfine interaction is short-range). Once a set of theoretical wavefunctions are determined which accurately reproduce the experimental results, a theoretical value for the PNC amplitude can be calculated with confidence.

Early calculations of the PNC amplitudes in various atoms were crude. However, there are now several groups using sophisticated approaches to calculations of wavefunctions in atoms with many electrons. The success of calculations varies widely with the atom chosen; the results in atomic cesium are now considered accurate to within 5%, whereas the calculations in bismuth still show ±30% variations from method to method. Table 3 shows some of the predictions for $E1_{PNC}$ in cesium. We take the result of Ref. 41 as

Table 3

Theoretical PNC Values for Cesium

$\frac{E1_{PNC}}{A}$[a]	$\frac{Im(E1_{PNC})}{\beta}$[b]	Calculation Method
1.35	2.35 mV/cm	Semi-empirical; explicit sum over states[5]
1.16	2.02 mV/cm	Parametric potential[36]
1.08	1.88 mV/cm	Sum of 5 lowest states[37] } Modified Tietz potential
1.00	1.74 mV/cm	Green function[37] } Modified Tietz potential
1.06	1.84 mV/cm	Relativistic many-body perturbation theory[38]
0.97	1.69 mV/cm	Norcross potential; Green function[39]
0.90[c]	1.57 mV/cm	Relativistic MBPT[40]
0.95[d]	1.65 mV/cm	Relativistic MBPT[41]
0.935[e]	1.65 mV/cm	Semi-empirical; rescaling of hyperfine[42]

a) $A \equiv i \cdot e a_0 \cdot (-Q_W/N) \cdot 10^{-11}$
b) Using $\beta = 27.2(4)\ a_0^3$ calculated from α as given in Ref.43, and α/β as given in Refs.44-46; and using $Q_W = -71.8(1.5)$ calculated using the renormalized weak charges (Ref.7) and $\sin^2\theta_W = 0.230(5)$ from Ref.6.
c) The authors quote an uncertainty of 2%; however, this estimate is not widely accepted.
d) Quoted uncertainty: ± 5%
e) Quoted uncertainty: ± 2% (experimental) ± 3% (theoretical)

the best available prediction in cesium at this time; we use this value in the interpretation of our experimental result (Chapter 5).

Theoreticians are coming to the conclusion that cesium calculations that use the many-body perturbation approach are at the limit of their usefulness. Calculations have been completed to third order (with most of the largest fourth order terms also), but the convergence is slow. It has been shown that several terms in fourth and fifth order are of the order of 1% of the present accepted theoretical value. However, hopes are high that a new approach (coupled-cluster calculations) will achieve better than 1% accuracy.

CHAPTER II

CESIUM THEORY

In this chapter I will present the basic theoretical structure for calculation of the PNC rate term and the parity-conserving rate terms that mimic a PNC signal. First we introduce the highly-forbidden magnetic dipole amplitude, which is the largest amplitude in the absence of external fields. Then we show the much larger electric dipole amplitude induced by Stark-effect mixing in an applied DC electric field, and the tiny PNC electric dipole amplitude. Then we show the effect of Zeeman splitting of the magnetic sublevels. Then, to allow more concrete discussion of the treatment of field misalignments in Section 2.6, we first establish definitions of coordinate axes and field components in Section 2.5. Within this framework, we can calculate all of the relevant transition amplitude and rate contributions on any of the four hyperfine transitions; results are listed in Appendix C.

2.1 Magnetic Dipole Amplitude

The cesium atom energy level diagram is shown in Fig.2-1. The only stable isotope of cesium (Z=55, A=133) has a nuclear spin I=7/2; thus the 6S ground state has hyperfine levels F = 3 and 4, as does the 7S excited state. The wavelength needed for the 6S→7S transition

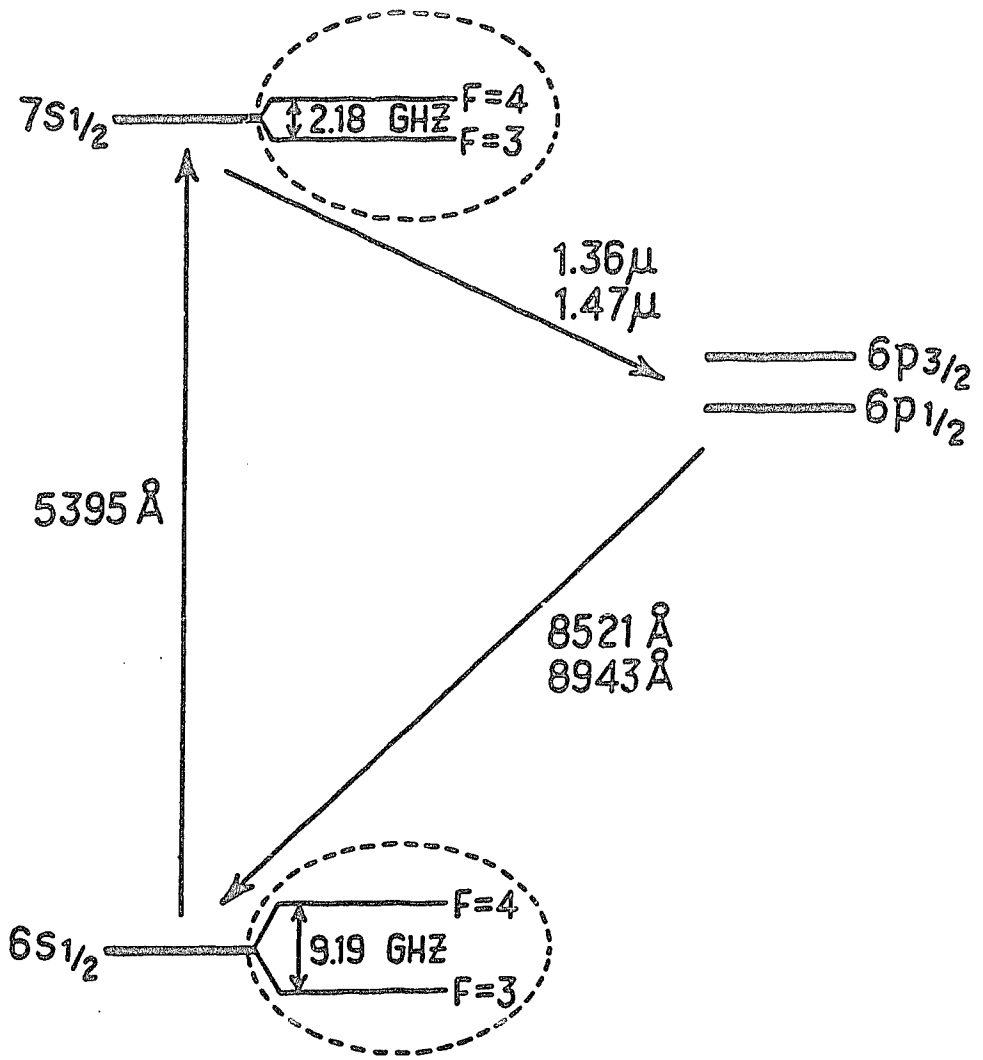

Fig.2-1. Lowest-lying S and P states in cesium. The hyperfine splitting of the S states is show on an expanded scale.

is 540 nm (green), for which we use a ring dye laser. The excited 7S state decays quickly (≈ 50 ns) through the $6P_{1/2}$ and $6P_{3/2}$ states to the 6S state, emitting two photons at 1470 nm and 852 nm ($6P_{3/2}$) or 1360 nm and 894 nm ($6P_{1/2}$). We detect the second fluorescence photon as a measure of the 6S→7S rate.

The strongest 6S → 7S transition amplitude in the cesium atom in the absence of external perturbations is a highly forbidden magnetic dipole amplitude. Since M1 transitions between states with different n are forbidden to first order, this transition amplitude is extraordinarily weak (oscillator strength ≈ 10^{-13}). This small amplitude results mostly from relativistic effects[47] and from an off-diagonal coupling of the hyperfine interaction.[5,37,48]

The oscillating magnetic field of the laser couples to the atom through the usual hamiltonian

$$\mathcal{H} = \vec{\mu}\cdot\vec{\mathcal{B}} = \frac{\mu_B}{\hbar}(\hat{L} + 2\hat{S})\cdot\vec{\mathcal{B}} \qquad (2\text{–}1)$$

where μ_B is the Bohr magneton. We must consider the matrix element

$$\langle 7SF'm'|\mathcal{H}|6SFm\rangle = \frac{\mu_B}{\hbar}\langle 7SF'm'|\hat{L} + 2\hat{S}|6SFm\rangle \cdot \vec{\mathcal{B}} \qquad (2\text{–}2)$$

For S states, this is

$$\frac{2\mu_B}{\hbar}\langle 7SF'm'|\hat{S}|6SFm\rangle \cdot \vec{\mathcal{B}} = M1\ \langle F'm'|\vec{\sigma}|Fm\rangle \cdot \vec{\mathcal{B}} \qquad (2\text{–}3)$$

where we have used $\vec{\sigma} = (2\hat{S}/\hbar)$, and we have incorporated the radial integrals into the constant M1. We are left with an expression

involving angular matrix elements of the $\vec{\sigma}$ operators – the Pauli spin matrices.

Using $\vec{\mathcal{B}} = \hat{k} \times \vec{\epsilon}$, we get the following expression for the M1 transition amplitude:

$$A_M = M1\ (\hat{k} \times \vec{\epsilon}) \cdot \langle F'm' | \vec{\sigma} | Fm \rangle \tag{2-4}$$

$$= M1(\hat{k}\times\vec{\epsilon})_z C^{F'm}_{Fm}\delta_{m,m'} + \left[d(\hat{k}\times\vec{\epsilon})_x + i(\hat{k}\times\vec{\epsilon})_y\right] C^{F'm'}_{Fm}\delta_{m,m'+d}$$

In this last step I have adopted a notation similar to Gilbert's[49]; I have also introduced the variable $d = \pm 1$ to keep track of sign reversals that depend on the sign of Δm_F. The constants $C^{F'm'}_{Fm}$ are proportional to angular matrix elements of σ_{1q}, the components of the Pauli spin operators in irreducible tensor notation:

$$C^{F'm'}_{Fm'-q} \equiv \langle F'm' | \sigma_{1q} | Fm'-q \rangle \cdot \left(\frac{1}{\sqrt{2}}\right)^{|q|} \tag{2-5}$$

where

$$\sigma_{11} = -\frac{1}{\sqrt{2}}(\sigma_x + i\sigma_y) \qquad \sigma_{1-1} = \frac{1}{\sqrt{2}}(\sigma_x - i\sigma_y) \tag{2-6}$$

$$\sigma_{10} = \sigma_z$$

These matrix elements can be calculated by a simple application of the Wigner-Eckart theorem using the rules for coupled states. The results are listed in Appendix A.

2.2 Stark-induced Amplitude

In the presence of a static electric field, the S states undergo mixing with nearby P states through the Stark hamiltonian:

$$|\overline{6S_{1/2}Fm}\rangle = |6S_{1/2}Fm\rangle + \sum_{nJF''m''} \frac{|nP_JF''m''\rangle\langle nP_JF''m''|-e\vec{E}\cdot\vec{r}|6S_{1/2}Fm\rangle}{E_{6SF} - E_{nPJ}} \tag{2-7}$$

$$\langle\overline{7S_{1/2}F'm'}| = \langle 7S_{1/2}F'm'| + \sum_{nJF''m''} \frac{\langle 7S_{1/2}F'm'|-e\vec{E}\cdot\vec{r}|nP_JF''m''\rangle\langle nP_JF''m''|}{E_{7SF} - E_{nPJ}}$$

where the bar overhead indicates a perturbed wavefunction. In a laser field, this mixing allows a "Stark-induced" transition amplitude given by

$$A_E = \sum_{nJF''m''} \left\{ \frac{\langle 7SF'm'|-e\vec{E}\cdot\vec{r}|nP_JF''m''\rangle\langle nP_JF''m''|-e\vec{\epsilon}\cdot\vec{r}|6SFm\rangle}{E_{7SF'} - E_{nPJ}} \right. \tag{2-8}$$

$$\left. + \frac{\langle 7SF'm'|-e\vec{\epsilon}\cdot\vec{r}|nP_JF''m''\rangle\langle nP_JF''m''|-e\vec{E}\cdot\vec{r}|6SFm\rangle}{E_{6SF} - E_{nPJ}} \right\}$$

Using the principle of irreducible tensor operators, Bouchiat and Bouchiat have shown[5] that this may be written

$$A_E = \vec{\epsilon} \cdot \langle 7SF'm'|\vec{r}_{eff}|6SFm\rangle \tag{2-9}$$

where the matrix elements of $\vec{r}_{eff}$, the effective dipole operator, must be of the form

$$\langle 7SF'm'|\vec{r}_{eff}|6SFm\rangle = \alpha\vec{E}\,\delta_{F,F'}\delta_{m,m'} + i\beta\langle F'm'|\vec{\sigma}\times\vec{E}|Fm\rangle \qquad (2\text{-}10)$$

In this expression, $\langle F'm'|\vec{\sigma}\times\vec{E}|Fm\rangle$ is the angular matrix element of $\vec{\sigma}\times\vec{E}$ and the constants α and β contain the radial integrals. The constants α and β are called transition polarizabilities; they correspond to the familiar scalar and tensor electric polarizabilities. Expressed in terms of reduced matrix elements and energy differences between states, these constants are[50]

$$\alpha = \frac{1}{6}\sum_{n}\left\{\langle 7S\|r\|nP_{1/2}\rangle\langle nP_{1/2}\|r\|6S\rangle\left(\frac{1}{E_{7S}-E_{nP1/2}}+\frac{1}{E_{6S}-E_{nP1/2}}\right)\right. \qquad (2\text{-}11)$$

$$\left. -\langle 7S\|r\|nP_{3/2}\rangle\langle nP_{3/2}\|r\|6S\rangle\left(\frac{1}{E_{7S}-E_{nP3/2}}+\frac{1}{E_{6S}-E_{nP3/2}}\right)\right\}$$

$$\beta = \frac{1}{6}\sum_{n}\left\{\langle 7S\|r\|nP_{1/2}\rangle\langle nP_{1/2}\|r\|6S\rangle\left(\frac{1}{E_{7S}-E_{nP1/2}}-\frac{1}{E_{6S}-E_{nP1/2}}\right)\right. \qquad (2\text{-}12)$$

$$\left. +\frac{1}{2}\langle 7S\|r\|nP_{3/2}\rangle\langle nP_{3/2}\|r\|6S\rangle\left(\frac{1}{E_{7S}-E_{nP3/2}}-\frac{1}{E_{6S}-E_{nP3/2}}\right)\right\}$$

Then the Stark-induced transition amplitude is

$$A_E = \alpha(\vec{E}\cdot\vec{\epsilon})\delta_{F,F'}\delta_{m,m'} + i\beta(\vec{E}\times\vec{\epsilon})\cdot\langle F'm'|\vec{\sigma}|Fm\rangle$$

$$= \alpha(\vec{E}\cdot\vec{\epsilon})\delta_{F,F'}\delta_{m,m'} + i\beta(\vec{E}\times\vec{\epsilon})_z\, C_{Fm}^{F'm}\delta_{m,m'} \qquad (2\text{–}13)$$

$$+ i\beta\left[d(\vec{E}\times\vec{\epsilon})_x + i(\vec{E}\times\vec{\epsilon})_y\right] C_{Fm}^{F'm'}\delta_{m,m'+d}$$

where we have expressed the angular matrix elements of $\vec{\sigma}$ in terms of the $C_{Fm}^{F'm'}$ coefficients again.

In the absence of an external magnetic field, the spectrum of the 6S → 7S transition when A_E is the dominant amplitude contains four peaks (listed in ascending order of laser frequency):

F → F′	Rate
4 → 3	$R = \frac{21}{4}\beta^2\lvert\vec{E}\times\vec{\epsilon}\rvert^2$
4 → 4	$R = 7\alpha^2(\vec{E}\cdot\vec{\epsilon})^2 + \frac{7}{4}\beta^2\lvert\vec{E}\times\vec{\epsilon}\rvert^2$
3 → 3	$R = 9\alpha^2(\vec{E}\cdot\vec{\epsilon})^2 + \frac{15}{4}\beta^2\lvert\vec{E}\times\vec{\epsilon}\rvert^2$
3 → 4	$R = \frac{21}{4}\beta^2\lvert\vec{E}\times\vec{\epsilon}\rvert^2$

(2–14)

Since $|\alpha/\beta| \approx 10$, the $\Delta F = 0$ transition peaks are usually much larger than the $\Delta F = \pm 1$ peaks; the relative sizes of the four peaks also depend strongly on the orientation of $\vec{E}$ and $\vec{\epsilon}$.

2.3 PNC Amplitude

Eq.1–8 gives an expression for the PNC transition amplitude on the 6SFm → 7SF'm' transition peak:

$$A_{PNC} = i\,\mathrm{Im}(E1_{PNC})\,\vec{\epsilon}\cdot\langle F'm'|\vec{\sigma}|Fm\rangle \qquad (2\text{–}15)$$

$$= i\,\mathrm{Im}(E1_{PNC})\left[\epsilon_z C_{Fm}^{F'm}\delta_{m,m'} + (d\epsilon_x + i\epsilon_y)C_{Fm}^{F'm'}\delta_{m,m'+d}\right]$$

in the notation of the previous sections.

2.4 Zeeman Interaction – Weak Field Limit

The application of a small magnetic field will cause energy shifts of the various spin states as given by the standard Zeeman interaction:

$$\mathcal{H}_Z = \frac{\mu_B}{\hbar}(\hat{L} + g_S\hat{S})\cdot\vec{B} + \frac{\mu_N}{\hbar}g_I(\hat{I}\cdot\vec{B}) \qquad (2\text{–}16)$$

where μ_N is the nuclear magneton. Taking $\vec{B}$ along $\hat{z}$ and neglecting the tiny μ_N term, the first order energy shift is

$$E^{(1)} = \langle nSFm|\mathcal{H}_Z|nSFm\rangle = g_F\mu_B B_z m_F \qquad (2\text{–}17)$$

where g_F is given by

$$g_F = g_J\frac{F(F+1) + J(J+1) - I(I+1)}{2F(F+1)} \qquad (2\text{–}18)$$

For S states, $g_J = 2$; then

$$g_F = \begin{cases} +\ 1/4 & F=4 \\ -\ 1/4 & F=3 \end{cases} \qquad (2\text{–}19)$$

Thus the individual m_F levels are shifted by

$$\Delta\nu = (-1)^F \frac{\mu_B}{4} m_F B \qquad (2\text{–}20)$$

This Zeeman structure is shown on the energy level diagram in Fig.2–2. The F = 4 state splits into 9 sublevels and the F = 3 state splits into 7 (2F + 1 sublevels in each case). However, the various m_F sublevels in the F = 3 state are arranged in the opposite order from those in the F = 4 state: thus when the $|F,m_F\rangle = |4,+4\rangle$ state increases in energy, the $|3,+3\rangle$ state decreases in energy. Furthermore, the ordering of these states in energy reverses when the applied $\vec{B}$ reverses direction (since we choose to keep the +z direction fixed under a $\vec{B}$ reversal).

The effect of the Zeeman splitting on the spectrum depends on the choice of $\Delta F = 0$ or ± 1 peaks and on the orientation of the DC electric field and laser field relative to the DC magnetic field. For $\Delta F = 0$ transitions, the various m_F levels split in the same way and by the same amount in both ground and excited states; thus the separation between two states with the same m_F value does not change, regardless of the value of m_F. This means that the $\Delta m = 0$ peaks for all values of m_F fall at the same laser frequency as at zero magnetic field. Similarly, the frequency separation of two states whose m_F values differ by ± 1 will be shifted by $g_F \mu_B B[(m\pm 1)-m] = \pm g_F \mu_B B$,

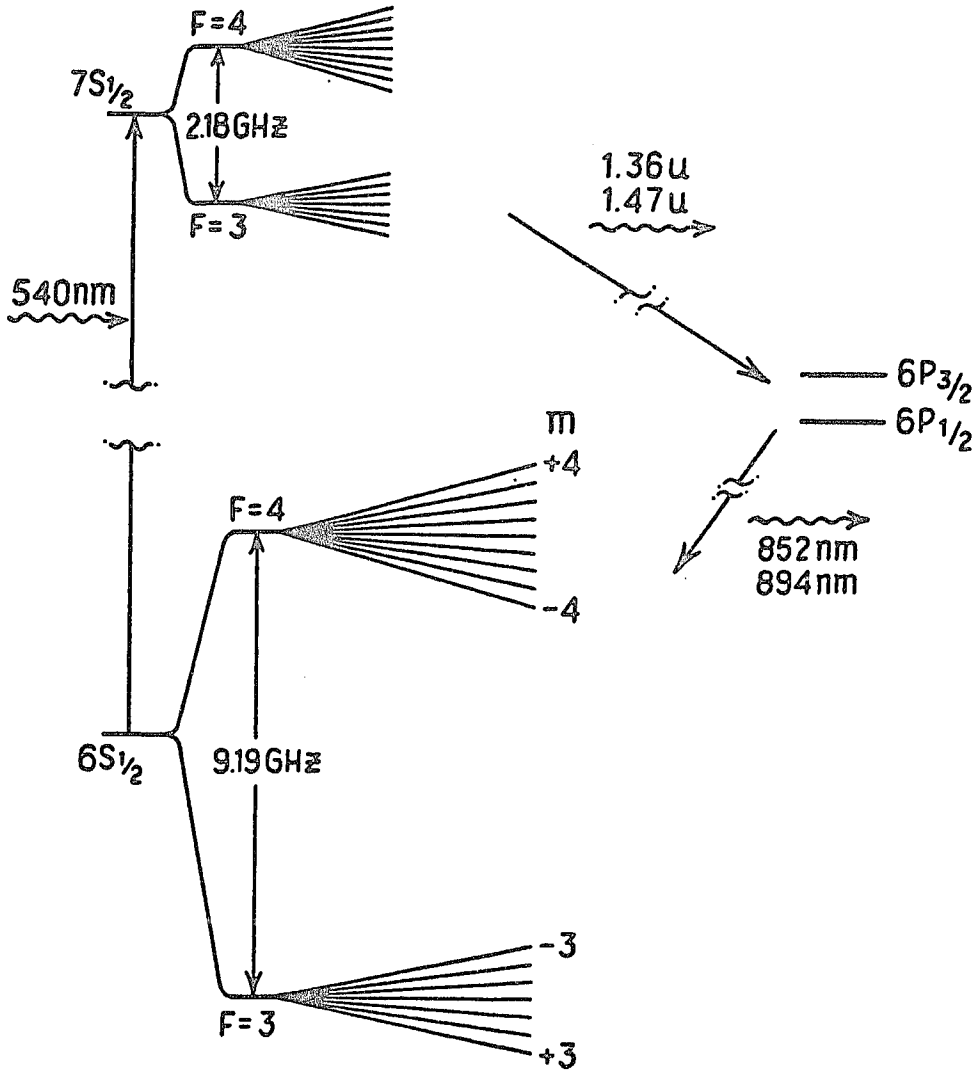

Fig.2–2. Lowest-lying S and P states of cesium, showing Zeeman structure.

independent of m_F. The resulting spectrum for a $\Delta F = 0$ transition (Fig.2–3a) has three peaks: $\Delta m = 0$ and ± 1. Since the $\Delta m = 0$ transitions can be excited through the α term in Eq.2–13 but $\Delta m = \pm 1$ transitions can only proceed through the β term, the $\Delta m = 0$ peak is generally much larger ($\alpha^2/\beta^2 \approx 100$) than the $\Delta m = \pm 1$ peaks. This ratio can be changed by selecting the angle between $\vec{\epsilon}$ and $\vec{E}$.

The $\Delta F = \pm 1$ transitions are very different. For both $\Delta F = +1$ and -1 transitions, the excited state sublevel energies shift in the opposite direction from those of the ground state. The frequency shift of the transition between $|F,m\rangle$ and $|F',m'\rangle$ is given by

$$\Delta\nu = g_{F'}\mu_B Bm' - g_F\mu_B Bm = -g_F\mu_B B(m' + m) \qquad (2-21)$$

where we have used $g_{F'} = -g_F$. In this case (Fig.2–3b), the seven transitions corresponding to $\Delta m = +1$ and the seven corresponding to $\Delta m = -1$ lie at eight evenly spaced positions separated by $2|g_F\mu_B B|$. While the outermost two peaks are caused by only a $\Delta m = +1$ or -1 transition, the six inner peaks have both $\Delta m = +1$ and -1 rate contributions. There are also seven peaks in between the $\Delta m = \pm 1$ peaks, corresponding to $\Delta m = 0$ transitions. In all cases, the frequency spacing between any two peaks is an integer multiple of $g_F\mu_B B$.

In our specific field configuration, the fact that $\epsilon_y = 0$ means that the $\Delta m = 0$ transition amplitude is zero to first order. Thus the $\Delta m = \pm 1$ peaks dominate in the actual experimental spectrum of the $\Delta F = \pm 1$ transitions (Fig.2–4b). There is another effect that induces a small $\Delta m = 0$ amplitude which is visible in Fig.2–4b; we will

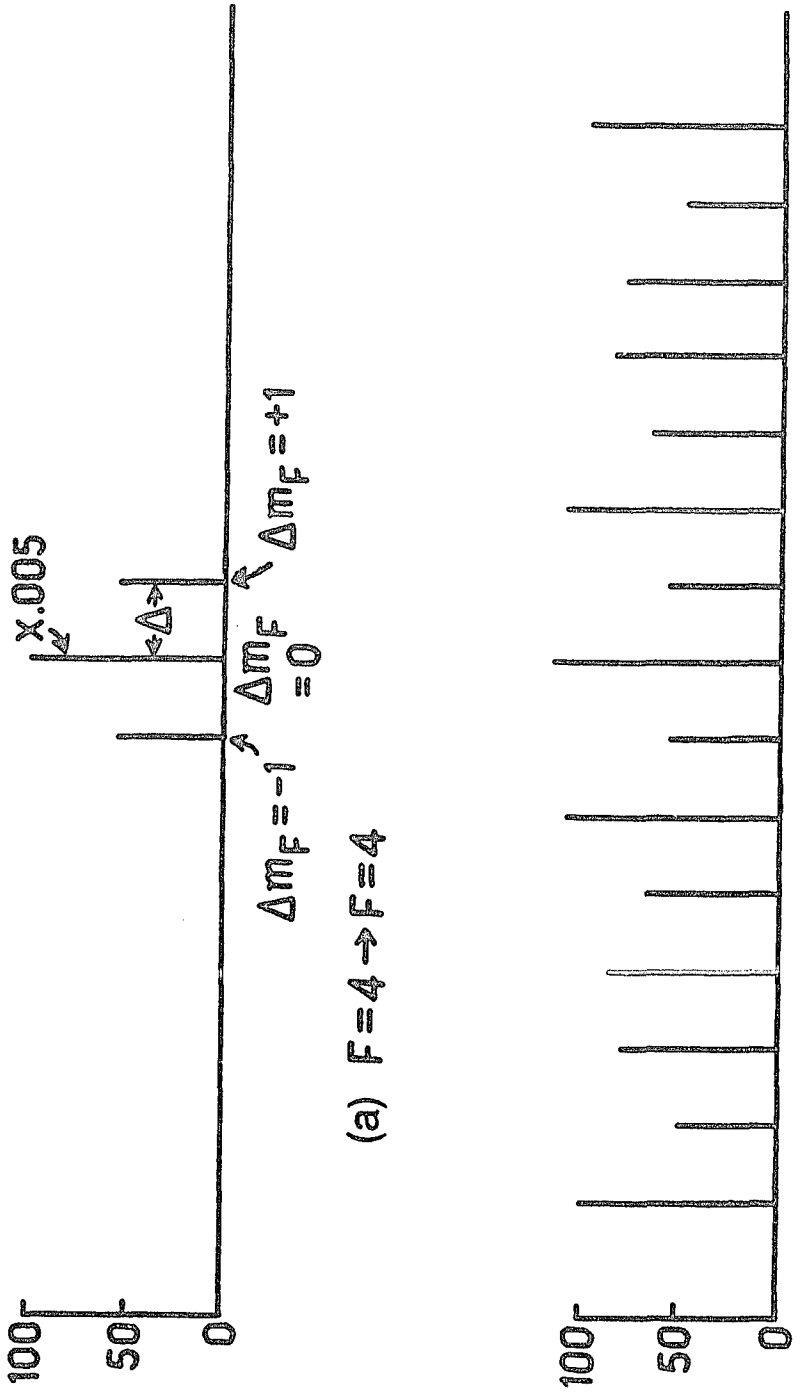

Fig.2-3. Theoretical spectra of (a) $\Delta F = 0$ and (b) $\Delta F = \pm 1$ transitions in a magnetic field. Note that the central peak in (a) is shown on a reduced scale.

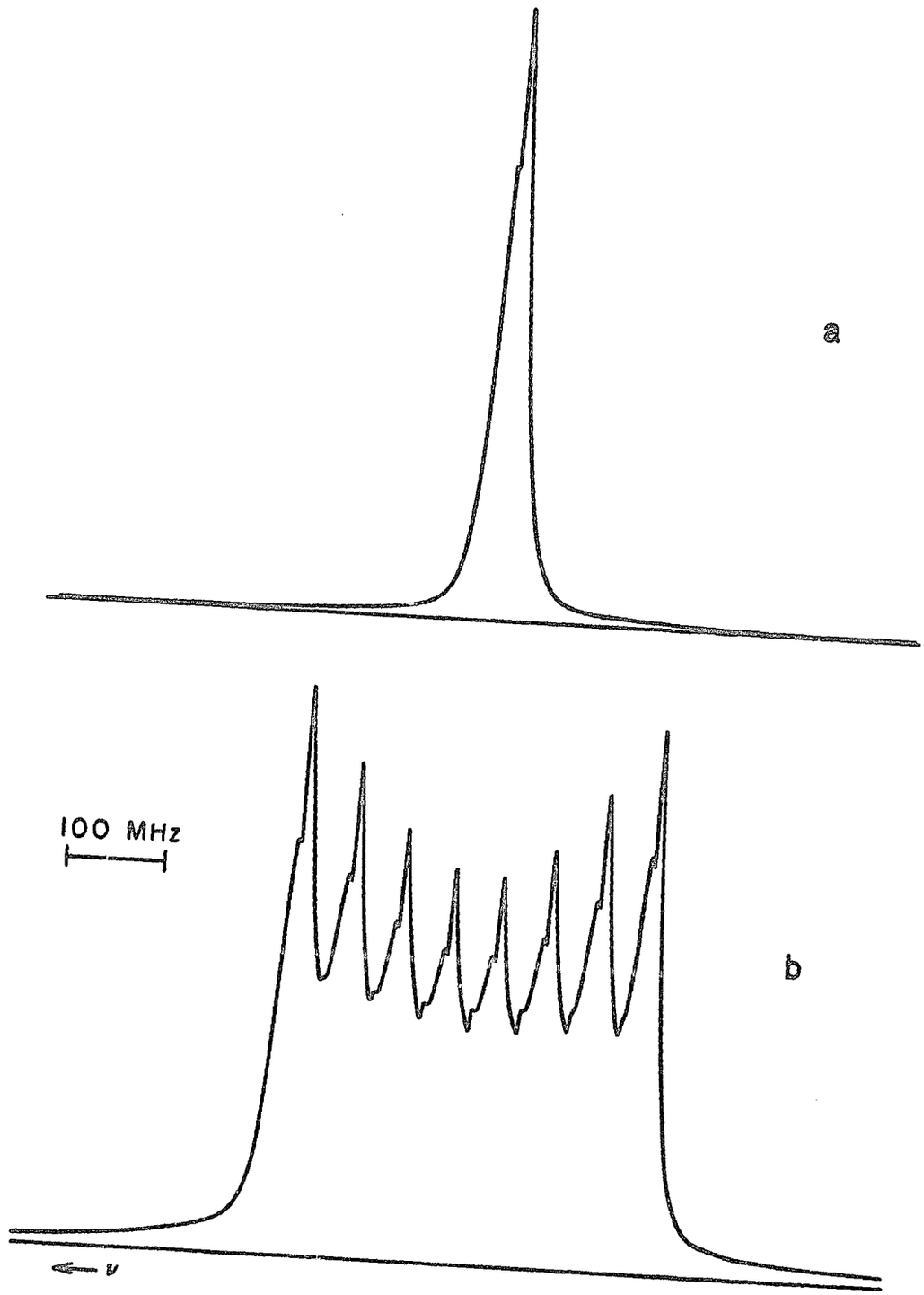

Fig.2–4. Observed spectra of (a) $\Delta F = 0$ and (b) $\Delta F = \pm 1$ transitions in a 74 gauss magnetic field.

discuss this in Section 2.6. The cause of the asymmetry of the peaks in Fig.2–4a,b is explained in Chapter Six.

2.5 Experimental Field Configuration: Definitions

The arrangement of the applied fields in the interaction region is identical to the arrangement used in our earlier measurement. As shown in Fig.2–5, the laser path, the static electric field, and the static magnetic field are all mutually orthogonal; $\hat{k}$ is aligned perpendicular to the cesium beam to minimize the Doppler shift of the transition frequency, and $\vec{B}$ is aligned along the cesium beam. The laser polarization is usually modulated between left and right circular, although some of our measurements of systematic effects are performed with linear polarization. The electric and magnetic fields are also periodically reversed in direction by reversing the voltage applied to the field plates ($\vec{E}$) or the current in the main coils ($\vec{B}$). The $\vec{E}$ and $\vec{B}$ fields commonly have contributions that do not reverse with the applied signals.

The conventional choice of axes places the y axis directly along the $\hat{k}$ direction, the x axis along the component of the flipping part of $\vec{E}$ that is perpendicular to y, and z perpendicular to x and y. In this coordinate system, the most general fields we can write down are

$$\begin{aligned}
\vec{\epsilon} &\equiv (\epsilon_z + a\Delta\epsilon_z)\hat{z} + a(\epsilon_R + a\Delta\epsilon_R)\hat{x} + ia(\epsilon_I + a\Delta\epsilon_I)\hat{x} \\
\vec{E} &\equiv (bE_x + \Delta E_x)\hat{x} + (bE_y + \Delta E_y)\hat{y} + \Delta E_z\hat{z} \qquad (2\text{–}22) \\
\vec{B} &\equiv (cB_x + \Delta B_x)\hat{x} + (cB_y + \Delta B_y)\hat{y} + (cB_z + \Delta B_z)\hat{z}
\end{aligned}$$

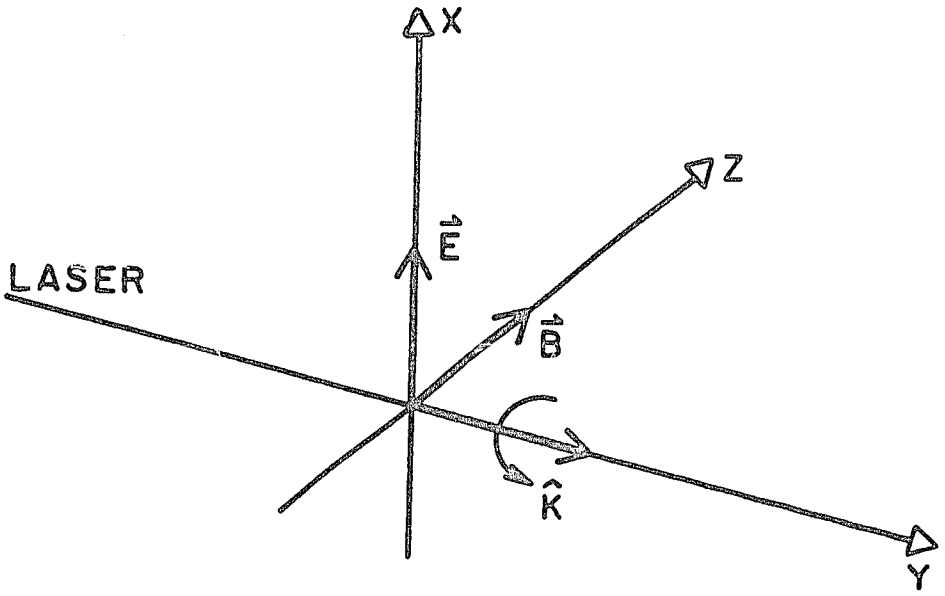

Fig.2–5. Field orientations in the PNC experiment.

where

$$\Delta\epsilon_Z \approx \Delta\epsilon_R \approx \Delta\epsilon_I \ll |\vec{\epsilon}|$$

$$\epsilon_Z \approx \epsilon_R \approx \epsilon_I \approx |\vec{\epsilon}|$$

$$\Delta E_X \approx \Delta E_y \approx \Delta E_Z \approx E_y \ll E_X$$

$$\Delta B_X \approx B_X \approx \Delta B_y \approx B_y \approx \Delta B_Z \ll B_Z$$

In this notation, non-flipping parts of the electric and magnetic fields are indicated with a Δ, and flipping fields are accompanied by a flipping variable b or c which has the value ± 1; these flipping variables, analogous to the flipping variable d introduced in Eq.2-4, are used to keep track of sign reversals that depend on reversal of the electric and magnetic fields. Similarly, the $\Delta\epsilon$ variables are small compared to the absolute size of the laser field; they account for small modulations of the field amplitude components (e.g. from birefringence effects) as the laser polarization switches between left and right circular. The major components ϵ_Z, ϵ_R, and ϵ_I are comparable to the absolute size of the laser field, although usually only ϵ_R or ϵ_I (not both) is this large at any time. Note that $\epsilon_y = 0$ by definition. The polarization reversal is labelled by the flipping variable $a = \pm 1$.

2.6 Perturbation of States by the Magnetic Field

Many of the small parity-conserving rate terms that give systematic errors result from small perturbations of the wave functions by the Zeeman interaction. In addition to misalignments of $\vec{B}$ relative to $\vec{E}$ and the laser $\hat{k}$ direction, we must consider mixing of

the different hyperfine states by the magnetic field. Normally, we consider the intermediate-field regime to begin when the Zeeman interaction is the same size as the hyperfine interaction; however, in this case we have such fine resolution of the atomic behavior that in a practical sense we are in the intermediate regime when the Zeeman shifts are less than 5% of the hyperfine separations.

First we will consider this mixing of hyperfine states by the applied magnetic field. A magnetic field along the z axis, mixes the $|Fm\rangle$ states with states from the other hyperfine level. The new states are

$$|\overline{nSFm}\rangle = |nSFm\rangle + \sum_{F"} |nSF"m\rangle \frac{\langle nSF"m|\mathcal{H}_z|nSFm\rangle}{E_{nF} - E_{nF"}} \qquad (2\text{–}23)$$

$$= |nSFm\rangle + |nSF"m\rangle \frac{\mu_B B}{f \cdot \Delta_{nS}} C^{F"m}_{Fm} \qquad (F" \neq F)$$

where Δ_{nS} is the hyperfine splitting of the nS state; here I introduce another flipping variable $f \equiv (-1)^F$ which marks the "F–flip" – switching from one initial hyperfine state to the other. Since this mixing amplitude changes sign with the reversal of $\vec{B}$, it is useful to state that dependence explicitly with the flipping variable $c = \pm 1$ introduced in Eq.2–22. Then

$$|\overline{nSFm}\rangle = |nSFm\rangle + |nSF"m\rangle cf\delta_n C^{F"m}_{Fm} \qquad (2\text{–}24)$$

where

$$\delta_n \equiv \left|\frac{\mu_B B}{\Delta_{nS}}\right|$$

We then must use this perturbed wavefunction when we calculate the matrix elements in Eqs.2-4, 2-13, and 2-15. The small $\Delta m = 0$ peaks visible between the main $\Delta m = \pm 1$ peaks in Fig.2-4b come from the small hyperfine-mixing contributions to the 6S and 7S states (the second term in Eq.2-24) in our 74 G magnetic field; this allows a small transition coupling through the α term in Eq.2-13.

Next we must consider a possible misalignment of the magnetic field. There are two obvious approaches for doing this: (1) choose axes that are convenient for calculating $\vec{E}\cdot\vec{\epsilon}$ and $\vec{E}\times\vec{\epsilon}$, or (2) choose axes that are convenient for calculating the perturbed wavefunction. In the first case, we would choose axes defined by two vectors which never move during the experiment: $\vec{E}$ and $\hat{k}$ (see Section 2.5). Then we would have to include perturbations of the wave function by small B_x and B_y fields; in exchange for this added complication, all terms proportional to ϵ_y and E_z (but not ΔE_z) are zero by definition. In the second case, we would naturally choose $\hat{z}$ along $\vec{B}$; then the wave function is simple (Eq.2-24), but there are new field misalignments ϵ_y and E_z.

Although there are advantages to each approach, I will stick to the first. It is less confusing to use axes that do not move as the magnetic field misalignments change at the reversal of $\vec{B}$; also, it is more natural and practical to realign the magnetic field by applying

shim magnetic fields than to align the laser and electric field with the prevailing magnetic field).

The B_x and B_y field components can be treated as perturbations to the wavefunction in Eq.2-24. This gives

$$|\overline{nSFm}\rangle = |nSFm\rangle + \sum_{m''\neq m} |nSFm''\rangle \frac{\mu_B \langle nSFm''|\sigma_x B_x + \sigma_y B_y|nSFm\rangle}{g_F \mu_B B(m-m'')}$$

$$+ cf\delta_n C_{Fm}^{F''m} \left\{ |nSF''m\rangle + \sum_{m''\neq m} |nSF''m''\rangle \frac{\mu_B \langle nSF''m''|\sigma_x B_x + \sigma_y B_y|nSF''m\rangle}{g_{F''} \mu_B B(m-m'')} \right\} \quad (2-25)$$

The first row of this equation is the perturbation of the $|nSFm\rangle$ portion of the wavefunction in Eq.2-24; the second row is the perturbation of the hyperfine-mixed part $|nSF''m\rangle$. Note also that the summation terms in curly brackets in Eq.2-25 are proportional to $\delta_n B_x/B = |\mu_B B_x/\Delta_{nS}|$; this term is not always unobservably small. This perturbed wavefunction is sufficient for a thorough calculation of all relevant contributions to the amplitudes in Eqs.2-4, 2-13, and 2-15. The largest terms are listed in Appendix C.

CHAPTER III

APPARATUS

The apparatus we used for this experiment is largely the same as that used in our earlier measurements of parity nonconservation, with some significant exceptions that are summarized at the end of the chapter. The laser beam excites the 6S→7S transition in a beam of cesium atoms inside a vacuum chamber, in a region of crossed electric and magnetic fields. The fluorescence given off by the atoms as they drop through the 6P to the 6S state is collected by a large-area low-noise silicon photodiode; the signal current from this detector is converted in an amplifier into a signal voltage. This signal voltage is digitized under computer control, and the results are stored for later analysis. Specifically, the fractional changes in the signal voltage are measured while the electric and magnetic fields and laser polarization are reversed under computer control. Our PNC result is then calculated from these fractional modulation measurements.

3.1 Cesium Beam Production

The cesium beam is produced in a two-stage stainless-steel oven. The cesium effuses from a glass capillary array composed of capillaries 10 μ in diameter and 0.5 mm long, in a roughly hexagonal array. The result is a wafer 0.5 mm thick with the appearance of

frosted glass. These arrays are commercially available in 25 × 25 mm pieces,[51] which we then slice carefully into three pieces, roughly 7.6 × 25 mm. This array is about 50% transparent to cesium atoms that are incident at zero angle to the capillaries, and gives a collimated beam with about 3.9° divergence (full-angle at half maximum) at low intensity. At intensities above about 10^{15} cm^{-2} s^{-1} the beam divergence begins to rise with beam intensity; our standard operating intensity is near this "knee." We keep the array hot to keep the capillaries from quickly becoming clogged.

The array is mounted on the front of the second stage of the oven, as shown in Fig.3-1. The second stage is heated by a bead heater which is made of about 40 cm of heavy nichrome wire running through the centers of hundreds of tiny insulating ceramic beads. This stage is kept much hotter than the first, in order to reduce the density of cesium molecules in the beam. The first stage is just the rear area of the oven, where the cesium is kept. The entire back end of the oven is heated using 11 large cartridge heaters supplied by a variac; we set the variac high enough to obtain the desired cesium beam intensity.

Since cesium is so volatile (it reacts readily with moisture in the air), we must open the sealed glass ampoules under vacuum, lest the cesium develop a nearly impermeable oxide crust. The ampoule-breaker assembly can break three 10 gm ampoules in sequence.

The oven is mounted on a separate flange with a low-profile high-vacuum valve on the front. When this valve is operating properly, a vacuum of better than 10^{-5} torr can be maintained in the

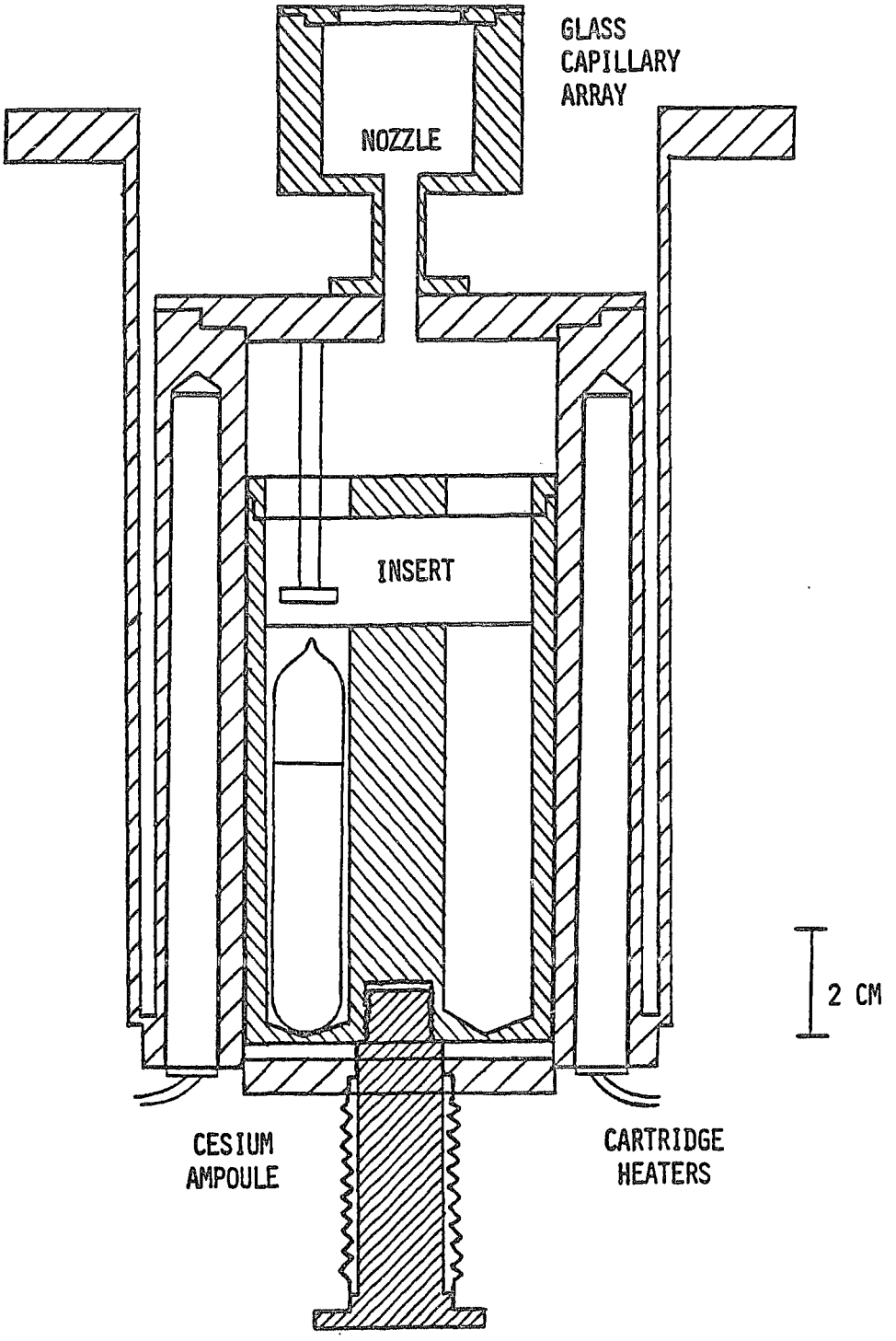

Fig.3-1. Cesium oven

oven for several days with the rest of the vacuum chamber open to air.

After leaving the oven, the cesium passes through several baffles and an additional collimating assembly to remove atoms with undesirable trajectories from the beam (Fig.3-2). Most important of these is the collimator; it is constructed of roughly 100 strips of 3-mil titanium foil, 1/4 inch wide, separated by 20-mil spacers at each end. This forms an array of narrow, parallel vertical slots through which the atoms pass. Since it has such a narrow aspect, only atoms travelling within a narrow range of angles in the horizontal plane pass through unscathed; the rest collide with the strips and emerge at random angles. In this way the atoms are further collimated in the horizontal direction in order to narrow the transition linewidth further. The final cesium beam has a full-angle divergence of about 2.6°, corresponding to a transition linewidth of 25 MHz.

We found it necessary to remount the collimator to allow better measurements of the mirror birefringence. Earlier we had simply mounted the collimator on a piece of springy steel that would bend to allow collimator tilt to adjust the tilt of the cesium beam in the horizontal direction. However, we had trouble getting a symmetric range of large tilt angles to each side of perpendicular. The collimator is now mounted on a hinge. We are able to tilt the beam to large angles to resolve the two transition peaks due to the two travelling waves in the standing-wave cavity; this allows us to measure one of the more serious systematic effects. Previously, we measured this effect only at "positive" tilt angles; this allowed

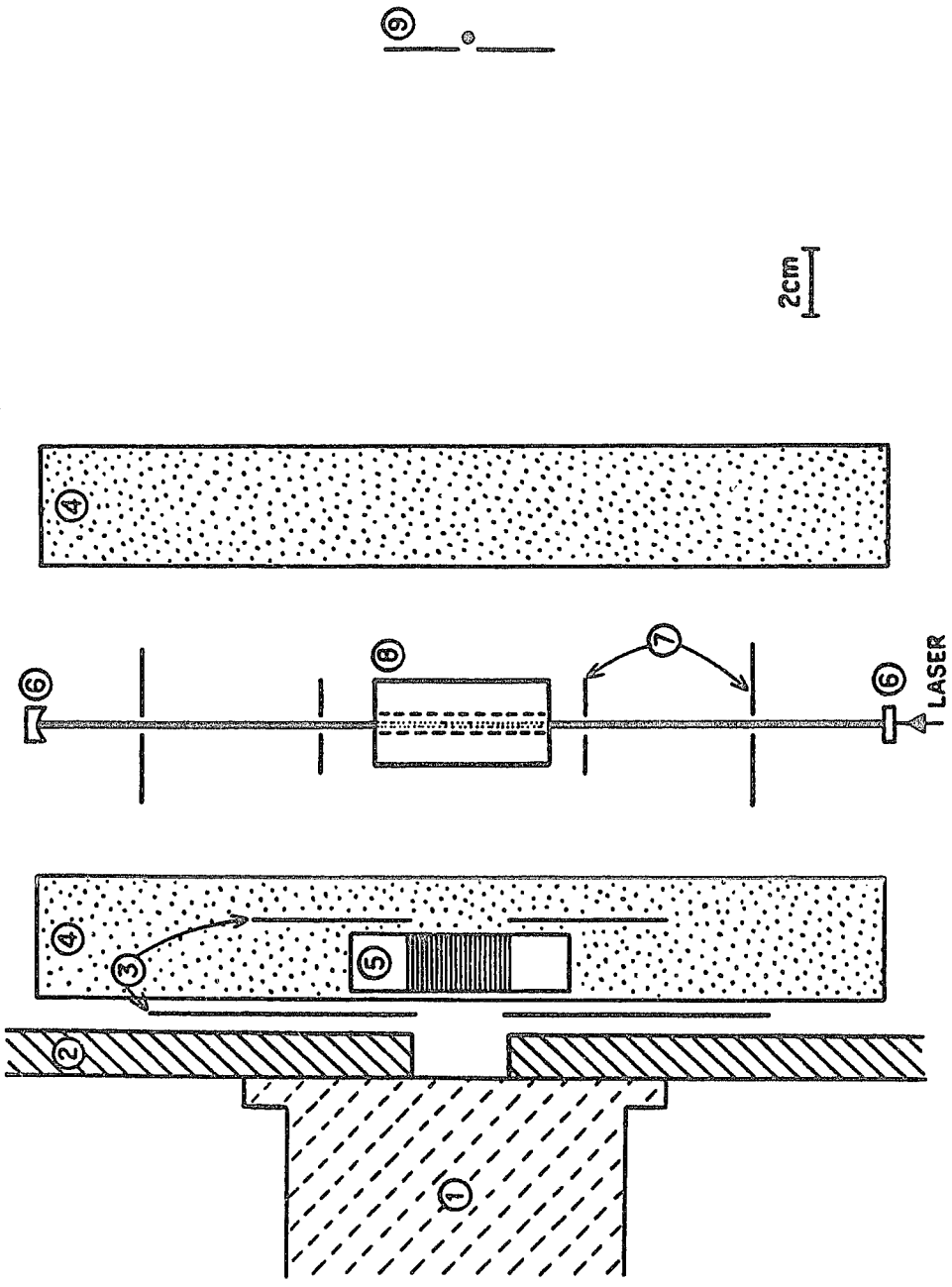

Fig.3-2. Layout of vacuum chamber: (1) Cesium oven, (2) chamber wall, (3) LN_2-cooled copper plates, (4) magnetic field coils, (5) stainless steel collimator, (6) power buildup cavity mirrors, (7) light baffles, (8) electric field plates, (9) hot-wire detector.

certain measurement errors to enter. We installed the hinge in order to have better control in placing the extremes of the range of tilt angles, so that we could measure at both positive and negative angles of collimator tilt. With this mounting we can control the collimator tilt with resolution of less than 1 mrad.

Just before and after the collimator we have two copper cold plates, cooled by liquid nitrogen (LN_2), which collimate the cesium beam and pump away the cloud of cesium that comes from scattering in the collimator. We discovered that a third cold plate mounted on the second one and suspended over the edge of the detector box gives further reduction of the cloud in the interaction region and helps to protect the electric field plates from cesium.

Since the mirrors of the power-buildup cavity are so sensitive to the buildup of cesium, we mount two small LN_2-cooled copper tubes in front of the mirrors to keep cesium away from them. We also use an automatic LN_2 level controller to keep filling the trap periodically without our attention, so that the protective copper tubes are kept cold all the time.

We have a hot-wire detector which we use for monitoring the intensity of the cesium beam. The tungsten filament (5 mils in diameter) is heated by a steady DC current of 1.4 A, and the collector voltage is -90 V. The filament glows with a light orange-yellow color. We measure the current through the collector with an electrometer; we take this current to be proportional to the cesium flux.

This detection system is somewhat sensitive to the filament current; we performed some tests to choose a value that would give

the most reproducible results. We measured the collector current at several values of filament current and found a plateau region near 1.4 A. We conclude that the higher slope below this current is due to increases in the ionization efficiency and the higher slope at higher currents is due to electron photoemission at the surface of the collector. We use 1.4 A as our operating current. The reproducibility of successive measurements of the cesium beam using the hot-wire detector is at the 5% level.

3.2 Interaction Region

The cesium beam, after passing through the collimator and cold plates, then intersects the laser beam in a region of perpendicular static electric and magnetic fields. In a short time after the excitation of an atom by the laser, it decays through the $6P_{1/2}$ and $6P_{3/2}$ states to the ground state, emitting photons at about 1.4 μ and 850-890 nm. The silicon photodiode detector nearby is about 80% efficient at the shorter wavelength,[52] but completely insensitive to the 1.4 μ light. In a fairly small region we must apply a uniform electric field, collect and filter the light for detection, and also provide a path for the cesium to enter and exit.

The arrangement we use is shown in Fig.3-3. The quartz field plates lie above and below the interaction region; they are transparent to allow the infrared light to pass through to the collection optics above and the detector below. Both field plates are coated with a transparent conductive coating for applying a vertical electric field. The top plate is mounted on a cylindrical

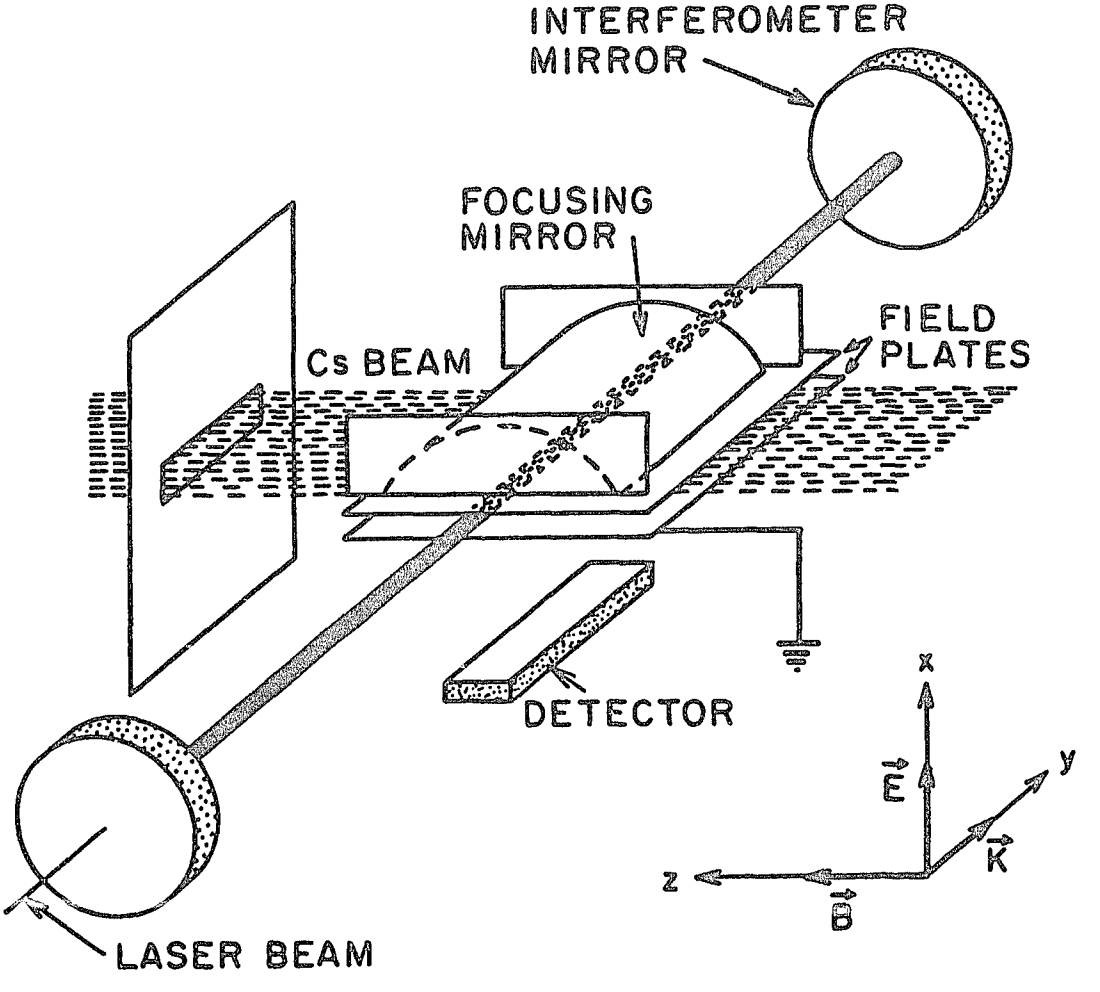

Fig.3–3. Detailed view of the interaction region. The cesium beam crosses the laser beam from the left in a region of static electric field.

mirror (the "collector") that focusses light from the interaction region onto the detector below. The long narrow detector is mounted below the lower field plate inside an aluminum box. Between the lower field plate and the detector are two filters, one of which has an additional transparent conductive coating. The first filter (Corning BG-3) provides some attenuation of scattered green laser light with little attenuation of the infrared light; the other (Corning RG-780 plastic) provides much stronger attenuation of green light with about the same infrared transmission (about 85%). The BG-3 filter is necessary because the RG-780 filter shows much greater infrared fluorescence of green light; the RG-780 is needed because the BG-3 does not attenuate enough in the green. Together they reduce the amount of scattered light at PNC measurement conditions to less than 10% of the atomic signal. The transparent conductive coating on the bottom of the BG-3 filter is grounded to shield the detector from transients due to the electric field reversal.

The detector is a large-area low-noise silicon photodiode, 5 × 56 mm, specially made by Hughes Aircraft Company. It is LN_2-cooled to reduce the noise current. It is operated in the photovoltaic mode (zero bias), with the current sent to a very low noise amplifier. The detector is mounted on an aluminum chunk supported by nylon screws (about 1 inch long); this assembly is inside a rigid aluminum box, with a removable top on which the field plates and the collector are later mounted. The box serves the important function of shielding the detector and its electronics from transients at the electric and magnetic field flips.

The collector is a cylindrical reflector used to reflect and focus the atomic fluorescence light onto the detector. It sits immediately above the interaction region, with its gold-coated concave side facing down. It is made from a section of glass tubing cut parallel to the axis; the concave side has been coated with a thin layer of gold laid on a "primer" layer of nichrome. This gold coating has a high reflectivity at our infrared wavelengths. Standard aluminum front-surface coatings, by comparison, have a reflectivity around 50% at 850 nm.

The field plates are pieces of quartz slide glass, 25 × 50 × 0.5 mm, that have been coated with an antimony tin oxide (ATO) coating. This coating has more than 80% transmission and less than 30 Ω/square conductivity; it is durable enough to survive more than 2 months of light exposure to cesium and moisture; and it gives acceptably small stray electric fields in the interaction region.

To keep cesium from building up quickly on the field plates, we keep them slightly warm by heating them with a 17 kHz AC current. We use a high-frequency heating current so that stray fields from the applied voltage would be averaged out quickly. We have found that heating does help to reduce cesium buildup, but that applying too much heat can cause faster deterioration of the conductive coating. The heat may be catalyzing a reaction between cesium and the coating material. The lower field plate withstands a great deal more power than the upper field plate. This is probably because the lower field plate is firmly mounted on the detector box; the box is well connected to the PBC base, and is also slightly cooled by radiation to the LN_2-cooled detector inside.

The change to ATO-coated quartz field plates and to a 5 mm plate spacing also dramatically improved the transition signal-to-noise ratio by reducing the noise from the scattered green light. Much of the scattered light signal was actually due to fluorescence of the plastic substrate of the original conductive coating material. By switching to glass, we eliminated this fluorescence and dramatically reduced both the scattered light and its noise. At the same time we changed from a plate spacing of 4 mm to 5 mm. This also reduces the amount of green light that reaches the field plates.

The upper field plate is bonded to the underside of the collector using a small amount of 5-minute epoxy at the edges. The lower field plate is bonded to the BG—3 filter using an index-matched optical cement to minimize reflection at the interface. The filter and lower field plate are tacked onto the surface of the aluminum lid of the detector box using a light cement, and then the edges are sealed to the lid with RTV (a silicone rubber sealant) to keep cesium from leaking in around the edges. To set the spacing of the plates, we set a 0.5 cm spacer and the collector onto the lower field plate and fix the collector in position with tape; we then use 5-minute epoxy to bond 4 glass legs to the sides of the collector assembly. After the epoxy has set, the collector is ready to be used. If the collector "rocks" diagonally after the spacer is removed, then the legs are clearly positioned incorrectly and must be redone. We believe that the spacing can be set accurately in this manner to within ±0.05 mm, or 1% of the nominal spacing.

Another of the improvements for the present measurement is the construction of a tilting mount for the detector box, to allow the

field plates to be rotated around the z-axis (the nominal direction of the magnetic field). The box now rests on the ends of three screws. Two of the screws are on the end closest to the input mirror of the power-buildup cavity, arranged along the z direction. The third is a fine-threaded screw on the other end, to which we have attached a small DC motor and a gearbox. If we wish to alter the angle E_y/E_x between the laser and the electric field, we can drive the motor in either direction to raise or lower the one end of the detector box. With roughly 1-second precision in the timing we can get 10^{-5} radian precision in the orientation of the electric field. This is much smaller than the typical measurement inconsistencies from day to day.

The magnetic fields in the interaction region are controlled by four separate sets of field coils. The main field is supplied by a large Helmholtz pair inside the chamber. These coils are made of enameled wire of 0.10 inch square cross section wound around an aluminum spool. The inside diameter of the spool is 24 cm, the width of the channel is 2.9 cm, and the outside diameter of the windings is 29 cm. Each coil has approximately 100 turns. The field measured in the center of the pair is 74 gauss at a current of 10 A.

There are additional coils mounted on the outside of the chamber to trim the various components of the magnetic field to zero. The y fields are controlled by a pair of 27 cm diameter coils on the ends of the chamber, centered on the laser windows. The x fields are controlled by a pair of 12 × 29 cm rectangular coils mounted on the top and bottom of the chamber. The z fields are controlled by a coil of wire wrapped around four screws on the side of the chamber, around

the oven flange. These shim coils, although crude, give sufficiently uniform fields that we can control the systematics throughout the interaction region. In addition to nulling the ambient field of the earth and the building, we also use relays to change the shim currents to null fields resulting from misalignment of the main B_z coils; an important part of taking the systematic measurements was adjusting the values of these static and B_z-flipping parts of the shim currents.

3.3 Detector and Amplifier

The detector is a low-noise silicon photodiode measuring 5 × 56 mm. Its shunt resistance at room temperature is around 1 MΩ; the shunt resistance increases by about a factor of ten for every 20°C drop in temperature. When the detector is cooled by our LN_2 cold trap system, it reaches a shunt resistance of 10^9 Ω with a shunt capacitance of 2 nF.

The detector is used in a photovoltaic mode; that is, we make use of the fact that the detector pushes current through its terminals in proportion to the amount of light collected. This current is carried to an amplifier outside the vacuum chamber which puts out a voltage proportional to that current. The amplifier is an ordinary current-to-voltage converter design (see Fig.3-4) using an AD52J low-noise operational amplifier manufactured by Analog Devices Corporation. The size of the feedback resistor determines the output voltage ($V_{out} = -I_{in}R_f$).

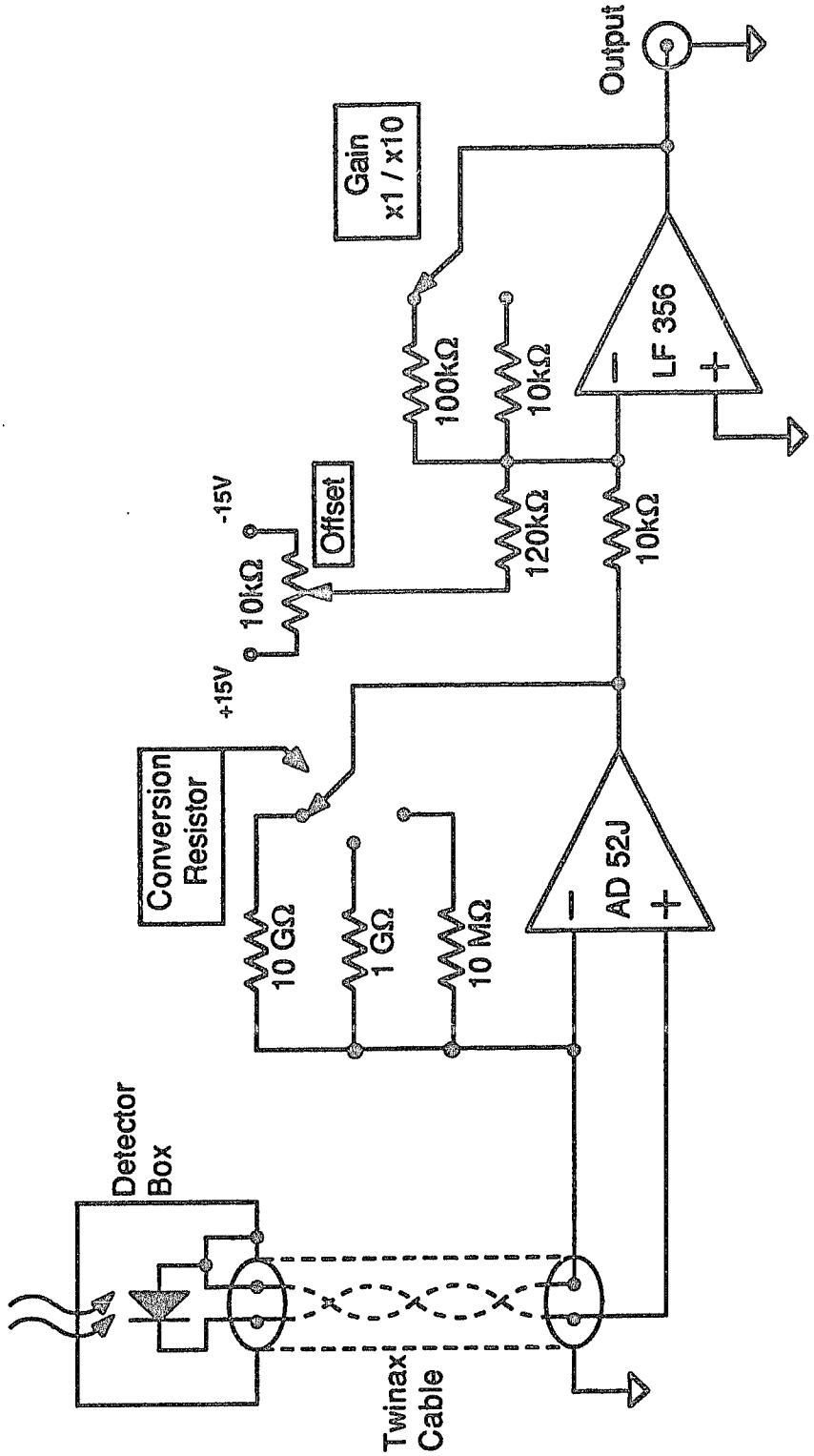

Fig.3-4. Low-noise detector amplifier

This current-to-voltage amplifier is followed immediately by an inverting amplifier with switchable gain of −1 or −10. This allows us to get the signal voltage in a good range despite the use of a limited selection of R_f values (10^7 Ω, 10^9 Ω, and 10^{10} Ω). This amplifier also has an offset control, which allows us to subtract a DC offset before sending the signal to the voltmeter that measures the average size of this signal. This offset enables us to subtract the offset due to background sources (such as scattered green laser light) so that the signal measured by the voltmeter is just the atomic fluorescence signal and not the sum of the fluorescence and background sources. This offset is repeatedly checked.

The signal then is sent to the voltmeter and to another voltage amplifier with a stable offset, with which we subtract the average signal voltage. The result (near zero volts) is sent to a gated integrator which integrates the signal for a 200 msec interval under computer control. The integrated voltage is digitized and stored in the computer. In this way we can measure small changes in the transition signal and then scale them to the full signal size.

This measuring system is a useful tool for studying the noise characteristics of the system. With it we can measure noise levels on the detector amplifier output of less than 230 $nV/\sqrt{Hz}$. We find that the noise level on the detector signal is around 50 $\mu V/\sqrt{Hz}$, limited by current spikes that we attribute to cosmic rays and radioactivity. The spikes were much more frequent when we were using a glass RG-780 filter instead of the plastic filter; we found that placing a 1 mm glass slide under the glass RG-780 filter dramatically reduced the spike size and rate. We concluded that the filter was

slightly radioactive and that the emitted particles were generating current pulses. The similar character of the remaining spikes suggests that perhaps these are also due to particle bombardment.

We have also been able to measure the detector noise level between these current spikes, when the noise was much quieter. Our measurements show that in the absence of the current spikes, the noise is about 25 $\mu V/\sqrt{Hz}$; this is limited by the detector amplifier noise characteristics. The detector/amplifier noise characteristics will be discussed in more detail in Section 4.7.

3.4 Power Buildup Cavity

The power buildup cavity (PBC) is a resonant Fabry-Perot interferometer composed of two highly reflective mirrors facing each other. When we couple the dye laser beam into the lowest-order transverse mode of the PBC, we can achieve a total peak power on resonance of almost 1 kW continuous-wave; in the process of locking the laser frequency to the cavity resonance we must narrow the linewidth of the laser to less than 30 kHz. So there are clear advantages to using a resonant cavity to supply the laser field that excites the transition: extremely high laser fields for boosting the signal size and a narrow laser linewidth with small high-speed frequency fluctuations. Since our transition is extraordinarily weak, we do not have to worry about atomic absorption affecting our resonant power. Thus, in a sense, all we're doing is reusing our laser photons thousands of times before discarding them.

The optical layout is shown in Fig.3-5. The light from the dye laser is sent through a telescope to set the spot size and wavefront curvature; it then passes through a Pockels cell used in the intensity stabilization system; then it passes through a Faraday isolator, which prevents light from returning from the PBC to the dye laser; and finally through the polarization-controlling Pockels cell before entering the cavity.

The mirrors have a very high-quality dielectric coating on the front surfaces. The mirrors we use are significantly higher quality than those used in our earlier measurements in cesium: the power buildup factor is about 1300 rather than 180, and the output-mirror coating birefringence is now essentially zero. The problems we had to overcome before being able to use them arose from the tremendous narrowing of the cavity resonance width and the resulting need for substantially better stabilization of the laser frequency. The mirrors have been selected from among several manufacturers on the criteria of scattering and absorption losses, transmission, and the reflection-birefringence of the coating. The cavity should have a high power buildup factor, a broad enough cavity linewidth, and low enough birefringence effects from the two mirrors. Clearly we want the highest buildup factor we can get; but if the cavity resonance is too narrow, we will not be able to lock the frequency at the peak, and the residual frequency fluctuations will lower the average buildup from the peak value.

We have chosen an input mirror made by Particle Measuring Systems; it is the same type as the mirrors they produce for green-output helium-neon lasers. The transmission of the mirror is

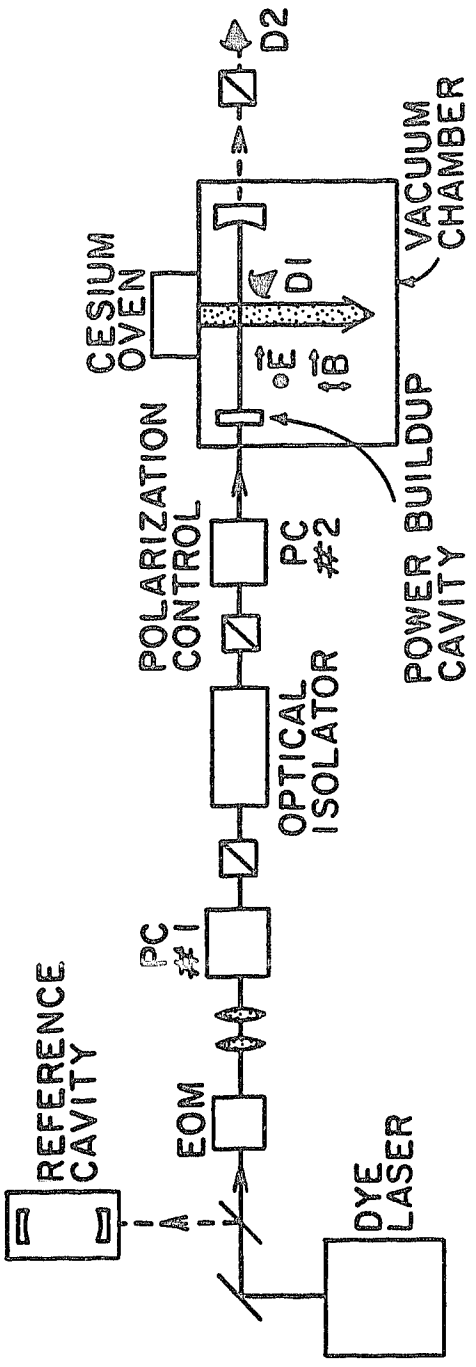

Fig.3-5. Layout of laser optics

3.5×10^{-3}, and the scattering and absorption losses together are about 1.8×10^{-4}. The birefringence of the mirror coating is measured by placing a linear polarizer after the PBC and measuring the modulation of the transmitted light. As the mirror is rotated, the fractional modulation will follow sinusoidally as the coating birefringence axes alternately line up with the axis of the linear polarizer (see Appendix B). The input mirror birefringence gives a ±4% modulation of the intensity after the analyzing polarizer as the input mirror is rotated. This implies a coating birefringence on the order of 5×10^{-6} radians at each bounce (using the finesse given below and the results of Section B.3).

The output mirror is a laser-gyroscope mirror supplied by Litton. These mirrors are manufactured to have extraordinarily low birefringence and very low scattering and absorption losses. The total scattering and absorption losses are somewhat less than the PMS mirror and the transmission is about 3.2×10^{-4}. The coating birefringence of the output mirror is far more important than that of the input mirror; it is the source of an E1·M1 interference term that is one of our major systematic contributions (see Chapter 4). At the beginning of this set of measurements, the birefringence of this mirror coating was zero within our measurement uncertainty. As the mirror aged under conditions of heavy and highly localized laser heating coupled with occasional cesium deposition, it began to develop a measurable birefringence on the order of 2×10^{-5} radians.

The PBC with these mirrors has a finesse of 6000 and a free spectral range (FSR) of 600 MHz, implying a cavity linewidth of about 100 kHz. However, the free-running laser linewidth is close to

2 MHz; therefore, we clearly need some elaborate servo systems to reduce it to less than 30% of the cavity linewidth (for a goal of less than 10% intensity modulation in the cavity from the residual frequency jitter). This stabilization system will be discussed in detail later.

The mirror curvatures are 50 cm spherical for the input mirror and flat for the output mirror. The spacing is nominally 25 cm, giving us a semi-confocal configuration. We have tried several different choices of mirror curvatures and spacing in the course of this experiment. The arrangement we have found works best is the near-semiconfocal configuration. The two chief advantages of this arrangement are the small spot sizes and the lower sensitivity to slight mirror misalignments. The small spot size allows us to use smaller apertures in the baffles with which we keep the scattered laser light from reaching the detector. This scattered light originates at the PBC mirror surfaces and causes background signals on our detector, often with a high noise level. The other advantage is that small misalignments of the mirrors while the chamber is under vacuum can be corrected more easily by realigning the laser from outside. The spot size advantage is relatively slight: in fact, the spot sizes do not increase rapidly with increasing radius of curvature. The more significant difference between a 50 cm mirror and a 100 cm mirror is the ease of realignment when the mirrors shift their alignment under vacuum. The causes of this misalignment are discussed later. The laser displacement required to realign the cavity from the outside after a tilt of the 100 cm mirror is twice as large as for the same tilt of a 50 cm mirror. This difference often

determines whether the new laser path intersects one of the baffles (reducing the maximum buildup).

The mirrors are mounted on fine-adjusting tilt mounts to allow careful alignment of the mirrors. This allows us to place the laser path where we want it and then tilt the mirrors until the cavity is fully aligned. Just outside the laser there is also a telescope made from two lenses with short focal lengths; this enables us to vary the spot size and wavefront curvature of the laser to couple it efficiently into the lowest order transverse mode of the PBC. With careful mode-matching, we can couple more than 95% of the laser power into this mode.

The PBC mirror mounts are fastened to a base of ordinary granite. This granite block measures roughly 30 × 10 × 5 cm tall; it also supports the scattered-light baffles and the detector assembly. The block is supported by pads of neoprene rubber at each end and is fixed to the floor of the chamber using aluminum clamps and more neoprene pads. This mounting isolates the PBC from vibration fairly well, but also gives good reproducible positioning. Granite was selected for the PBC base because it has thermal expansion properties similar to quartz but is acoustically more "dead."

One of the problems we have studied is a temporary decrease in the peak buildup in the lowest-order mode of the cavity at high laser power, accompanied by changes in the transmitted spot shape from the PBC and a significant increase in the scattered-light noise on the detector signal. When the mirror absorption is large, the peak PBC power decreases for several milliseconds after the laser frequency was locked to the PBC resonance, and is restored after several

milliseconds off resonance. Thus, for example, we would see a significantly higher value for the peak transmitted intensity of the PBC when the PBC scans quickly across the resonance than when it is steadily locked on resonance.

The apparent cause is the coupling of light into higher-order transverse modes of the cavity due to distortion of the mirrors. We have seen evidence that the when the PBC mirrors are dirty, they can absorb enough power at high laser intensity to cause thermal expansion of the substrate glass and distortion of the surface. This is observable in changes of the PBC transmitted spot shape and in tuning effects during slow scanning of the laser frequency across the PBC resonance. The spot shape changes by adding a ring around the central gaussian spot at the same time that the PBC transmission is reduced as described above. The tuning effects are observed as hysteresis in the position of the PBC resonance as the laser is scanned slowly back and forth across the resonance. The distortion of the mirror surface causes the mirror surface to extend closer to the other mirror, decreasing the spacing of the mirrors. Thus as the laser frequency moves onto the resonance and the cavity power increases, the PBC resonance frequency is either pushed away or pulled through (depending on the scan direction).

The earlier observations of an increase in the scattered-light noise apparently resulted from the same distortion effects. The degree to which light is coupled into these higher-order modes would fluctuate rapidly as the frequency-locking circuits struggled to keep the laser locked on a rapidly moving resonance. The larger spot sizes of the higher-order modes result in greater scattering off the

baffles, which then results in greater scattered-light signals in the detector.

We treated this problem by moving the mirrors toward each other so that the other modes had their resonance frequencies to the "red" side of the resonance of the lowest-order mode (at semiconfocal spacing, the higher modes are at the same frequency as the lowest-order mode). Then as laser heating caused distortion of the surface of the mirror, the modes that the laser light would have been coupled into were tuned further from the laser frequency; thus coupling was suppressed.

Mounted in the tilting sections of the mirror mounts are the heaters and thermistors of a temperature control system. The problems we faced were the slow deposition of cesium on the mirror surfaces (causing a decrease in the power buildup factor) and large drifts and step-changes in the mirror birefringences that correlated well with temperature changes. The simplest explanation of the birefringence effect is that the temperature changes introduced stresses into the mirror mounts and the mirrors themselves, causing stress birefringences in the substrates to change. The use of the temperature controller vastly reduced this problem. The other benefit of heating the mirrors was that cesium tended to collect on the mirrors less when they were hot.

This system actually only controls the temperature of the output-mirror mount, since the birefringence of this mirror is the most sensitive to temperature. However, the same heater voltage is sent to the heater on the input mirror mount, allowing us to regulate its temperature very coarsely.

The heaters ended up causing another problem: misalignment of the mirrors during evacuation of the chamber. The change in the distribution of heat load on the mirror mounts caused by the elimination of convection losses apparently caused the mounts to buckle slightly, tilting the mirrors away from their original alignment.

The input mirror is mounted on a piezoelectric tube to allow a few GHz tuning of the cavity resonance. The tube has a 3/8 inch outside diameter with a wall thickness of 1/16 inch; the electrodes are metallic coatings on the inside and outside surfaces of the tube. When a voltage of 0→1 kV is applied to these electrodes, the tube changes in length by about 4 longitudinal orders of the cavity, allowing a cavity tuning range of the same number of free spectral ranges (i.e. 2.4 GHz). This tuning capability is necessary to allow the PBC resonance to be placed at the atomic resonance frequency, and to compensate for thermal expansion of the PBC frame once the frequency has been locked.

The use of this piezo driver to move the mirror also brought on a secondary problem: changes in the stress birefringence of the input mirror. If we bond the mirror to the end of the piezo tube using a rigid glue like a cyanoacrylate adhesive (e.g. Krazy Glue), the mirror acquires uneven stresses as the piezo tube expands and contracts in diameter and length. Thus at one time the tuning of the PBC caused changes in birefringence-sensitive measurements such as the measurement of the output-mirror coating birefringence. To control this possible source of systematic contribution, we remounted the mirror using more and more flexible adhesives; we finally chose

RTV (the silicone-rubber sealant mentioned earlier) because of its flexibility and despite the fact that our mechanical resonance frequency was lowered to less than 3 kHz. We found that since the PBC vibrations we needed to control were all at fairly low amplitude and frequency, the loss of bandwidth in that part of the frequency stabilization system was not serious. However, the stress-birefringence problem was greatly reduced.

The Faraday isolator is a device that allows the laser beam to pass in one direction with virtually no attenuation but prevents the light from passing through in the other direction. It uses the Faraday effect in certain special glasses to perform an optical rotation of the light that depends on an applied magnetic field but not on the direction the light is travelling. The light passes through a linear polarizer, is rotated by 45° in the Faraday glass, and passes through another polarizer. When returning along the same path, it is rotated another 45° in the same direction, causing extinction at the first polarizer. In this way, light of arbitrary polarization can be prevented from travelling backwards through the isolator. Fortunately this device also leaves the emerging beam with clean linear polarization, which we need for producing the circular polarization for the experiment.

3.5 Laser System

The laser is a commercial ring dye laser manufactured by Spectra Physics. It is pumped by an argon ion laser made by Coherent, Inc. The wavelength we need is 540 nm, for which we use Rhodamine 560 HCl

laser dye in an ethylene glycol solution. We have made several small modifications to the dye laser and we have built our own frequency-stabilizing electronics to give us the degree of stabilization we need.

The basic design of the laser is shown in Fig.3-6. The pump laser is focussed by a 5 cm curvature mirror onto a thin flat jet of laser dye solution. The four mirrors M_1–M_4 form a ring resonator whose lowest-order resonating mode passes directly through the illuminated spot on the dye jet. The output coupler M_4 is about 10% transmitting.

The lasing mode is selected using a triple-plate birefringent filter, a thin glass etalon, and a scanning etalon. A unidirectional device similar to our Faraday isolator confines lasing to one direction in the loop. The birefringent filter is composed of three similar filters, with three different effective FSR values. The thin etalon ("fine etalon") is an uncoated piece of fused silica of thickness 0.11 mm, mounted perpendicular to the laser beam; it acts as an interferometer with a FSR of 900 GHz (about 8.7 Å at our wavelength of 5400 Å) and a finesse of about 0.6. As the etalon is tilted manually, the peak-transmission frequency is shifted.

The scanning etalon ("581B etalon") is composed of two planar mirrors separated by a piezoelectric crystal. These two mirrors have a dielectric coating with a reflectivity of 30% (cavity finesse $\approx$ 2.5). The FSR of the cavity is 75 GHz. The cavity is tuned by applying a voltage of 0 $\rightarrow$ 1 kV to the piezo element, which changes the spacing of the mirrors. This tuning capability is important to

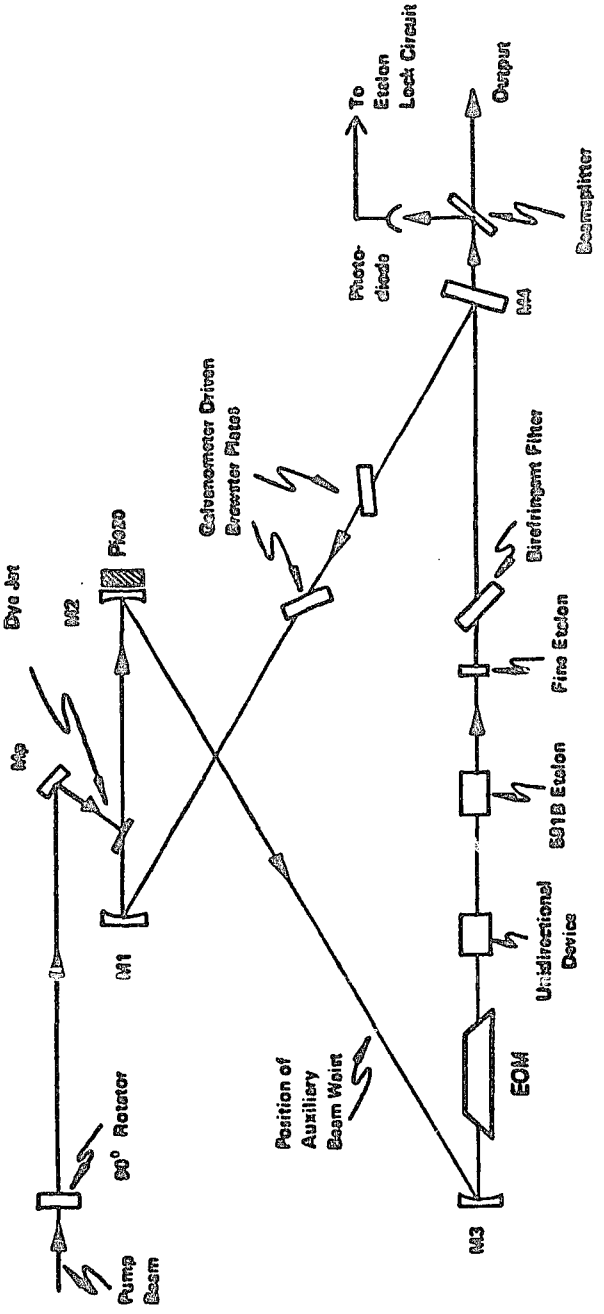

Fig. 3-6. Layout of Spectra-Physics ring dye laser

allow us to select, lock onto, and track any longitudinal mode of the laser cavity as we perform a long frequency scan.

The frequency of the selected mode can be changed using three different devices: the galvanometer-driven windows, the piezo-driven mirror, and the electro-optic modulator (EOM). The piezo-driven mirror was significantly upgraded, the EOM was added, and sophisticated electronic servo systems were developed for each to enable the improvements we made in the laser frequency stabilization system.

The galvo-driven windows are two thick windows mounted on galvanometer drivers and set at Brewster's angle. Tilting the windows causes changes in the optical path length through the window; the use of two counter-rotating windows minimizes the deflection of the beam as the window tilt is changed. The scan range of this system is large ($\approx$ 150 λ), but the mechanical resonance of the galvo driver is only about 500 Hz.

Next is the mirror mounted on a piezo disk to allow translation of the mirror along the path of the laser; this allows a high-speed change in the optical path length. The mechanical resonance frequency of this system is about 200 kHz, and the range is about 1 λ. A mechanical resonance frequency this high is extraordinary; the usual is between 5 and 20 kHz. To get this high speed, we used a mirror on a very light substrate, a thin piezo disk (rather than a piezo tube) for extra mechanical strength, and a specially made conical stainless steel mounting fixture. Both the composition and shape of this mounting fixture proved important.

Last is the intracavity EOM, which gives us the ability to correct the laser frequency at speeds up to 1 MHz. The bandwidth of the device is much higher than this (several GHz if necessary); the range is about ±0.02 λ (about ±4 MHz) at signal voltages of ±30 V. The chief speed limitation in this system is in the electronics.

3.6 Frequency Locking System

The stabilization of the laser frequency is a difficult but crucial part of this experiment. As noted before, we need to stabilize the laser frequency at the resonance peak of the PBC to maximize the power in the interaction region. We also need to stabilize the frequency at the peak of the cesium resonance to a degree sufficient to keep the transition rate noise as low as possible.

We must first generate an error signal that immediately tells the laser which way to change its frequency to stay at the resonance peak. The most difficult stage in which to do this is the dye laser-to-PBC lock, since the error signal must respond to frequency discrepancies at very high speed. The first limitation in a locking system is the modulation frequency chosen: the error signal derived cannot be substantially faster than this. For this reason we eventually chose RF modulation frequencies. The method finally chosen is the method of Drever *et al.*, which is a descendant of the method of Pound.[53] In this system, we apply 2 MHz phase-modulation sidebands to the laser before sending it to the buildup cavity. We then extract the beam that bounces off the cavity, and send it to a

high-speed photodiode. We then send this signal to an RF mixer, which extracts the in-phase 2 MHz signal. The amplitude modulation at 2 MHz of this rebounding beam is proportional to the detuning between the laser and the cavity resonance, and the phase indicates the sign of the detuning. Thus the mixer output is exactly the error signal we need for locking the laser to the PBC. After suitable filtering (details later), this signal is sent to the galvos, the piezo-mounted-mirror, and the EOM.

The circuit for deriving the error signal is shown in Fig.3-7. A signal generator produces a 2 MHz signal to drive the tuned circuit on the input of the phase modulator, which is a KD*P Pockels cell; it also drives the reference input of the mixer. The tuned circuit is a series-resonant LC circuit that allows us to get much higher voltage across the phase modulator, for much greater phase modulation. The reference signal goes to the mixer through a 20 m section of 50 Ω cable that provides the necessary phase shift. The fast photodiode produces a high-frequency signal containing all of the 2 MHz amplitude-modulation signals on the reflected beam. This signal is buffered and sent to the mixer, where the amplitude of the 2 MHz component is extracted. This error signal is then split and sent to the three different systems for stabilizing the laser frequency. After filtering, the signals go to the device drivers and then to the devices themselves.

Each circuit performs its own filtering to match the capabilities of the system. In the EOM circuit, we selected an AC-coupling frequency of 16 kHz and a low-pass filter (LPF) frequency of 16 kHz. In the piezo system, the AC coupling frequency was 1.6 kHz

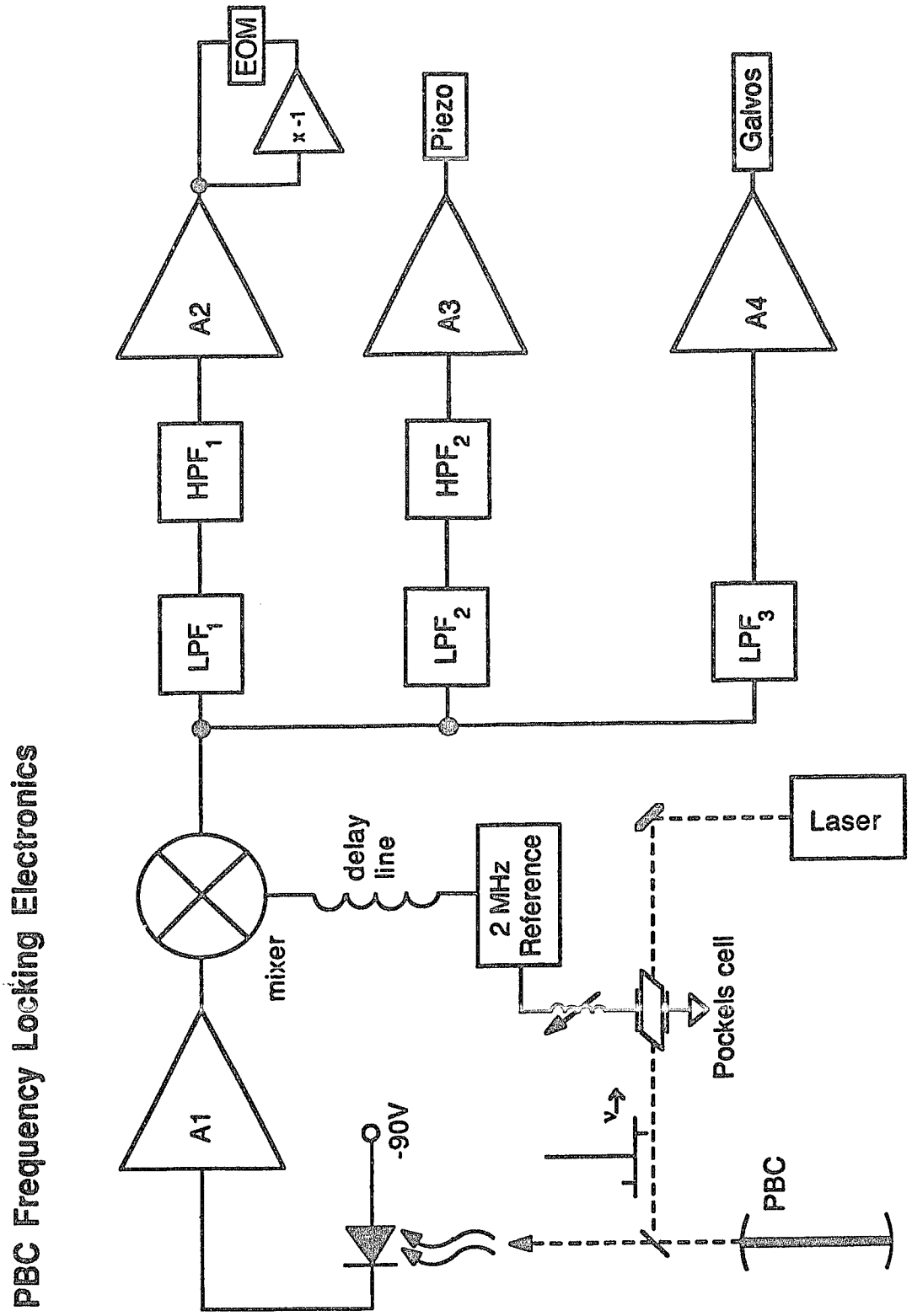
PBC Frequency Locking Electronics
EOM
x -1
Piezo
Galvos
A2
A3
A4
HPF1
HPF2
LPF1
LPF2
LPF3
delay line
2 MHz Reference
mixer
A1
-90V
Laser
Pockels cell
PBC

Fig. 3-7.

and the LPF frequency was 5 Hz. The galvo driver was basically used only to correct for the large drifts: its LPF frequency was 3 Hz, and its DC gain was very high.

In each case we used a combination of high gain and low LPF frequency. This allows the maximum gain at all frequencies subject to the constraint that oscillation may not occur. At some frequency in each system, the combination of resonance phase shifts and signal delay times will combine to give a net 180° phase shift of the feedback signal. Since the loop applies negative feedback at lower frequencies, the feedback is then positive at this high frequency; if the open-loop gain of the feedback loop is greater than one at this frequency, oscillation will occur. Thus we add a single pole (an LPF) to the transfer function of the feedback electronics to reduce the gain at higher frequencies, allowing high gain at frequencies far below the resonance point. The lower the LPF frequency is, the better: if the LPF frequency is lowered by a factor of ten and the gain is increased by the same factor, the gain at high frequency is the same -- but the gain below the new LPF frequency has increased by a factor of ten. The exception to this rule of thumb is the case of AC-coupled stages, in which the low-frequency gain is intentionally limited.

The problem with adding a second filter is that each pole adds a 90° phase shift to the signal; two such filters would cause oscillation very close to the higher of the two filter frequencies. Since the filter frequencies normally would be placed far below the normal oscillation frequency of the system, we would be worse off than with only one filter.

The EOM and piezo circuits also have high-pass filters (AC coupling). We must limit the low-frequency gain in these circuits to prevent these small-range, high-speed devices from trying to correct for large, slow drifts, which are the province of the galvo system. Similarly, we must try to keep the EOM from trying to handle the work of the piezo. We have set their gains and the EOM AC-coupling frequency so that the EOM covers most of its voltage range in normal use, but rarely needs to step beyond that range to cover a larger frequency jump; those larger jumps are left to the piezo system. In essence, we have tailored the filters to cause the three systems share the load equitably.

The piezo circuit has two sections: one does the AC-coupling at a lower frequency than the other. Each has its own gain control. The use of two such sections was originally expected to prove useful; in practice, I have found it difficult to discern a difference in their effects on the locking.

The piezo is driven by a 400 V high speed amplifier. Though its rolloff frequency (100 kHz) is less than the piezo's 200 kHz mechanical resonance frequency, it does not seriously limit the performance of the system.

The EOM is driven directly by the final stage of the filter/driver circuit and by an inverting amplifier fed by the same signal. Since the voltage on one terminal is equal to and opposite in sign from that on the other terminal, the voltage across the EOM crystal is twice the voltage at either amplifier. In this way, we can double the frequency range of the EOM without resorting to expensive or complicated amplifier techniques, and without any

decrease in the bandwidth of the electronics. This factor of two is both necessary and sufficient for our system: the final voltage range used is 20 V peak-to-peak with frequent spikes to ±20 V.

The next step would be to lock this highly stabilized laser frequency at the peak of the transition signal. However, since the PBC mirror mounts are fairly poorly stabilized, the laser frequency is actually seen to wobble at several hundred Hz with an amplitude of several MHz. Unfortunately the signal-to-noise ratio on the transition signal at high frequencies (above 500 Hz) is too poor to allow adequate locking of the PBC directly to the transition peak. Thus we must stabilize the PBC resonance frequency first, before trying to lock to the transition peak. We do this by establishing an intermediate lock to a more steady cavity. The piezo mount of the first mirror allows us to change the PBC resonance frequency quickly to compensate for a vibration of the whole unit.

The polarized spectrum analyzer (PSA) is a very stable cavity constructed of Invar and brass, with two 5 cm spherical mirrors mounted in the brass end-pieces. The metal parts are designed with thermal expansion effects in mind: the brass pieces indent slightly into the Invar tube, so that their large thermal expansion will nearly cancel the small expansion of the Invar tube. There is a high-quality laser window inserted in the beam path at Brewster's angle, causing the cavity to support only one polarization. Tuning is accomplished by tilting this window slightly using a galvanometer driver similar to those in the laser.

This cavity was constructed to allow us to stabilize the laser using the technique of Hänsch and Couillaud.[54] The amplitude of the

imaginary component of the wave reflected from the front of the cavity has the dispersion shape we desire for locking to the resonance. We can extract this amplitude by arranging for interference between the light that comes directly off the front mirror and the light that has resonated in the cavity and leaked back out. Since the cavity polarizes the light that resonates, the two waves can be distinguished by their polarization. The interference then is detected as an intensity difference on two photodiodes and used as the error signal for locking the laser to the cavity.

This system is used to derive the error signal for locking the PBC resonance to the PSA resonance. Again, the signal is filtered before being sent to the high-voltage amplifier that controls the piezo on the PBC. One advantage of this locking technique is that the bandwidth of the signal is limited chiefly by the speed of the photodiodes and electronics used. Since photodiodes with very high bandwidth can easily be found, and since the piezo-mirror mount on the PBC is the major bandwidth limitation in this locking loop, this advantage is almost completely irrelevant. The disadvantage of offset drifts is also of minor importance, since our main goal is to stabilize the frequency rather than to lock exactly at the peak of the PSA transmission. The major advantage is that the PSA has excellent long-term stability.

The laser frequency is now tuned onto the transition peak using the tilt of the window in the PSA cavity. The tilt is controlled by varying the current sent through the galvanometer coil; we use a current-regulating amplifier. We lock the laser frequency to the transition peak by applying feedback to this current. The error

signal for this lock is derived from a standard dither lock: the laser frequency is modulated at 330 Hz and the resulting modulation on the transition signal is analyzed by a lock-in amplifier. The 330 Hz modulation frequency was chosen because of the low detector noise there. Furthermore, we wanted to tune the modulation frequency far from the nearest harmonics of the 60 Hz line frequency: we see transition noise entering at the difference frequencies (ν − 300 Hz) and (ν − 360 Hz), probably due to line-locked detector pickup being heterodyned in the lock-in.

The laser frequency is quite stable as soon as the PBC is locked to the PSA: for short times, we can get transition noise to match the best performance without even locking the PSA to the transition. In only a few seconds, though, the PSA will drift off the peak, and the residual frequency noise begins to appear in the transition noise at first order. Therefore we need only arrange for a feedback signal to the PSA that corrects for very slow deviations. This is important, because the low bandwidth of the transition signal seriously limits our ability to see fast modulation of the transition rate.

The lock-in amplifier does the heavy filtering of the feedback signal; the RC filter is set for a 5 second time constant. The DC gain following this filter is quite large, to ensure that the detuning of the laser from the transition peak is always small. In addition, I developed a circuit which I call the "Automatic Graduate Student" (AGS) circuit (Fig.3-8), which continually resets this offset to zero. The circuit was designed to do the same task I was doing repeatedly: check the offset of the transition lock and change an injected offset manually to re-center the lock. The circuit does

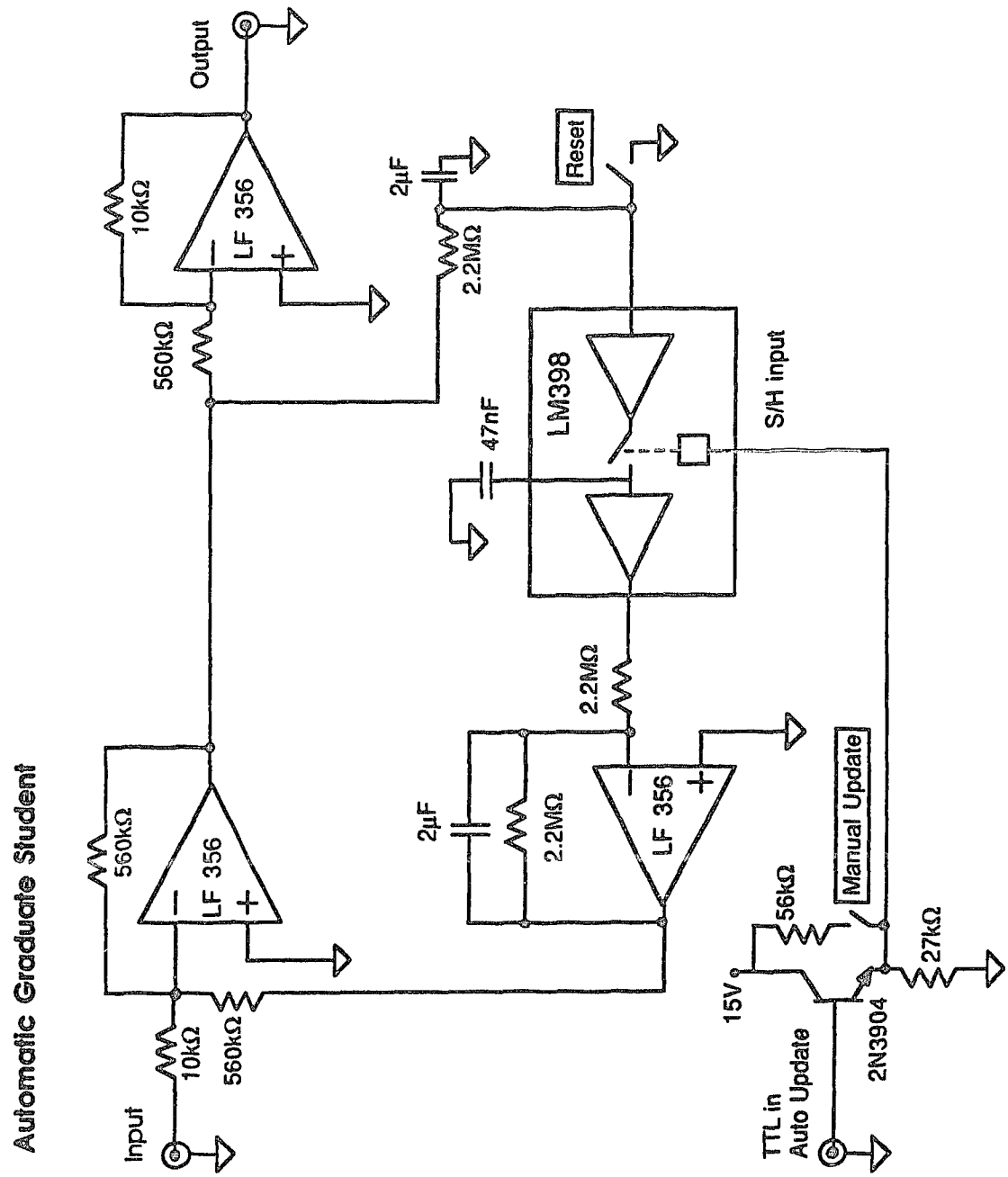
Automatic Graduate Student
Input
10kΩ
560kΩ
LF 356
560kΩ
Output
10kΩ
LF 356
560kΩ
2µF
2.2MΩ
Reset
47nF
LM398
S/H input
2µF
2.2MΩ
2.2MΩ
LF 356
15V
56kΩ
Manual Update
27kΩ
TTL in
Auto Update
2N3904

Fig. 3-8

this by measuring the offset of the lock-in signal and eventually shifting it from the lock-in to an offset stored in a sample/hold (S/H) circuit. The input of the S/H circuit is essentially just the DC offset of the lock-in signal. If this same offset is added to the lock-in signal before sending it to the PSA driver circuit, the lock-in signal will adjust to force the output of the AGS to maintain the same value (since the required input to the PSA driver has not changed). The offset required of the lock-in to satisfy this condition is zero, since its previous offset has been acquired by the S/H circuit. The S/H trigger frequency is not very important, although it should be slower than the filters that precede and follow the S/H, and faster than typical offset drifts. Note that this is not the same as adding a full-time amplifier to the basic locking system. That would simply divide the DC error by the gain of the new amplifer; it would also introduce the risk of new oscillations. The key feature of the AGS is intermittent sampling of the offset by the sample/hold circuit.

To be more specific, the offset of the lock-in signal must always be added to whatever offset already exists on the S/H output to select the new S/H output voltage; this addition is done in the first amplifier. Furthermore, the offset voltages to be acquired by the S/H must be fairly large, since the S/H cannot accurately hold offsets on the order of a few mV. Therefore, the lock-in signal must be amplified from its usual size of a few mV to a few volts before being sent to the S/H circuit. The signal can then be stepped back down to its original size at the output. This limits the useful range of the circuit, but it is rare for a system to be very

sensitive to mV offset drifts (as ours is) while also requiring several volts of range (which ours does not). It is fortunate for the human graduate student population that the capabilities of this circuit are so limited.

3.7 Intensity Stabilization

The intensity of the light in the cavity must be stabilized in order to keep the noise on the transition signal down. This intensity is measured with a photodiode placed at the output end of the PBC. Since the intensity in the cavity is proportional to the intensity of the light transmitted by the output mirror, stabilizing this photodiode signal is equivalent to stabilizing the cavity power.

The stabilization control circuit simply compares the photodiode signal to a reference voltage and amplifies the difference; the amplified, filtered difference signal is sent to a KD^*P Pockels cell (PC) to control the polarization of the light; and then the light is sent through a linear polarizer that discards the light that has been rotated into the wrong orientation. Thus we control the intensity of the PBC transmission by varying how much light we discard before the PBC.

The performance of this system has also been dramatically improved since our earlier measurements. The noise on the intensity signal from the photodiode depends on the location of the laser spot on the surface of the detector and sometimes on its angle of incidence. When we remounted the photodiode on a very rigid mount and then carefully aligned it to find a stationary point, we were

able to get fractional transition signal noise of less than $2.2 \times 10^{-5}/\sqrt{\text{Hz}}$ – a factor of 4 lower than previously possible. An additional help is the switch to an air-suspension system to keep strong building vibrations from shaking the laser, the PBC, and the PBC-transmission photodiode. This air-suspension system allows us to get good data at all times of day; before this, we could only get our best data at night.

The stabilization circuit also generates a square-wave voltage to add to the reference voltage; this square wave is derived from the same TTL logic signal that controls the polarization flip. Its amplitude is selected by front-panel controls. This system (which we called the ΔP feedforward system) allows us to force the intensity at the photodiode to modulate with the polarization flip. This capability is necessary for reasons that will be given later.

The photodiode signal has large amounts of noise at high frequencies (5 kHz→50 kHz), due to the rapid fluctuations in the laser frequency around the resonance peak. This noise is filtered slightly (LPF at 70 kHz) before the stabilization circuit. Inside this circuit, there is only one LPF: the main filtering at 3 Hz. Again, there is large DC gain after the filter, including a high-voltage amplifier at the end. The high-voltage signal travels down a long shielded twisted-pair cable to the Pockels cell. The cable has an unfortunately high capacitance, which limits the bandwidth heavily: the oscillation frequency is only about 3 kHz. However the stability we achieve is better than $10^{-6}/\sqrt{\text{Hz}}$; this is more than ten times quieter than the noise on the transition under the best of conditions. Furthermore, increases in the gain on the intensity lock

eventually begin to interfere with the dye-to-PBC frequency lock, making it harder to keep the laser locked for long periods. We believe that this comes from intensity modulation causing noisier signals on the fast photodiode of the PBC error-signal system.

The transition signal was found to be much quieter when we included a linear polarizer before the photodiode that measures the PBC transmission. This is probably due to the slight detuning of the resonant frequencies for the two polarizations, which arises from the coating birefringences of the mirrors. This birefringence produces a slight path length difference for the components of the light polarized along each of the birefringence axes (see Appendix B); this in turn implies that the resonant frequencies are slightly different. The addition of the analyzing polarizer after the PBC allows us to stabilize just the intensity component that excites the transition.

However, it then becomes necessary to apply a P-flip modulation to the photodiode signal to allow the modulation of the intracavity power to be kept at zero. If the light in the cavity were very close to circular and the ΔP modulation of its x and z components were zero, there would still be a modulation of each of the components of the light after the output mirror due to the birefringence of the mirror substrate. If we were to stabilize the z component of the intensity to a constant (non-modulating) value, the total intensity in the cavity would acquire a modulation and impart it to the transition rate. Instead we must modulate the reference level before stabilizing the intensity to it; we select an appropriate modulation amplitude to null the modulation in the transition rate. This added

modulation is produced by the ΔP feedforward system mentioned earlier.

3.8 Polarization Control

The experiment requires very accurate circular polarization of the light in the cavity, with the capability to reverse the handedness of the polarization accurately. The device we use for controlling this polarization is another KD^*P Pockels cell (PC) with its electric field along the laser path and its birefringence axes along the x and z directions as defined in the interaction region. It has a low residual birefringence at zero voltage, and its 1/4-wave voltage is around 1850 V.

Because the residual birefringence is found to be very sensitive to temperature, we placed the PC inside a small "oven" that maintains a temperature near 30° C. The temperature controller is an inexpensive AC proportional controller manufactured by Cwen Industries. The mounting system was designed to minimize the heat-conductive path from the oven to the PC so that fast temperature changes of the oven would not be efficiently transferred to the PC inside. Birefringence drifts are now less than 5×10^{-4} per hour.

The initial alignment of the polarization PC is accomplished as follows. Crossed linear polarizers are placed before and after the PC; a diffuser like Scotch tape is placed just before the PC. The scattered light that passes through the second polarizer falls in a concentric ring pattern with an extended cross through the center.

The PC is tilted until the cross pattern is centered on the spot that the laser hits when the tape is removed.

The voltage for the PC is supplied by a stable high-voltage supply; the reversal of this voltage is accomplished with a high-voltage relay that alternately reverses the connections between the PC and the supply. In addition, it is necessary to add a compensating voltage overshoot at each reversal of the relay to obtain accurate 1/4-wave birefringence immediately after the flip. We use a high-voltage square wave signal filtered with an AC-coupling circuit to generate the necessary compensating voltage. This voltage is applied to one terminal of the PC, and the bipolar voltage from the relay is applied to the other terminal. One output terminal of the relay is grounded while the other swings between positive and negative high voltages.

The diagnostic tool we use to optimize the operation of the PC voltage control system is the intensity of a beam that we dubbed the PURC signal ("polarization un-rotated component"); this is the beam that bounces off the PBC and passes back through the PC, but is not kicked out at the output polarizer of the Faraday isolator. If the PC were set exactly right, the polarization at the PBC would be exactly circular and the beam would be changed back to linear upon returning through the PC; the returning polarization would be orthogonal to the original, and so all the light would be kicked out at that linear polarizer. However, if the PC birefringence is not exactly 1/4 wave, some light passes through to the input polarizer of the Faraday isolator. We therefore set the compensator and the high-voltage signals to minimize this signal.

One of the important new systematic contributions turns out to be driven by the vertical intensity component of the laser $|\tilde{\epsilon}_x|^2$; by comparison, most of the other terms in the transition rate on the transition peak we use are proportional to $\tilde{\epsilon}_x\epsilon_z$ or ϵ_z^2. The control of this systematic term depends heavily on being able to limit the modulation in $|\tilde{\epsilon}_x|^2$ with the polarization flip, since the term already has explicit E- and B-flips. This term will be discussed in more detail in Section 4.3. As part of the solution to this problem, we designed a system to monitor the modulation of $|\tilde{\epsilon}_x|^2$ in the PBC.

For this task we use a beamsplitting polarizer for the analyzing polarizer; the two beams are sent to photodiodes. One photodiode is sent to the intensity stabilization circuitry as usual. Both photodiode signals are also sent to amplifiers that produce the sum and difference of the signals. The difference signal is set to zero by rescaling the signal from the $|\tilde{\epsilon}_x|^2$ photodiode, so that equal absolute modulation size on each signal would imply equal fractional modulation as well. Then the P-flip modulation of the sum signal is monitored as a measure of the modulation of $|\tilde{\epsilon}_x|^2$ within the cavity.

To understand this system we must first realize that a change in a birefringence in the system causes equal and opposite changes in the modulation amplitudes of the ϵ_x^2 and ϵ_z^2 signals (see Appendix B). Thus in the absence of intensity stabilization, a birefringence change will have no effect on the sum-signal modulation. However, the modulation of the ϵ_z^2 signal is fixed by the ΔP feedforward and the intensity stabilization; therefore a change in the birefringence will show up as a change in the P-flip modulation of the ϵ_x^2 signal only, and hence it will also change the sum-signal modulation. The

reason that we don't want to use the difference-signal modulation as our measure is that it already has a huge modulation on it, which would then only show small changes with drifts in the birefringence. By comparison, the sum signal has nearly zero modulation at the desired operating point.

We tested this system by arranging the Pockels cell and ΔP feedforward to null the modulation of the β transition ($\Delta F = \pm 1$; proportional to ϵ_z^2 in the cavity) and the sum signal from the two photodiodes; we then checked the modulation on the α transition ($\Delta F = 0$; proportional to $|\tilde{\epsilon}_x|^2$) to check whether the P-flip modulation in $|\tilde{\epsilon}_x|^2$ was indeed zero. We found a good linear relationship between the modulation of the α signal and the modulation of the sum signal from the photodiodes, with nearly zero offset; this shows that the sum signal is a good indicator of the modulation of $|\tilde{\epsilon}_x|^2$ in the cavity. The best way to control the modulation of both signals (α and photodiode) is by tilting the Pockels cell slightly; this introduces a small birefringence just before the PBC.

There is often a different daily value of the relative offset between the zero-modulation positions for the α signal and the sum signal from the photodiodes. The offset appears to be independent of the laser frequency (which we tested by comparing results from the two $\Delta F = 0$ transitions and the two $\Delta F = \pm 1$ transitions). Because of this uncertainty in the offset, we measured it before every day of PNC data.

3.9 Computer System

The computer system is another crucial part of the experimental apparatus. It controls the reversals of the polarization, electric field, and magnetic field (in a complex switching pattern); the operation of the gated integrators; and the digitization and storage of the results.

The machine processor is the LSI 11/23 made by the Digital Equipment Corporation. The data-taking programs were written in FORTRAN 66. Additional hardware includes a programmable clock, a 12-bit 8-channel A/D converter, a 12-bit 4-channel D/A converter, a 16-bit in/16-bit out parallel line unit, and a Weinberg-angle meter.

The programmable clock provides all of the timing information for the operation of the gated integrator; all of the field reversal timing is based on this integration cycle. The timing of the polarization flip is carefully regularized because the PC compensator circuit is sensitive to irregularity in the timing.

The control of the experiment is mainly carried out through the parallel line unit. The 4 most-significant bits of the PLU output are connected to buffer drivers with optoisolator outputs: these are important for keeping switching transients from travelling back to the computer and confusing the PLU driver circuits. We use three of these to control the polarization, electric field, and magnetic field flips. The gate and reset inputs of the gated integrators are controlled by two of the unbuffered outputs of the PLU. All of the remaining outputs of the PLU are unused.

The switching waveforms for the three fields are somewhat complex. The polarization is reversed after every integration period (about 2 Hz); the electric field is reversed (E-flip) after every 5 full P-flip cycles; and the magnetic field is reversed (B-flip) every 5 full E-flip cycles. The complication is in the phase reversals. After every full cycle of the B-flip, the polarization flip is phase-reversed; and after every *other* full cycle of the B-flip, the electric field flip is phase-reversed. The phase reversal consists of inverting the P- or E-flip signal (in the program) so that transitions of P, E, and B do not always occur in the same way for all of the data (e.g. both going to logic high at the same time). Instead, half of the data is taken with these coinciding flips happening one way, and half is taken with the opposite phase relationship. This reduces the chances that a transient from the flip of one variable would always produce a spurious contribution of one sign; instead, such a contribution would tend to average to zero after a long period of data-taking.

The gated integrators are made by Evans Associates. The circuit integrates the input voltage as long as the gate input is on; when the gate is turned off, this value is held until the reset input is operated. The control inputs are standard TTL signals; the gate period can be as short as 30 nsec. The integration time constant is selected by an external capacitor. We use selectable time constants of 0.1, 1.0, and 10 msec; we finally used the 10 msec time constant for all of the PNC data. The integrator time constants, the programmable clock, and the A/D conversion scale coefficient were calibrated together by sending a known voltage (measured with a

voltmeter) into the signal input and recording the values measured by the computer A/D converters.

3.10 Summary of Improvements

Many things were vastly improved to perform this new measurement of parity nonconservation. One of the most dramatic was the improvement in the PBC through the use of much better mirrors. These mirrors give more than five times the intracavity power we had previously, and the systematic effects from the birefringence of the output mirror coating are reduced by more than a factor of 25 (to less than 2% of the PNC signal). The frequency stabilization system was also vastly improved in order to take advantage of these high-quality mirrors. Previous estimates of our laser linewidth when stabilized were around 500 kHz peak-to-peak; current estimates are closer to 30 kHz. Our measurement errors in the calibration of the mirror-coating-birefringence systematic term were reduced by the delicate mounting of the PBC input mirror (to reduce stress-induced birefringence that depends on PBC tuning), and by the improvements in the technique for taking the tilted-collimator measurement itself. These improvements in the tilted-collimator measurement include the use of measurements at a symmetric opposite tilt to cancel effects due to various substrate-birefringence effects rather than the atoms.

The switch to coated quartz field plates and a 5 mm spacing vastly reduced the scattered light, the drift in the scattered-light background level, and the noise coming from this scattered light. It is now possible to take PNC data in which the scattered light noise

does not contribute. Another noise source that was greatly reduced was the noise in the measurement of the PBC transmission; since this signal is used for stabilizing the power in the cavity, this greatly reduced the noise on the transition signal also (by a factor of 4).

The remounting of the detector box enables us to tilt it to large angles to measure a factor in a certain PNC systematic term (B_x/B_z), and then tilt it back to null out a factor in another term (E_y/E_x). This is a significant improvement over the old system of trying to select an E_y/E_x value that is large enough for making the B_x/B_z measurement and small enough that its own systematic term won't be too large. It is also much superior to attempting this procedure using shims placed under the detector by hand, based only on previous data on the value of E_y/E_x. Now we can set a large value, and then null it out in minutes through successive measurements of E_y/E_x.

The air suspension system isolates the table from vibrations of the floor, reducing noise in vibration-sensitive systems like the PBC frequency and the PBC transmitted-intensity stabilization. This also means we can take PNC at any convenient time of day rather than being forced to wait for the quietest hours of the day – 7 pm to 7 am. (An unnamed researcher has already seen too many sunrises from the wrong side, for just that reason).

With these modifications we have increased our PNC signal-to-noise to the point where we could make daily measurements with almost the same precision as our entire first measurement run (which took more than 30 days). This is the only reason that it was practical to push forward to this new lower measurement uncertainty.

CHAPTER IV

SYSTEMATIC EFFECTS

The most important features of any PNC experiment are the signal-to-noise ratio and the control of systematic effects. The effect we are measuring is so extraordinarily small that the quality of an experimental design can be judged entirely on the integration time required for a PNC measurement and the immunity to systematic effects. In this sense our experiment has a big advantage over all of the experiments that use a vapor cell, since we have control of one important parameter: the velocity distribution of the atoms. In addition, the effects of molecules and blackbody background are virtually eliminated. Another advantage of our system is the high PNC signal-to-noise we have achieved.

In our experimental apparatus, the field arrangement is simple enough that we can write down all possible combinations of these fields that contribute to the transition rate. This is a very powerful tool, since we can then identify all of the important systematic contributions directly and then work to measure and reduce them.

Many improvements were made in the apparatus which allow better control of the systematics. Among these is the addition of a drive motor to allow careful adjustment of the field misalignment E_y/E_x while the system is under vacuum. This allows us to use a large

field tilt while we measure another field misalignment (B_x/B) and then set a small field tilt to reduce the systematic term that depends on E_y/E_x itself.

Many of these corrections are the same as those described in Sarah L. Gilbert's thesis,[49] but we also discovered one new term. Explicit expressions for many of the systematic terms appear at the beginning of many of these sections; all of these expressions are derived in Appendix C. First we will discuss the dilution of the PNC measurements by the overlap of transition peaks from adjacent m_F levels. Then we will consider the standard M1 correction due to the coating birefringence of the output mirror of the PBC. Next we will discuss the new M1 term in detail in Section 4.3. Then we will cover the ΔE terms that involve stray electric fields and various field misalignments. Section 4.5 then gives typical measurements of each of these systematic terms. Then we will discuss possible "apparatus" systematic effects that do not involve the atoms at all. We will conclude this chapter with a discussion of the noise sources.

4.1 Dilution Factor

The linewidth of the transition under normal conditions is dominated by inhomogeneous broadening from Doppler shifts. The line is about 24 MHz FWHM, with a "pedestal" which has a height of a few percent of the peak and a width around 580 MHz. This pedestal results from a background gas of cesium in the interaction region. Since the separation between adjacent $\Delta m = \pm 1$ peaks from the different m_F levels in our usual magnetic field is about 50 MHz,

there is significant overlap of the peaks from different m_F levels. Since each peak has a different fractional PNC modulation, the observed fractional PNC modulation on each peak will be changed by the inclusion of the modulation signals from overlapping peaks.

The relative sizes of the rate contributions for the $|E1_{ST}|^2$ and $E1_{ST} \cdot E1_{PV}$ terms are determined by the $C_{Fm}^{F'm'}$ coefficients appropriate for the ground- and excited-state quantum numbers. These constants are listed in Appendix A. Since all but the outermost two peaks in the Zeeman spectrum contain both a $\Delta m = +1$ term and a $\Delta m = -1$ term, the contributions for those peaks are determined by a sum of the squares of two $C_{Fm}^{F'm'}$ coefficients. For rate terms like the M1 and $E1_{PV}$ interference terms, the amplitudes for $\Delta m = +1$ and -1 have opposite signs, and thus the contribution on each peak is given by the *difference* of the squares of the $\Delta m = +1$ and -1 coefficients. By this recipe we find that the $|E1_{ST}|^2$ rates for the eight peaks in the Zeeman multiplet are in the ratio (14:11:9:8:8:9:11:14). For the $E1_{ST} \cdot E1_{PV}$ interference term, the ratio is (14:10:6:2:−2:−6:−10:−14).

It is precisely this difference in the ratios for the two types of rate contribution that compels us to calculate a dilution correction to the size of the measured fractional PNC. The PNC modulation is modified in one way by the overlap of the lines, and the size of the average transition rate is modified in another. Thus the fractional modulation is different in the presence of overlap from other lines.

An additional contribution was calculated. The $\Delta m = 0$ peaks that appear due to mixing of hyperfine states by the B_Z field (see Section 4.3 and Appendix C) also contribute to the $|E1_{ST}|^2$ rate but

not to the PNC. The ratio of these peak heights to the height of the outermost $\Delta m = -1$ peaks is

$$\frac{\alpha^2}{\beta^2}\,(\delta_6-\delta_7)^2\,\frac{\left(C_{Fm}^{F'm}\right)^2}{\left(C_{Fm}^{F'm'}\right)^2} \qquad (4\text{-}1)$$

On the same scale as the $|E1_{ST}|^2$ ratios given above, the $\Delta m = 0$ contributions to the $|E1_{ST}|^2$ rate for $B_Z = 74$ G are in the ratio $(7:12:15:16:15:12:7) \times 0.1273(15)$ for the seven $\Delta m = 0$ peaks.

The procedure used during both of our measurements of PNC is as follows. We take a frequency scan of the transition with and without the 74 G magnetic field, recording it on an X–Y plotter. On the picture of the scan taken in a 74 G field, we measure the relative frequency offsets of the eight transition peaks. The distances from each end peak to each of the other seven peaks are recorded; in addition, the positions of the $\Delta m = 0$ peaks are estimated by calculating the midpoint between adjacent $\Delta m = \pm 1$ peaks. Then on the scan taken at zero field, we mark out these distances from the position of the peak. At these frequency offset positions (and at the peak) we measure the signal size from the graph. This set of signal measurements is used as the measure of the amount of overlap of each of the other peaks onto the end peak (to which the laser is locked during PNC data).

Then we scale these signal measurements by the ratios given above and add them to calculate the modified sizes of the $|E1_{ST}|^2$ and $E1_{ST}\cdot E1_{PV}$ rate terms. The ratio of these sums is the ratio of the factors by which each rate term is modified by the overlap. This is the dilution factor by which we scale the PNC measurements.

4.2 Normal E1·M1 Interference Terms

$$\text{abcd}' \frac{M1}{\beta E_X} \frac{\Delta(\epsilon_Z^2)}{\epsilon_Z^2} \frac{\omega_L}{\omega_D} \frac{\theta_T}{\theta_D} \times (\text{lineshape factor}) \qquad (4\text{–}2)$$
(Collimator tilt + P-flip in ϵ_Z^2)

$$\text{abcd}' \frac{M1}{\beta E_X} \frac{\epsilon_{I1}}{\epsilon_{Z1}} \varphi \sin 2\theta \qquad (4\text{–}3)$$
(Output mirror birefringence)

ω_L: laser detuning ω_D: Cesium beam Doppler linewidth

θ_T: collimator tilt angle θ_D: Cesium beam divergence angle

One of the most serious systematic terms in all PNC experiments that use mirrors in various power-buildup schemes is the cross-term between the M1 transition amplitude and the applied $E1_{ST}$ amplitude. Because the M1 amplitude is 20,000 times larger than the PNC amplitude, we must suppress the M1 by an enormous factor. It does not help that in our experiment the E1·M1 interference term flips with three of the four variables with which the PNC term flips. Fortunately the normal E1·M1 contribution is suppressed by the cancellation of signals from the opposing travelling waves in the PBC. Still, the E1·M1 terms must be strongly suppressed by the polarization flip.

One of the simplest ways that the E1·M1 term might acquire a P-flip modulation is if the P-flip modulation in ϵ_Z^2 is large and the cancellation of the E1·M1 term in the standing wave is incomplete. In this case, the fractional modulation of the E1·M1 with E, B, and m_F is multiplied by the fractional P-flip modulation in ϵ_Z^2 to give a net component that modulates with all four variables. The P-flip

modulation in ϵ_z^2 could arise from improper setting of the ΔP feedforward system in the intensity stabilization system. As described in Section 3.7, the feedforward system normally impresses a fixed modulation onto the intensity of the z-component of the light transmitted through the PBC; this modulation compensates for birefringences, allowing the intensity inside the PBC to remain constant. If the modulation size is incorrect, the intensity inside the PBC acquires an overall modulation, causing a modulation of ϵ_z^2. Poor cancellation of the E1·M1 would arise if the collimator tilt were set incorrectly and the laser frequency were slightly to one side of the line center (see Section 4.3, Appendix B, and Chapter 6). This is simple to control: the P-flip modulation can be held consistently to less than 10^{-4} by careful selection of the ΔP feedforward value, and the E1·M1 term can be reduced to less than 5×10^{-4} by setting the proper value of collimator tilt. Throughout the PNC data, the modulation of ϵ_z^2 is always less than 2.5×10^{-4} and the $\Delta E \Delta B$ modulation due to the normal E1·M1 term is in the worst case as high as 2×10^{-3}, yielding a maximum correction of about 2% of the PNC term. Since the P-flip modulation of ϵ_z^2 drifts both positive and negative, this type of correction averages out over a large data sample.

A more serious problem is the possibility that the precise cancellation of the two travelling waves in the PBC (and hence the cancellation of the E1·M1 term) would fail in a polarization-sensitive way. A coating birefringence on the output mirror would do exactly that. Although the intensities of the incident and reflected waves would be nearly the same, their polarization would be

different, so that the E1·M1 amplitudes would not cancel; most important, this failure to cancel would be sensitive to the incident polarization. Calculations presented in Appendix B show that such a term proportional to the birefringence of the output mirror coating can occur. This term is not easy to control; the only choices are to rotate the mirror until its birefringence axes are parallel to the x and z axes, or (if this proves too difficult) to replace the output mirror. Our apparatus is well arranged for measuring this birefringence (unlike every other PNC experiment), but it is not arranged to enable nulling of this term while under vacuum.

The factor $\varphi \cdot \sin 2\theta$ that appears in the expression for this systematic can be measured directly in the following way. We tilt the collimator far over to one side so that almost all of the atoms emerge with a high Doppler shift of a particular sign. This allows us to resolve the two transition peaks due to excitation by each PBC travelling wave alone. While stabilizing the x-component of the PBC transmission, we monitor the signal on the $\Delta F = 0$ transition, measuring the P-flip of the signal on the one peak (corresponding to one travelling wave) and then on the other peak. In this way we can detect very slight differences ($\Delta P \Delta k \lesssim 10^{-5}$) in the polarization of the two travelling waves. The calculations in Appendix B show that this tilted-collimator measurement gives a direct measure of the factor $\varphi \cdot \sin 2\theta$.

There is a significant problem with drifts in the polarization when taking these measurements. Birefringence drifts can be separated into two classes: those that change the P-flip modulation of the transition signal ($\Delta \epsilon_x^2$) and those that only change the P-flip

modulation of the other polarization ($\Delta\epsilon_Z^2$). These groups are natural since drift in $\Delta\epsilon_X^2$ is immediately visible in the tilted-collimator data but drift in $\Delta\epsilon_Z^2$ is not; also, the two groups generally correspond to whether the optics causing the birefringence drift follow or precede the PBC (see Section B.2).

We might assume that the tilted-collimator measurement is fairly insensitive to drifts in $\Delta\epsilon_Z^2$, since the transition signal modulation is just given by $\Delta\epsilon_X^2$. However, we find that drifts in $\Delta\epsilon_Z^2$ correlate with drifts in the ΔP difference between the k^+ and k^- peaks ($\Delta P\Delta k$). Since we use these $\Delta P\Delta k$ differences as the measure of the mirror birefringence, a drift in this quantity can affect the final result. We do not have a theoretical understanding of this effect.

We can check for drift in $\Delta\epsilon_Z^2$ by measuring the P-flip modulation of the transition signal when the analyzing polarizer is removed. In this case, the total intensity is held constant; but ϵ_Z^2 and ϵ_X^2 in the PBC modulate with equal size and opposite sign (see Appendix B), causing modulation of the transition signal. We usually perform this measurement before each short set of $\Delta P\Delta k$ measurements, tilting the Pockels cell to null the modulation of ϵ_X^2; then we recheck this measurement after the data set to see if there has been a large drift. Data sets are discarded if $\Delta\epsilon_Z^2$ changes substantially (more than about 2×10^{-4}).

Our technique for measuring the output mirror birefringence has become more refined as our mirror quality has improved. For our previous measurement of PNC we took measurements only with a single direction of collimator tilt; we now take measurements with the collimator tilted both ways, to reduce the effect of $\Delta P\Delta k$ offsets

caused by polarization errors. We have tried hard to stabilize the mirror temperature carefully to reduce its birefringence drifts. And we are far more selective in dropping data sets that show large ΔP drifts of either type. Typical measurement runs include six or more 20-minute data sets, each of which contains data with both values of collimator tilt. Of these six, we usually only get three sets with small enough ΔP drifts; these three also usually agree within their uncertainties, whereas the other sets usually do not.

4.3 New E1·M1 Systematic Term

$$\text{abcd'f}\,\frac{\alpha}{\beta}\,\frac{M1}{\beta E_x}\,\frac{\Delta(\epsilon_x^2)}{\epsilon_z^2}\,\frac{\theta_T}{\theta_D} \times (\text{lineshape factor}) \qquad (4\text{–}4)$$

As discussed in Chapter 2, the E1·M1 interference term changes sign with the laser propagation direction; thus the contributions from the opposing travelling waves in the standing wave tend to cancel. These two contributions are usually nearly equal; however, if the cesium beam is tilted slightly to one side or the other, the atoms may no longer absorb equally from the two travelling waves due to their Doppler shifts. If the laser is tuned exactly to the center of the rest-frame transition frequency of the atoms, the contributions from the two travelling waves will still very nearly cancel. But as we will discuss in Chapter 6, an asymmetry in our lineshape causes the laser to lock just to one side of the line center. In this case, one travelling wave finds more atoms on resonance than the other, and we get a large uncancelled contribution from the E1·M1 term (since this contribution flips with E, B, and m_F,

but not P, it is not a PNC systematic term). So as long as the laser is locked off the line center, any tilt will allow a large E1·M1 contribution to the transition rate. This provides a useful measure of the tilt of the cesium beam as we adjust the collimator tilt.

We have found that we can also get a large E1·M1 contribution from the $\Delta m = 0$ transition peak immediately adjacent to the $\Delta m = \pm 1$ peak we use. This transition peak is very small, since it only occurs due to the mixing of different hyperfine levels by the B_Z field (see Chapter 2). In normal scans of the transition in a 74 G magnetic field, the $\Delta m = 0$ peaks are only visible as small bumps nestled in the dip between peaks (see Fig 2-4b). Due to the overlap of the Doppler-broadened peaks which we discussed earlier, there are many atoms whose Doppler shift is equal to the Zeeman splitting between the adjacent transition peaks. Thus we have many atoms undergoing $\Delta m = 0$ transitions by absorbing at the frequency of the $\Delta m = \pm 1$ transition.

The calculations presented in Appendix C include the calculation of the E1·M1 rate term for the $\Delta m = 0$ and ± 1 transitions. The E1·M1 rate term for the $\Delta m = \pm 1$ transition peaks is proportional to ϵ_Z^2; this fact accounts for most of the suppression of the P-flip in the normal E1·M1 contribution, since the β transition rate is also proportional to ϵ_Z^2 (see Appendix B). However, the E1·M1 rate term on the $\Delta m = 0$ peak is proportional to ϵ_X^2; since common birefringence effects can cause P-flip modulation of ϵ_X^2, this E1·M1 term may modulate with P even if ϵ_Z^2 (and hence the main $E1_{ST}$ rate term) is not modulating with P.

Crude simulations of the frequency dependence of the E1·M1 term have been performed using a gaussian Doppler distribution for the atoms; tilt is simulated by changing the offset of the center of the gaussian. These simulations indicate that the new E1·M1 term may contribute a $\Delta E \Delta B \Delta m$ signal as large as 25% of the old E1·M1 term. Our data bears this out: the $\Delta E \Delta B \Delta m$ measurement on the $F=3 \rightarrow F'=4$ transition is as much as 2.3 times the $\Delta E \Delta B \Delta m$ on the $F=4 \rightarrow F'=3$ transition. Since the $\Delta m = 0$ E1·M1 term has opposite sign for each of these two lines, the measurements of the sum of the old and new terms give a ratio much different from the usual value of 1.44 (the ratio of M1 amplitudes for $\epsilon_x^2 = 0$).

To explain the m-flip of this $\Delta m = 0$ contribution, we need to know the laser-frequency dependence of the E1·M1 terms. If we tilt the collimator toward the input mirror, we add an offset to the velocity distribution; there are more atoms moving toward the input mirror than away from it. For a negative detuning of the laser, the atoms that are moving toward the input mirror are resonant with the downstream-moving travelling wave (k^+)in the PBC; for a positive detuning of the laser, those atoms are resonant with the other travelling wave (k^-). Then if the laser is tuned to the negative side of the line center, the E1·M1 rate term in the atoms moving toward the input mirror is chiefly excited by the k^+ wave; since there are fewer atoms moving toward the output mirror (and being excited by the k^- wave), the sum of the E1·M1 contributions from the two waves is dominated by that of the k^+ wave. Likewise, if the detuning is positive, the net E1·M1 rate is dominated by the signal from the k^- wave. Since the E1·M1 signals from the k^+ and k^- waves

have exactly opposite sign, the net E1·M1 signal will change sign with detuning. The result is that the E1·M1 term has a dispersion shape whose width is roughly that of the Doppler distribution of the atoms; the center of the curve is at the zero-velocity line center. The peak-to-peak size of this dispersion curve is roughly proportional to the tilt of the collimator.

We can see now that the contribution from the $\Delta m = 0$ peaks will change sign if the laser detuning changes sign. But we know that this detuning does reverse every time the laser is tuned from one end of the Zeeman multiplet to the other (the m-flip). When we tune to the lowest-frequency ($\Delta m = -1$) peak, the nearest $\Delta m = 0$ peak is on the high-frequency side; and when we tune to the other end of the multiplet ($\Delta m = +1$), the nearest $\Delta m = 0$ peak is on the low-frequency side.

Since we know that locking the laser to the transition peak actually sets it slightly to one side of the line center, we can also see that the $\Delta m = \pm 1$ E1·M1 term should only be visible at PBC intensities high enough to cause a lineshape asymmetry. We have verified that the sensitivity of the E1·M1 term to the collimator tilt is sharply reduced at low PBC intensity.

Now we must reverse the question: if the laser is detuned by $\Delta\nu$ from the center of the line, then at what value of collimator tilt will an E1·M1 contribution be cancelled in the standing wave cavity? The cancellation of the E1·M1 is achieved by balancing the number of atoms excited by the k^+ wave with the number excited by the k^- wave. When the collimator is tilted so that the number of atoms with Doppler shift $+\Delta\nu$ is equal to the number with a Doppler shift of $-\Delta\nu$,

the E1·M1 terms will exactly.cancel. For cancellation of all of the E1·M1 terms, this balance must be established simultaneously at all relevant values of laser detuning.

This has important ramifications for the nulling of the collimator tilt. We used to think that we could find a value of collimator tilt at which the E1·M1 terms were all zero. But since the old and new E1·M1 terms correspond to two separate groups of atoms distinguished by their velocities in the cesium beam, the collimator position for nulling the $\Delta m = \pm 1$ E1·M1 interference term will not necessarily be the same as for nulling the $\Delta m = 0$ E1·M1 term. The atoms that contribute a $\Delta m = 0$ E1·M1 term all must have a Doppler shift near 25 MHz (equal to the Zeeman separation between the two transition peaks); the $\Delta m = \pm 1$ contributions all come from atoms whose Doppler shift is equal to the offset of the distorted peak from the line center (about half the natural linewidth of 3.3 MHz). We have no reason to believe that the asymmetry in numbers at high Doppler shift should be the same as at low Doppler shift.

In practice, the two types of E1·M1 contribution seem to be linearly related over a wide range of collimator tilt angles, but often with a significant offset. From the calculated sizes of these E1·M1 terms, we predict that the $\Delta E \Delta B \Delta m$ modulation of the transition signal as a function of a scaled collimator tilt $\underline{t}$ will vary as

$$\begin{aligned} M1_4(t) &= M1_4^0\Big[(t-t_1) + \eta(t-t_0)\Big] \\ M1_3(t) &= M1_3^0\Big[(t-t_1) - \eta(t-t_0)\Big] \end{aligned} \qquad (4\text{–}5)$$

where η is the ratio of the $\Delta m = 0$ and $\Delta m = \pm 1$ E1·M1 contributions at the $\Delta m = \pm 1$ peak, $M1_4^9$ and $M1_4^8$ give the absolute size of the modulation for each hyperfine line, and t_0 and t_1 are the nulling positions for the $\Delta m = 0$ and $\Delta m = \pm 1$ E1·M1 terms, respectively. The constant η includes lineshape factors from both types of E1·M1 contribution and the polarization dependence of each, but it is independent of the collimator tilt and the choice of hyperfine line. The constants M^0 are proportional to the M1 amplitudes on each hyperfine line. This functional form allows for the tilt offset between the two nulling positions.

We performed several tests to determine what controls the offset between the null positions for the old E1·M1 term ($\Delta m = \pm 1$) and the new term ($\Delta m = 0$). Our first guess was that a relative tilt between the nozzle and the laser path was forcing us to adjust the collimator tilt to compensate; the high-Doppler-shift atoms perhaps were affected differently by the collimator tilt than the low-shift atoms, resulting in different degrees of imbalance between $+\Delta\nu$ and $-\Delta\nu$. We attempted to affect the offset by tilting the oven relative to the chamber, hoping to change the nozzle tilt. However, significant changes in the tilt of the nozzle failed to cause any change in the relative offset between the null positions. We subsequently determined one variable that did affect this offset: the orientation of the array in its mount. We found that remounting the array after rotating it 180° around its longitudinal axis reduced this offset by more than a factor of three. We have not identified the feature of the array that accounts for this; our best guess is that it has to do

with the orientation of the capillaries. However, this does not explain well why tilting the oven and nozzle had no effect.

The E1·M1 contribution from the $\Delta m = 0$ peak then only contributes as a PNC systematic because of the combination of two errors: incorrect adjustment of both the collimator tilt and the polarization. The collimator tilt would ordinarily be adjusted to zero by trying to null the $\Delta E \Delta B \Delta m$ modulation on both of the $\Delta F = \pm 1$ lines at the same time. Since the two E1·M1 terms are usually nulled at different collimator positions, this criterion leads to confusion. In the early stages of the experiment, it was always assumed that both $\Delta F = \pm 1$ lines would have $\Delta E \Delta B \Delta m = 0$ at the same collimator tilt; the $\Delta E \Delta B \Delta m$ was only nulled on one line, and the other usually was not checked. This accounted for the incorrect adjustment of the collimator tilt. We now check the $\Delta E \Delta B \Delta m$ on both hyperfine lines and choose a compromise collimator position which minimizes both types of E1·M1 contribution. Since we have more direct control of the P-flip modulation of ϵ_Z^2 than of ϵ_X^2 (see below), we allow about 5 times larger values of $\langle \Delta E \Delta B \Delta m \rangle_F$ ($\propto \epsilon_Z^2$) than of $\Delta E \Delta B \Delta m \Delta F$ ($\propto \epsilon_X^2$).

The same hyperfine mixing that allows the α·M1 interference on the $\Delta m = 0$ peak also produces a large $\alpha \cdot \beta$ term which flips with polarization, B_y, and ΔF. This term accounts for the improper setting of the polarization. Before we installed the system that monitors $\Delta \epsilon_X^2$ (see Section 3.8), we would set the polarization by nulling the P-flip modulation of the signal with the analyzing polarizer removed. However, in the presence of a B_y field, the total P-flip modulation of the signal would include this $\alpha \cdot \beta$ modulation; nulling their sum would leave a substantial error in the

polarization. Since we would typically perform this adjustment once at the start of the day, the sign of this error was dependent on the choice of the hyperfine line on which we began taking data.

With the new ϵ_X^2 monitoring system, we calibrate the P-flip modulation of the α transition rate ($\propto \epsilon_X^2$ inside the PBC) against the P-flip modulation of the output of the monitoring system. We find the linear relationship between the modulation amplitudes of these two signals so that we can null the modulation of ϵ_X^2 in the PBC by observing the monitor output. This calibration is performed before each set of PNC data. The PNC data files also contain measurements of the output of this ϵ_X^2 monitor taken with every transition signal measurement; the data-acquisition program also displays average $\Delta\epsilon_X^2$ measurements after every B flip.

The analysis of the data for the calculation of the PNC correction is simple. Using Eq.4–5 we find that the $\Delta m = 0$ contribution to the observed $\Delta E \Delta B \Delta m$ modulation is given by

$$\begin{aligned} \left(M1_4\right)_{\Delta m=0} &= M1_4^0 \eta(t-t_0) = M1_4(t) - \frac{M1_4^0}{M1_3^0} M1_3(t) \\ \left(M1_3\right)_{\Delta m=0} &= M1_3^0 \eta(t-t_0) = M1_3(t) - \frac{M1_3^0}{M1_4^0} M1_4(t) \end{aligned} \qquad (4\text{–}6)$$

This simple calculation involves only the $\Delta E \Delta B \Delta m$ measurements $M1_4(t)$ and $M1_3(t)$ from the PNC data and the precisely known ratio $M1_4^0/M1_3^0$.

As we have said, the constant η includes the factor $\epsilon_X^2/\epsilon_Z^2$. Since the E1·M1 term already flips with E, B, and m, the PNC contribution from this term is given by product of $(M1)_{\Delta m=0}$ and the fractional P-flip modulation of η, which is just $\Delta(\epsilon_X^2)/\epsilon_Z^2$. The size

of this modulation can be derived from the ΔP measurements of the ϵ_x^2 system, as shown above.

We have found that drifts in birefringences caused typical short term (10–30 sec) drifts in $\Delta\epsilon_x^2$ on the order of 10^{-4}. We were able to see these drifts in the monitor signal during PNC data and in the P-flip modulation of the α transition rate during the testing. We have also found that the modulation observed on both the monitor and the α transition changes as we move the laser from one transition line to another; however, we also find that the linear relationship between the two modulation signals is unchanged.

4.4 <u>ΔE Terms</u>

$$-2\ \text{abcd}'\ \frac{\Delta E_y}{E_x}\ \frac{B_x}{B}\ \frac{\epsilon_I}{\epsilon_z} \tag{4-7}$$

$$-2\ \text{abcd}'\ \frac{\Delta E_z}{E_x}\ \frac{E_y}{E_x}\ \frac{\epsilon_I}{\epsilon_z} \tag{4-8}$$

There are two remaining terms which are still significant, both of which arise from stray (non-flipping) electric fields. Both of these rate contributions are derived from products of terms in the $E1_{ST}$ amplitude.

The individual factors in these terms can be measured independently. The stray electric field in the z-direction is

measured on the $\Delta F = 0$ transition, for which the dominant transition rate terms are

$$|A_E|^2 = \alpha^2 \, E_X^2 \, |\tilde{\epsilon}_X|^2 \left[1 + b \frac{\Delta E_X}{E_X} + b \frac{\Delta E_Z}{E_X} \frac{\epsilon_Z \cdot \epsilon_R}{|\tilde{\epsilon}_X|^2} \right] \qquad (4\text{–}9)$$

The last two terms in this rate include the factor b (± 1), which simply emphasizes that these terms will change sign when the electric field reverses. The last term is the one we use to determine ΔE_Z. If we use linear polarization at a 45° angle to the electric field, the modulation of the signal with the E reversal will include the ΔE_Z contribution; if we then rotate the polarization 45° to the other side, the sign of ϵ_R relative to ϵ_Z will reverse, and the sign of the last term will also reverse. This allows us to isolate the ΔE_Z term.

The measurements of E_y and ΔE_y use two closely related terms in the $\Delta F = \pm 1$ rate expressions:

$$|A_E|^2 = \beta^2 \, E_X^2 \, \epsilon_Z^2 \left[1 + \left(\frac{E_y}{E_X} + b \frac{\Delta E_y}{E_X} \right) \frac{B_X}{B_Z} \frac{\epsilon_I}{\epsilon_Z} + \ldots \right] \qquad (4\text{–}10)$$

These terms are easily observed if the B_X field is increased using an external coil; we have a coil that can apply a 10.5 G field in the interaction region. When we also reverse the direction of this applied field, we can isolate this term from any similar terms. Both terms in Eq.4–10 reverse with the polarization- and m-flips; the ΔE_y term also reverses with the E-flip.

The B_X field is measured using this same term, except with E_y/E_X set to a large value. The drive motor on the detector box allows us to change this field tilt quickly, so that we can set a large E_y/E_X

to measure the value of B_x/B_z. For this measurement, we want to know the B_x field without the added field used in the E_y/E_x measurement, so we turn that coil off. Note that the part of B_x that flips with B_z is the quantity we measure.

Since the ΔE values are not easily controlled, it is helpful that there is a controllable factor in each of the equations 4–7 and 4–8, so that we can get an extra degree of suppression of each systematic contribution. The B-flipping part of B_x is controlled by changing the current in the B_x shim coils at the same time that the B_z current is reversed. (The stray B_x field does not contribute to the PNC, since the rate contribution that comes from that part of B_x does not reverse at the B-flip). We adjust the B_x shim currents for each polarity of B_z so that the flipping component of the resulting field along x is zero. The value of E_y/E_x can be nulled by physically tilting the field plates (using the detector box motor) until they are parallel to the laser path.

4.5 Typical Systematic Measurements

We have studied the behavior of the systematic measurements extensively to determine the reliability of our measurements of the various fields. We need to know how long we can expect the various fields to stay reasonably close to their initial values, so that we know how often we must measure them. We also need to be certain that our measurements will accurately determine the desired quantity.

Dilution factor: Typical values for the dilution factor range from 1.02 to 1.05. Thus the PNC measurements were reduced by 2% to 5% by the overlap of adjacent lines. The variations in this dilution factor were caused by changes in the velocity distribution of the cesium atoms in the beam. Most of these changes apparently resulted from clogging of the cesium beam apertures; as the clogging begins, we commonly increase the oven temperature to try to maintain a constant transition signal. The higher oven temperature gives higher beam intensity, resulting in greater angular spread in the beam at the nozzle.

The dilution factor is measured from the scan graphs with the aid of a simple digitizing system using computer-controlled 12-bit A/D and D/A converters and the X–Y plotter. Typical spread in repeated measurements of the dilution factor from a single scan is around 0.002–0.003 (out of a typical dilution factor of 1.03). Typical variations in measurements of the dilution factor on consecutive days are around 0.008.

Stray fields: The stray electric fields in the x and z directions typically are less than 100 mV/cm. A normal value for ΔE_y is less than 50 mV/cm. If the measurements yield values much larger than this, we halt the experiment until we can reduce these stray fields. The maximum acceptable value for these and other fields depends on how well we can control the other fields that contribute to the same PNC systematic term. So, for example, since we can normally reduce E_y/E_x to less than 10^{-4}, we can tolerate a ΔE_z field as high as

100 mV/cm before the term proportional to $(E_y/E_x)\cdot\Delta E_z$ becomes substantial at the level of 1% of the PNC term.

It has been our experience that stray electric fields often decrease in size during a data run covering several days, but it is unusual for the stray field to reverse in sign. We can attribute this to a gradual washing-out of local collections of stray charge as a cesium film is slowly deposited on the surfaces of the field plates, or as oil or other volatile films are pumped away. It is rare that we can make more than one such data run before we have to open the chamber to fix some new problem.

Field misalignments: The quantity Bx/B_z can be measured with a sensitivity of about 1×10^{-4} in a reasonable measurement time (10 minutes). We measure it using the rate term proportional to E_y/E_x in Eq.4–10. We increase E_y/E_x by tilting the detector box and field plates. This sensitivity is relatively poor compared to other measured quantities; the main limitation is in how large we can make E_y/E_x without blocking the cesium beam or laser beam with the field plates.

We can measure and null out E_y/E_x with a sensitivity of about 5×10^{-6}, but these measurements drift from one day to the next. It is not uncommon to measure E_y/E_x repeatably on one day and find it has drifted by 3×10^{-5} the next day. Since this is an extremely small angle, a possible explanation is that the mirror mounts move slightly, moving the laser path relative to the field plates. We have seen much larger mirror movements than this in pumping out the chamber; we found that the PBC mirror mounts were buckling as the

mirror temperature control system readjusted to the sudden removal of the convective heat load. Similarly, the mirrors might move by a small angle if the radiative heat load changed slightly.

Typical values of the systematic correction from the term in Eq.4–10 are less than ±0.010 mV/cm out of a PNC value near 1.6 mV/cm. The correction for the term in Eq.4–8 is usually less than ±0.005 mV/cm.

Non-uniformities: We have also performed a simple test to check for large non-uniformities in the fields that cause these systematics. We took our usual systematic measurements, measuring these quantities averaged over the whole interaction region; then we took measurements with half of the cesium beam blocked. In this way we could compare the average over the entire interaction region with the average over just one half of it.

It is important to know this information, because the size of a systematic contribution averaged over the interaction region is the average of the product of two quantities (e.g. ΔE_y and B_x/B), whereas we can only measure the average value of each factor over the entire interaction region. Non-uniformities in each factor could cause much larger or smaller systematic contributions than our systematic measurements would predict.

Our measurements showed a discrepancy of less than 1.3×10^{-4} in the B_x/B field misalignment, less than 6×10^{-5} in the E_y/E_x field misalignment, and less than 40% for the stray fields. This implies that the extra non-statistical uncertainty in the PNC result is less than 0.001 mV/cm due to these non-uniformities.

PBC mirror birefringence: We have made several measurements of the birefringence of the output mirror of the PBC throughout the experiment. With the Litton output mirror, we have seen birefringence much smaller than we can measure reliably. Typical measurements gave $\varphi \cdot \sin 2\theta$ less than 4×10^{-6} at first. Later, after nearly two years of use at high intensity (and often with a film of cesium), the measurements began to show values around 1.5×10^{-5}. After rotating the mirror and moving the laser spot to a different place on the mirror, we were again able to reduce it to less than 4×10^{-6}.

New E1·M1 Systematic Term: Typical values for the $\Delta m = 0$ part of the fractional $\Delta E \Delta B \Delta m$ are less than 10^{-3}, with less than 10% uncertainty; typical average $\Delta\epsilon_x^2/\epsilon_x^2$ measurements are less than 2×10^{-4}, with uncertainty around 1×10^{-4}. The usual correction to the PNC for each day of data was on the order of ±0.001 mV/cm or less. The final corrections to the PNC (averaged over the entire data set) were +0.0007(5) mV/cm on the F=4 → F'=3 line and -.0036(6) mV/cm on the F=3 → F'=4 line.

4.6 Tests of the Apparatus

We have also performed extensive testing of the computer, the data-taking program, and the analog electronics to ensure that there are no systematic errors. At the most basic level, a systematic error in these systems would not lead to a PNC systematic in the long run, since the data taken on the low-frequency end of the Zeeman

multiplet is always subtracted from the data taken on the high-frequency end; a systematic error that affects all of the data files equally will cancel. However, of greater concern is an error that exists only for part of the data-taking time, or is sensitive to the presence of another modulation signal (which may have a different value on each end of the Zeeman multiplet).

The simplest problem that may occur in the computer is an error in the timing of the gated integrator. Since the integrator's final output value is proportional to the length of the integration period, any error in the timing of the start or end of this integration period will give an erroneous reading of the input voltage. The integrator output is also proportional to the average DC offset at its input; therefore timing errors lead to the greatest measurement errors when the offset is large at the input of the gated integrator.

Ordinary timing jitter does not present a problem unless it limits the noise on the measurements; however, mistakes that repeat in some pattern may cause shifts in the PNC result. Recall that the timing of the integrator gate period is controlled by the computer; if the program were designed poorly, it could easily produce timing errors that correlate with one or more of the field variables. Luckily, timing errors are very simple to detect; if the results of measurements taken with zero DC offset at the input of the integrator differ from those taken with a large DC offset, the timing errors are substantial.

Another problem is more subtle and more difficult to detect with certainty, although it is easy to correct. It is the "carving" of data by the A/D converter. We can think of the A/D converter as

measuring the voltage with high precision and then separating these numbers into much wider bins. If the noise at the input of the A/D converter is comparable to or less than the resolution of the converter (the width of a bin), the numbers acquired can be greatly affected by small changes in the offset of the input signal. For example, we can imagine a signal so quiet and steady that it can consistently supply a voltage that is one-tenth of a bin width below the edge of a bin; the A/D converter will consistently read the same bin. If we change the offset by one-fifth of a bin width, the A/D will begin reading the next higher bin consistently. Thus the small offset results in a shift of the measurements that is five times larger. The fundamental problem is that so-called bit noise (digitizing error) is non-statistical noise.

We performed extensive tests of this effect using an electronic circuit to produce signals similar to the PNC data. When the noise is small enough to allow carving to occur, the first effect we can see in the test data is a rapid rise in the χ^2 for the distribution of data. We found that this begins at a noise level that is about a factor of two lower than the noise in our typical PNC data. Although this seems disturbingly close, we found no evidence that our PNC data was being carved. One way to check this is to see if normal fluctuations in the data are large enough to spread the measurements over several bins (this is the case in our PNC data). Another way to check it is to see if the χ^2 test improves when the signal (and its noise) are amplified further before the input to the A/D converter; since the distribution of our PNC data already looks statistical, we have not tried this approach. The way to fix the problem is to

amplify the signal more; this prevents the bit error from dominating the noise in the measurements, but does not sacrifice the signal-to-noise ratio.

Another problem that occurred with an earlier detector was an AC coupling effect, in which the AC current from the detector was much more efficiently coupled to the amplifier than the DC current. As a result, the modulation signals we measured were a much larger fraction of the DC signal, and all of our results were too large. This effect is also easy to detect. We commonly monitor our detector collection efficiency using an LED with a square-wave-modulated current. The rising and falling edges of the detector signal normally have a rounded exponential-charging shape due to the limited detector amplifier bandwidth. However, if the detector exhibits this AC coupling, the signal overshoots at each edge. We have seen no such behavior with the present detector.

We have also checked that the detector quantum efficiency is not affected by the direction of the applied electric or magnetic fields. We tested this by monitoring a steady signal produced by the same LED while we reversed the electric and magnetic fields. We place an upper limit of 10^{-5} on the fractional modulation of the collection efficiency; since the polarization and m_F flips can suppress this still further, any residual effect is unimportant.

4.7 Noise Characteristics

The main classes of transition noise under the conditions chosen for PNC data are detector/amplifier noise, transition locking noise,

and spurious scattered light noise. The detector/amplifier noise originates in such things as Johnson noise, amplifier input noise currents and voltages, and cosmic ray and radioactivity events. The transition locking noise comes from limitations in the various servo systems that stabilize the laser frequency and intensity and in the optics that provide the feedback signal for stabilization. The scattered light noise comes from scattering of the green laser light by Cs_2 molecules and by the field plates.

One important contribution to the detector noise (in the absence of light input) at the sampling frequency we used in virtually all of our data acquisition is the noise from occasional current spikes from the detector. The spikes range in size up to 1.5 pA; they occur at an average rate of about 6–10 per minute. We see these spikes no matter what conversion gain we use in the detector amplifier, and they disappear when we substitute a dummy detector (a resistor-capacitor combination). The effective noise current produced by these spikes is around 4.6 $fA/\sqrt{Hz}$. The noise we observe during the intervals in which no current spikes occur is around 2.5 $fA/\sqrt{Hz}$.

We find that the spikes are much more frequent when we place a 1 mm thick RG–780 infrared filter directly over the detector; these spikes return to their previous frequency when we place an ordinary 1 mm glass slide between the RG–780 filter and the detector. We interpret the added spikes as current pulses excited by radioactive emission from the filter glass. We can reasonably surmise that most of the remaining spikes also result from particle detection by our low-noise silicon detector. We have seen similar spikes on small germanium detectors we have tested, and we were able to reduce the

frequency of these events sharply by shielding the device with lead bricks. It is possible that the particles originate either in cosmic rays or in radioactive materials nearby.

The other important contributions to the noise on the detector signal are[55]

(1) the Johnson noise from the detector shunt resistance R_D

(2) the Johnson noise from the feedback resistor R_F

(3) the amplifier equivalent input noise voltage e_{na}

(4) the amplifier equivalent input noise current i_{na}

(5) the shot noise of the input signal.

The shot noise on a signal current I is $\sqrt{eI}$, where e is the electron charge; for a signal of 2×10^{-10} A, this current noise is about 6 fA/$\sqrt{\text{Hz}}$. Shot noise represents a fundamental noise limit; we seek to reduce all of the other noise sources to below this value.

The Johnson noise produced by a resistance R is

$$i_{nJ} = \left(\frac{4k_B T}{R}\right)^{1/2} \qquad (4\text{–}11)$$

When the detector is cooled by the LN_2 system to its final temperature (somewhere below about −180°C), its shunt resistance reaches about 10^9 Ω. The Johnson noise associated with this resistance at this low temperature is about 1 fA/$\sqrt{\text{Hz}}$. The Johnson noise of the 10^{10} Ω feedback resistor is about 0.6 fA/$\sqrt{\text{Hz}}$.

The amplifier equivalent noise input voltage produces a noise current signal

$$i_n = \frac{e_{na}}{Z_S} = \frac{e_{na}}{R_D}\sqrt{1 + (\omega R_D C_D)^2} \qquad (4\text{-}12)$$

where Z_S is the source impedance (in this case, the combination of the detector shunt resistance R_D and shunt capacitance C_D). At frequencies below about 15 Hz, this noise is less than the detector Johnson noise; however, above about 20 Hz the noise begins to scale as $e_{na}\omega C_D$, becoming much larger than the other noise sources. Thus we must operate at a low enough sampling frequency to keep this noise source from dominating. At our sampling frequency of 5 Hz, the noise contribution is about 2 $fA/\sqrt{Hz}$; the figure quoted for i_{na} is about 3 $fA/\sqrt{Hz}$. Combined in quadrature, these noise sources total about 3.5 $fA/\sqrt{Hz}$, which is slightly more than the observed value in the absence of the current spikes on the detector; this is still much less than the observed noise in the presence of current spikes.

In choosing the signal size (i.e. the electric field) to optimize the parity violating signal-to-noise ratio, we must separate the various types of noise according to how they scale with the applied electric field. Detector noise and scattered light noise are independent of the applied field. Shot noise is proportional to the square root of the signal current, and is therefore linear in the applied field. Transition locking noise sources, which come from residual noise in the stabilization of the laser frequency and intensity, are nominally a constant fraction of the signal, and are thus proportional to the square of the electric field. The PNC

modulation is linear in the applied field. Then the PNC signal-to-noise ratio is

$$\frac{\text{PNC}}{\text{noise}} = \frac{aE}{\sqrt{b^2 + c^2E^2 + d^2E^4}} \qquad (4\text{–}13)$$

where a, b, c, and d are experimentally determined constants. This ratio is maximized for $b = dE^2$, independent of a and c. Thus we optimize the value of electric field by setting the noise from transition locking equal to the total electric-field independent noise contribution. In practice, this ratio is fairly insensitive to changes in E near the optimum.

An interesting side issue is how to choose the optimum combination of electric field and polarization. Increasing the ratio $|\tilde{\epsilon}_x/\epsilon_z|$ by a factor ξ (without changing the relative 90° phase shift) decreases the PNC rate term by the factor ξ and the parity-conserving signal size by the factor ξ^2. Thus the fractional PNC modulation is increased by the factor ξ. We can boost the electric field to maintain the optimum noise condition. However, a systematic contribution prevents us from doing so: the PNC scales with ξ, but the new M1 systematic (Section 4.3) scales with ξ^2. Thus the ratio of the PNC to this PNC systematic contribution worsens. We chose $|\tilde{\epsilon}_x/\epsilon_z| = 1$ as a compromise.

The scattered light signal that comes from scattering off the electric field plates is usually about 10 pA, with a noise contribution that is much smaller than the detector noise. The scattered light contribution that depends on the presence of a cesium

beam (from molecular scattering) is about 4 pA, with a very small noise contribution.

Common sources of transition locking noise include improper setting of the frequency and intensity locks (introducing electrical noise or decreasing the available feedback gain) and poor optical design (introducing noise in the measurement of intensity or frequency). We have improved the apparatus in both ways since our earlier measurement. Our new frequency locking system involves stabilizing the frequency of the laser to a very narrow PBC resonance. Essentially all of the remaining frequency fluctuations are due to motion of the PBC mirrors, which occurs on a very slow time scale ($\lesssim$100 Hz). These fluctuations are much easier to control than the fast dye laser fluctuations we faced in our earlier measurement.

The optical noise introduced by vibrations of the intensity-monitoring photodiode at the output of the PBC was also vastly reduced. The photodiode was mounted in a very flimsy way during our first measurement; we found great improvement (about a factor of two) in mounting this photodiode on a very rigid mount and adjusting its position to find a place where the signal was insensitive to small adjustments.

Typical transition locking noise at high transition rates (on the $\Delta F = 0$ transition peak) was about $2.2 \times 10^{-5}/\sqrt{\text{Hz}}$ as a fraction of the transition rate. This is more than a factor of two lower than in our previous measurement. This fractional noise implies a typical transition locking noise contribution on a 2×10^{-10} signal of about 4.4 $\text{fA}/\sqrt{\text{Hz}}$.

Under PNC experimental conditions, the typical noise contributions from the various sources were

(1) Detector/amplifier noise sources 4.6 fA/$\sqrt{\text{Hz}}$

(2) Transition locking noise 4.4 fA/$\sqrt{\text{Hz}}$

(3) Shot noise 5.7 fA/$\sqrt{\text{Hz}}$

(4) Scattered light noise < 3 fA/$\sqrt{\text{Hz}}$

The quadrature sum of these noise amplitudes is 8.5 fA/$\sqrt{\text{Hz}}$. This matches the observed transition noise ($\gtrsim$8.4 fA/$\sqrt{\text{Hz}}$).

The PNC term under typical conditions contributes a fractional modulation of about 3.2×10^{-6}, which gives a PNC detector current signal around 0.64 fA. Thus the PNC signal-to-noise ratio is about 0.071 in one second, implying an integration time of about 3.3 minutes for a 100% measurement of the PNC. The final precision of 2.1% in this PNC measurement was achieved in approximately 160 hours of integration time. This gives the slightly larger value of 4.2 minutes for the 100% integration time. In either case, we have an integration time that is a full order of magnitude lower than in our first PNC measurement, and at least another factor of three lower than in any other PNC measurement yet performed.

4.8 Summary

Many of the systematic terms we were concerned with in this experiment are the same ones that we worked with on our previous PNC measurement. The notable exception is the so-called new M1 systematic, which turned out to have a significant effect in our early attempts at this second measurement. The discovery of this

contribution will also enable more accurate measurements of the M1 transition amplitude in the future.

We have also improved the suppression of the systematic terms in Eqs.4–7 and 4–8 by using a drive motor to allow large changes of E_y/E_x while the system is under vacuum; this allows us to measure B_x/B carefully at a large value of E_y/E_x and then set E_y/E_x to near zero. And we have improved the technique for measuring the output mirror birefringence, which gives rise to the well-understood "old" M1 systematic. As precision improves in PNC measurements, it will be more and more important to know the contribution from this systematic accurately.

We have also increased the signal size using higher laser fields in the PBC, and decreased several noise sources; this gave about a factor of 10 decrease in the integration time required for a 100% measurement of the PNC.

CHAPTER V

RESULTS AND CONCLUSIONS

In this chapter I will present the results of our measurements and the various statistical tests we performed on the data. First I will explain the procedure for analyzing the data and applying the corrections. Then I will present the results of our measurements. Then I will discuss the many tests we performed on our data to check its statistical consistency. Then I will conclude by discussing the implications of our measurement.

5.1 Analysis Procedure

In the data-taking process, the computer operates the control lines that handle the flipping of the relays in the experiment and digitizes the transition signal, storing the results on floppy disks. This data is analyzed later to determine the fractional modulation of the signal under various reversals of the fields. The PNC signal is derived from one of these fractional-modulation results.

The data stored on the disk is simply a series of measurements of the average transition signal. Because of the electronics that precede the A/D conversion, these measurements are actually just measurements of small increments added to a fixed offset. By calculating the average of the measurements during one half-cycle of

the flipping of one of the fields and subtracting it from the average over the next half-cycle, we can measure the part of the signal that modulates with that field variable. If we average over several complete cycles of all of the field variables, we can extract the part that flips only with that one variable.

Similarly, we can measure the piece of the signal that flips with each of two or more field variables. Since there are three variables that flip repeatedly during a data file, each file contains measurements of 7 signal components that flip with one or more field variables. We denote these quantities by their flipping variables: $\Delta P \Delta E \Delta B$, $\Delta P \Delta E$, $\Delta P \Delta B$, $\Delta E \Delta B$, ΔP, ΔE, and ΔB.

Since we do not know the absolute size of the transition rate (due to uncertainties in collection efficiency, atomic beam intensity, and laser intensity), it is more useful to know the fractional modulation rather than the absolute size of the modulation. For this reason we scale all of our results by the full size of the average signal as measured with a voltmeter. To ensure accurate scaling of the digitized modulation results, we have carefully calibrated the A/D converter and the amplifiers preceding it using the same voltmeter as a reference.

Our final result is quoted as the ratio of the PNC rate term to the dominant Stark-induced rate term. The $1/E_x$ dependence of this ratio is eliminated from the results by multiplying the fractional PNC modulation by the measured size of the electric field. We then apply systematic corrections calculated from our preliminary systematic measurements. We have taken measurements in which the systematic corrections were deliberately made large, in order to

determine the proper sign for applying these corrections. Our small calculated corrections are added to and subtracted from the PNC in the same way.

5.2 Final Result

Our new measurement of PNC in atomic cesium gives

$$\frac{\mathrm{Im}(E1_{PNC})}{\beta} = \begin{cases} -1.639(47)\ \mathrm{mV/cm} & F=4 \rightarrow F'=3 \\ -1.513(49)\ \mathrm{mV/cm} & F=3 \rightarrow F'=4 \\ -1.576(34)\ \mathrm{mV/cm} & \text{average} \end{cases} \qquad (5\text{-}1)$$

where the uncertainties include all sources of error.

This value is in good agreement with our earlier measurement of −1.65(13) mV/cm for the average of the results on the F = 4 → 3 and F = 3 → 4 transitions, and with the value −1.56(17)(12) mV/cm reported by Bouchiat *et al.*[31] (the first uncertainty is statistical and the second is systematic). They have since given a revised value of −1.52(18) mV/cm after a re-analysis of their data.[32]

Using the value $\alpha = -269.2(2.8)\ a_0^3$ from Ref.43 and $\alpha/\beta = -9.9(1)$ from Refs.44-46, we calculate $\beta = 27.2(4)\ a_0^3$; this gives

$$\mathrm{Im}(E1_{PNC}) = -0.834(22) \times 10^{-11}\ ea_0 \qquad (5\text{-}2)$$

(this experiment)

To relate this to the weak charge Q_W (or equivalently $\sin^2\theta_W$), we must first know the value of the matrix element in Eq.1-10. As we mentioned in that chapter, this matrix element cannot be measured

directly, but it can be calculated using theoretically derived wavefunctions. There is still some uncertainty in the calculation of this matrix element, but we believe that the best value to use is $E1_{PNC} = 0.95(5) \times 10^{-11}\ ieа_0(-Q_W/N)$ reported Johnson *et al.*[41] Using this value with our measurement we find

$$Q_W = -68.5 \pm 1.8 \pm 3.4 \qquad (5\text{–}3)$$

(this experiment)

where the first uncertainty is our experimental uncertainty and the second is the theoretical uncertainty. This is in good agreement with the standard model value using $\sin^2\theta_W$ obtained from the mass of the W boson[6] in Eq.1–5:

$$Q_W = -71.8 \pm 1.1 \qquad (5\text{–}4)$$

(standard model prediction)

The experimental value of Q_W can instead be used to derive a value for the weak mixing angle θ_W. Using Eq.1–5, we find

$$\sin^2\theta_W = 0.214 \pm 0.008 \pm 0.016 \qquad (5\text{–}5)$$

(this experiment)

where the two uncertainties are experimental and theoretical. This value is in good agreement with the value of 0.230 ± 0.005 obtained from the mass of the W boson.[6]

The difference in the PNC measurements on the two hyperfine lines contains information on the contributions from the proton-spin dependent PNC term (Eq.1–1, second term) and the anapole moment of the nucleus (a nuclear PNC effect arising from charged weak current

interactions). Novikov *et al*[56] have calculated the difference in the PNC for these two hyperfine lines using a simple shell model for the nucleus and ignoring the anapole moment contribution. They find the difference is equal to that from the flip of one proton spin, with an uncertainty of 30%. However, recent calculations indicate that the effect of the anapole moment is about five times larger.[57]

The difference in our PNC measurements on the two hyperfine lines has the opposite sign from our earlier measurement. The earlier difference was +0.29(26) mV/cm, whereas the present value is −0.126(68) mV/cm; the discrepancy is 0.42(27) mV/cm, or 1.5 standard deviations. Since the new E1·M1 systematic term (which can strongly affect the difference) may have contributed significantly in that measurement, we are not concerned by this discrepancy.

Frantsuzov and Khriplovich[57] calculate that the relationship between this PNC measurement difference and their nuclear asymmetry parameter κ_a is

$$\frac{E1^{4\to3}_{PNC} - E1^{3\to4}_{PNC}}{E1^{4\to3}_{PNC} + E1^{3\to4}_{PNC}} = 0.0555\ \kappa_a \qquad (5\text{–}6)$$

Novikov *et al.*, neglecting the nuclear anapole moment and using the simple shell model of the nucleus, asserted that $\kappa_a = C_{2P}$ to within 30%.[56] Our value $\kappa_a = +0.72(39)$ is in poor agreement with the standard-model prediction $C_{2P} = +0.047$. However, Frantsuzov and Khriplovich[57] calculate that the anapole moment is in the range +0.25 to +0.33; the sum of the two contributions gives a value for κ_a between +0.30 and +0.38. Our measurements agree well with this prediction.

Thus our results show preliminary evidence of the presence of nuclear-spin dependent PNC effects. The best agreement is with the prediction of a nuclear anapole moment arising from charged weak current effects in the electron-nucleon interaction.

5.3 Statistical Tests

We have performed many different statistical tests of the data to make sure that the measurements are consistent, and as an additional check for systematic problems. We have checked the statistical distribution of measurements of many different quantities in the data, at time scales ranging from seconds to the entire five-month duration of the data taking. In none of the tests did we find evidence of unexplained non-statistical behavior.

We used the χ^2 test in many different cases to check the data for any non-statistical spread at any time scale. In each case we broke the data into "chunks" of various sizes and calculated the average and statistical uncertainty for each chunk ; then we examined the data sets composed of these averages and uncertainties to look for evidence that some chunks of data differed from the others to a statistically significant degree. In all cases, we found that the fluctuations within a data set were statistical.

We checked measurements of $\Delta P \Delta E$ on each B-flip half-cycle (27 seconds) within a given data file (22 minutes long); $\Delta P \Delta E \Delta B$ measurements from each full B-flip cycle within a file; $\Delta P \Delta E \Delta B$ averages from entire data files on a particular hyperfine line from a single day of data; the same $\Delta P \Delta E \Delta B$ values for all of the data taken

in the entire PNC measurement; and the averages of $\Delta P \Delta E \Delta B \Delta m$ for each hyperfine line on each day for the entire PNC measurement.

Our criterion for evaluating the goodness of a particular distribution involves the calculation of $P(\chi^2,\nu)$ – the probability of randomly selecting a distribution with a higher value of χ^2. An exceedingly low value of $P(\chi^2,\nu)$ implies an exceedingly low probability that the distribution is statistically distributed. For the case $\chi^2/\nu \approx 1$, $P(\chi^2,\nu)$ is near 0.5; this implies that the median distribution has rms statistical fluctuations of about one standard deviation.

The calculated value of $P(\chi^2,\nu)$ for the distribution of $\Delta P \Delta E \Delta B$ measurements on each of the four transition lines ($\Delta F = \pm 1$, high- and low-frequency peaks of the Zeeman spectrum) on any given day ranged from 1% to 95%. We were initially uneasy about the occasional low probabilities; however we have concluded that these are statistical fluctuations whose effects are amplified in the small sets of data. Our position is supported by the following tests.

We tabulated the $\Delta P \Delta E \Delta B$ results for all of the files in the full five-month PNC measurement run, dividing them into four sets as above. We found $P(\chi^2,\nu)$ values of 0.38, 0.25, 0.007, and 0.91; the lowest probability was for the set of measurements on the $F=3 \rightarrow F'=4$ low-frequency peak (although even this probability is not beyond reason). But in this test we had not included any systematic corrections to the file results before collecting them as a data set. Later, when we looked at the distribution of daily measurements of the PNC (proportional to $\Delta P \Delta E \Delta B \Delta m$ – the difference between the low- and high-frequency results) after applying the systematic

corrections, we found $P(\chi^2,\nu)$ very close to 50% for the two data sets from the two hyperfine lines. The set of daily averages of the PNC measurements on the two hyperfine lines also showed $P(\chi^2,\nu)$ near 50%. These results indicate that the distribution of corrected daily measurements of the PNC term is statistical.

In addition, in the set of uncorrected $\Delta P \Delta E \Delta B$ results we checked the distribution of the deviations from the group average. We found that the number of files that fell more than 2.2, 2.5, 2.7, or 3.0 standard deviations from the mean matched the predicted statistical distribution quite closely. This disproved our intuitive sense that those far-flying files were "bad" in some way. Thus we conclude that the distribution of file results is chiefly due to statistical fluctuations, with some known systematic corrections.

We also repeatedly checked the data to be sure that the final uncertainties calculated in the analysis of each file were consistent with the short-term spread observed in the data. That is, we made sure that the uncertainty given with the $\Delta P \Delta E \Delta B$ result was comparable to the value we would calculate from observing the standard deviation of ΔP measurements in a short time (like one B-flip half-cycle). We never found any deviations from the simple scaling we expected. This shows that the $\Delta P \Delta E$ measurements were not drifting or changing suddenly in the middle of a file.

5.4 Drifts and Shifts

We also analyzed our data carefully to make sure there were no false PNC signals arising from long, slow drifts or large step-

changes in the modulating signals. We looked at the individual signal measurements and their averages to look for drifts that would cause ΔP offsets or false $\Delta P \Delta E$ contributions. Our simplest method was to plot the measurements with their statistical uncertainties as a set of lines on the page; we then scanned them by eye to look for patterns. If we found an apparent pattern, we would then subject the data to the statistical tests described above, to see if it could be purely statistical in origin.

We checked $\Delta P \Delta E$ measurements from each half-cycle of the B-flip and $\Delta P \Delta E \Delta B$ measurements from successive full cycles of the B-flip. We also compared these pictures for successive data files to look for patterns stretching across file boundaries. We found no such drifts or step changes that fell outside the realm of normal statistical fluctuations. This surprised us, since we saw many sections in which there appeared to be a clear pattern; our lesson is that the eye is much better at finding non-statistical patterns than our experiment is at producing them.

5.5 Conclusions

We have completed a measurement of PNC in atomic cesium with an uncertainty near 2%. The excellent agreement between our measurement and the prediction of the standard model of electroweak interactions is another valuable corroboration of this theory. It also has implications for theories that go beyond the standard model; it places new limits on the masses of additional bosons and the sizes of coupling constants in superstring theories, supersymmetric theories,

and others.[58,59] Fig.5–1 shows the present experimental constraints on the model-independent electron-quark coupling constants C_{1u} and C_{1d}.[58] If the electroweak theory were exactly correct, the values of these coupling constants would fall on the line marked $SU_2 \times U_1$; the position along this line would be determined by the value of $\sin^2\theta_W$. Deviations from this line are predicted in various grand unified theories (GUTs), as shown by the arrows marked Z_η (superstring), Z_χ (SO_{10}), and Z_{LR} (left-right symmetric). These extra neutral gauge bosons are predicted to shift the values of C_{1u} and C_{1d} by an amount that is inversely related to their mass. The figure shows that atomic PNC results are not very sensitive to the value of $\sin^2\theta_W$, but they are uniquely sensitive to deviations from the $SU_2 \times U_1$ line.

Fig.5–2 shows the lower mass limits our experiment places on the neutral Z_η gauge boson predicted in the E_6 class of grand unified theories.[59] In this plot, the position $\phi = 0$ corresponds to the SO_{10} model, and $\phi = -52.2°$ corresponds to a popular superstring model. For the SO_{10} model, our experimental results indicate that $M_{Z_\chi} >$ 515 GeV with 68% confidence, and $M_{Z_\chi} >$ 315 GeV with 90% confidence. Similarly for $\phi = -52.2°$ (superstring), $M_{Z_\eta} >$ 125 GeV with 68% confidence, and $M_{Z_\eta} >$ 105 GeV with 90% confidence. These energies are already a challenge to the largest accelerators available. Extending these limits is one of the goals of further improvement of PNC measurements and calculations.

Improvements on this technique are now being developed. Two methods are being considered for increasing the transition signal detected, under the present limitations of cesium density and laser

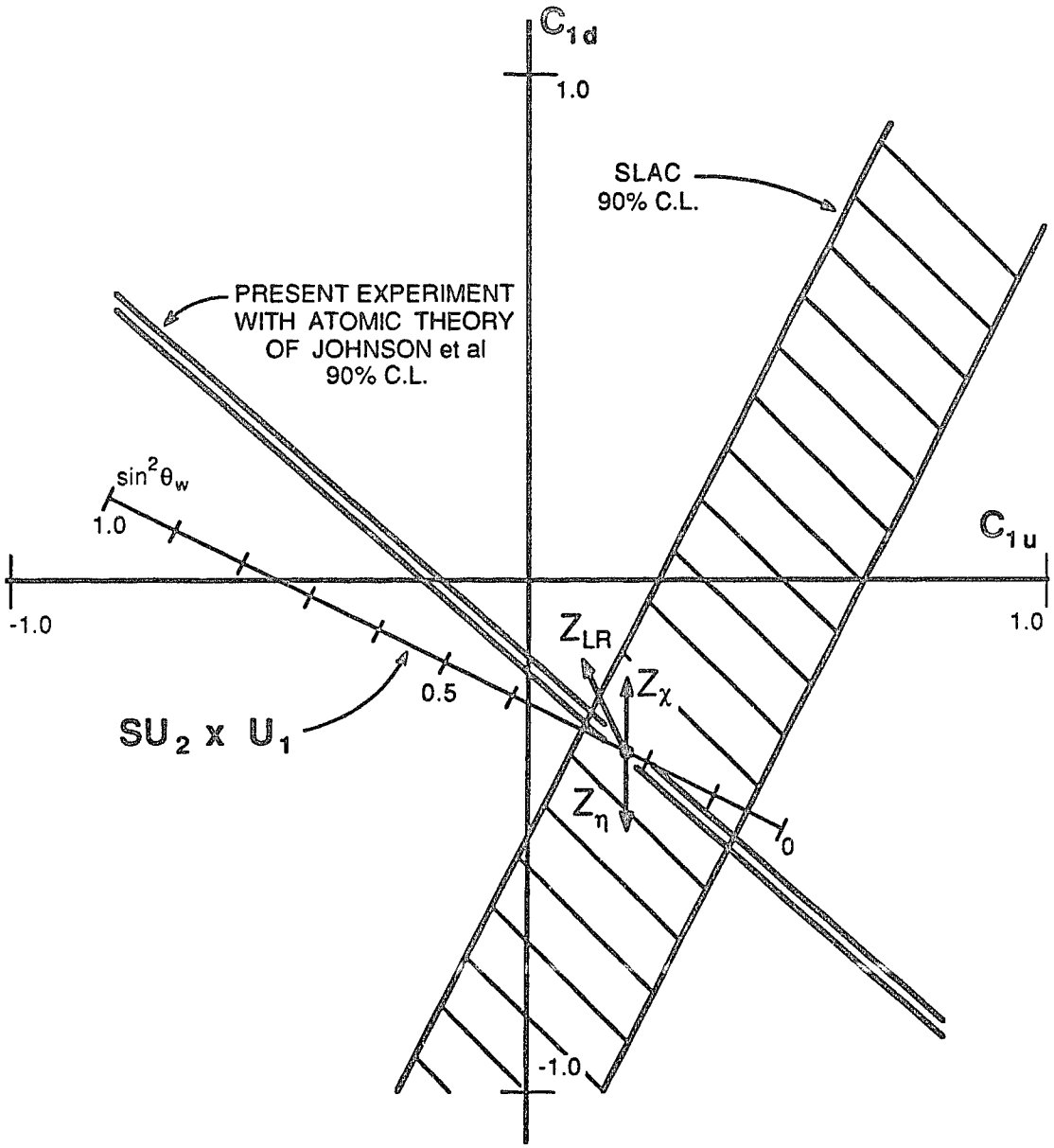

Fig.5-1. Experimental limits on the model-independent e-q coupling constants C_{1u} and C_{1d}. Also shown are deviations from the $SU_2 \times U_1$ predictions due to gauge bosons predicted in various grand unified theories (GUTs).

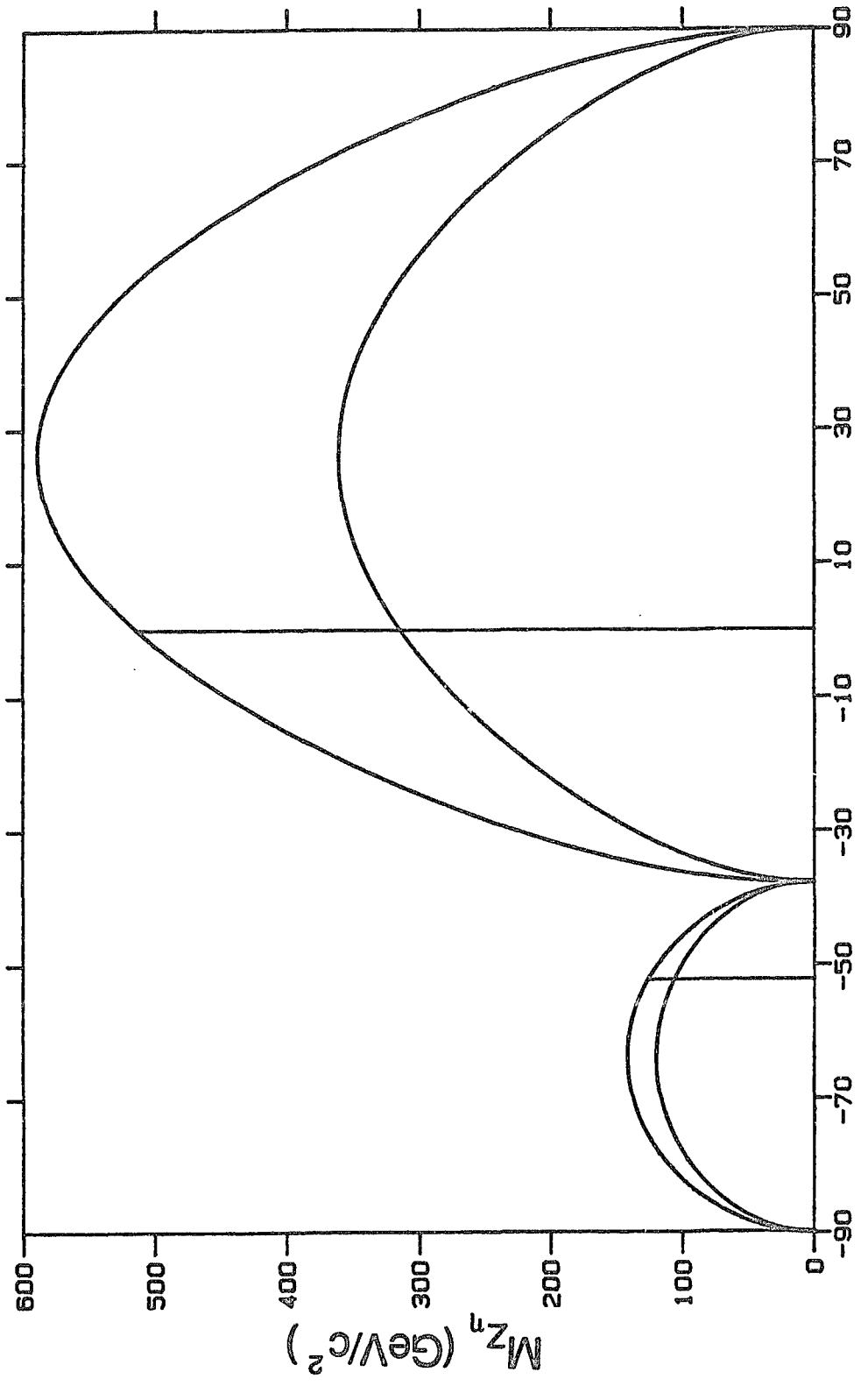

Fig.5-2. Lower limits on the mass of the Z_η boson in E_6 GUTs, derived from our results. ϕ is a theoretical mixing angle. Upper curve: 68% confidence. Lower curve: 90% confidence.

intensity. Such an increase would allow the use of a lower static electric field, thus increasing the fractional PNC modulation.

In one system, the cesium atoms in the beam will be optically pumped into a single spin state before the interaction region; this will take advantage of atoms in the beam that now are unused. In the ground state of cesium there are a total of 16 equally-populated spin states in the two hyperfine levels; our experiment only uses one of those spin states at a time. If all of the atoms in the beam start in a single initial state, we have 16 times as much signal for a given single-atom transition rate. Also, since the initial spin state is selected by optical pumping, we do not need to select it by the Zeeman splitting that we now use. Thus we can use a magnetic field of only a few Gauss (enough to orient the atoms perpendicular to the laser and the static electric field). This reduction of the magnetic field will essentially eliminate the Zeeman mixing of hyperfine states that now contributes to many of our systematic problems, including the new M1 term.

Another variation of this method holds the possibility of a much greater increase in signal. If the atoms are very highly polarized before entering the interaction region, the atoms that undergo the 6S→7S transition will be greatly depolarized. If we probe these atoms downstream, we can in principle collect hundreds of scattered probe photons from each depolarized atom (through suitable choice of the probe polarization and wavelength). There are obvious difficulties with getting high extinction of the probe scattering when the 6S→7S rate is zero, but the enormous increase in the signal size is clearly helpful. An additional benefit of using downstream

detection is that we no longer need to collect photons for a transition signal while the atoms are still in the interaction region; this means that we may choose to use opaque field plates whose stray field properties and durability are much better than the transparent ones we now use.

CHAPTER VI

ASYMMETRIC LINE SHAPE

An isolated atom which is weakly excited in a standing wave field is one of the most basic systems one can study in spectroscopy. It has been commonly assumed that this simple case would have a symmetric, easily understood line shape. We have observed that this is not the case, and in fact very weak transitions in a strong standing wave field can show striking asymmetric distortions of the resonance line shape. This is significant because these are the conditions encountered in the precision measurement of parity nonconservation in cesium, and this measurement relies on a thorough understanding of the resonance line shape. Also this is relevant to precision wavelength standards for which weak transitions have been sought because of their narrow linewidths.

6.1 Observations

We find the intensity-dependent distortion has two rather interesting and surprising characteristics. First, the frequency dependence is characterized by the natural linewidth, and, although the distortion depends on the laser intensity, it is independent of the excitation rate. Thus we have the unusual situation that on a Doppler-broadened single-photon resonance line there is a distinct

Doppler-free structure for arbitrarily small excitation rates. Second, the frequency dependence of the distortion for electric dipole (E1) transitions is the mirror image of that for magnetic dipole (M1) transitions. We have studied this distortion of the line shape for a variety of experimental conditions, and find our results agree very well with the line shape we calculate using optical Bloch equations that include the spatially varying ac Stark effect.

Prentiss and Ezekiel[60] have previously studied the intensity dependence of the line shape of the sodium D line. They observed an asymmetry at moderate to high excitation rates which they explained in terms of the induced dipole force changing the atomic trajectories. However, the asymmetry we observe is different in that it is independent of the excitation rate. To our knowledge this is the first observation of this type of line shape distortion.

In Fig.6-1a we show the line shape observed at relatively low intracavity power. The width is determined by the residual Doppler broadening. In Fig.6-1b we show a high-power line shape and in Fig.6-1c we show the difference that is obtained by scaling the curve in 6-1a by the laser power ratio and subtracting it from the curve in 6-1b. There is no absolute frequency scale, so the origins of the two frequency scales were chosen to superimpose the undistorted wings of the lines. At moderate power (less than 100 W) the difference curve passes through zero at essentially the undistorted line center, and the width, taken to be the separation between the positive and negative peaks, is always 3.5(5) MHz. This matches the 3.3 MHz natural linewidth of the 7S state. As the power is increased above 100 W the curve broadens and shifts slightly, as can be seen in

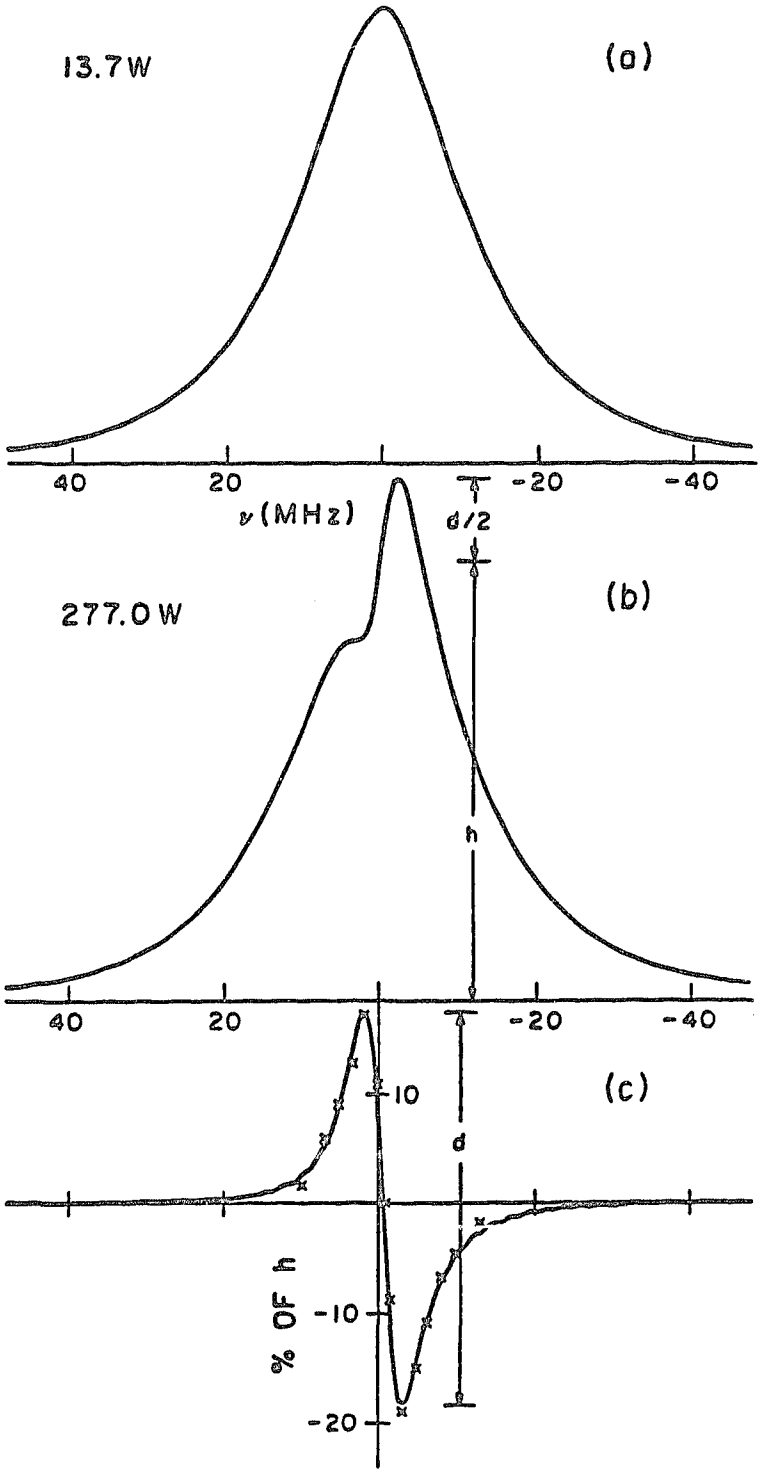

Fig.6-1. (a) Line shape of E1 transition excited by a standing wave with 13.7 W in each traveling wave. (b) Same transition with 277 W per traveling wave and different vertical scale. (c) solid curve is the difference between curves (a) and (b) after scaling by power. Theoretical points marked by ×.

Fig.6–1c. For the highest power we used (350 W), a width of 5 MHz and a shift of about 0.5 MHz were observed. This power corresponds to a peak intensity of 3.5×10^5 W/cm^2 at the center of the Gaussian wavefronts of each of the traveling waves in the cavity.

In Fig.6–2 we show the dependence of the distortion on the laser power. We are characterizing the asymmetry in terms of the fractional distortion, D, which we define as the ratio of the size of the distortion (d) to the peak height (h) the line would have if there were no distortion. This value initially rises linearly, but at higher power it begins to saturate.

We have also found that the asymmetry can be affected another way. When the angle between the cesium beam and the atomic beam differs from perpendicular by a value greater than the divergence of the cesium beam, the line shape begins to split into a doublet corresponding to excitation by each of the Doppler-shifted traveling waves; at these large tilt angles, the intensity-dependent distortion quickly disappears.

What most intrigued us about this asymmetry was the long list of variables on which it did not depend. The line shape for E1 transitions is independent of laser polarization, static electric field, and hyperfine transition ($\Delta F = \pm 1$ and 0). While the line shape remains the same as these conditions are changed, the transition rate per atom varies between 1 s^{-1} and 10^4 s^{-1}, corresponding to transition probabilities per atom between 10^{-6} and 10^{-2} for the entire interaction time. The simplest explanations cannot explain this complete insensitivity to the excitation rate.

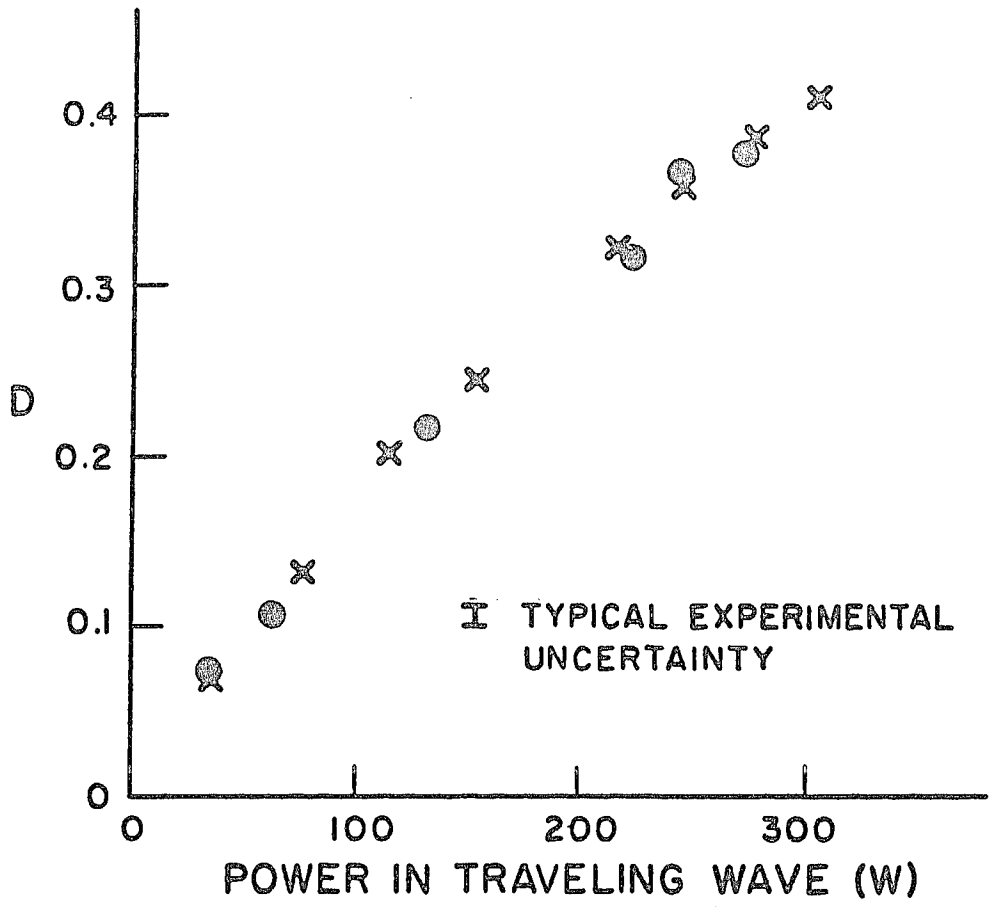

Fig.6–2. Fractional distortion D versus traveling wave power. The solid dots are experimental points and the ×'s are theoretical results.

The lineshape distortion is also independent of a number of other less fundamental variables. By applying the magnetic field, we can observe the transition rate from a single ground state m_F level to a single excited state m_F level; this shows the same distortion. Changing the cesium beam intensity and the sign of the wavefront curvature (which arises from the arrangement of the PBC mirrors) likewise has no effect. The line asymmetry also appears in the fluorescence emitted in the 7S→6P transition.

However, with the enormous laser fields we now have, we can observe the transition rate even when it is dominated by the tiny $M1^2$ rate term (i.e. when the E1 amplitude is eliminated by turning off the dc electric field). The first time we observed the $M1^2$ term, we were surprised to find that the line shape for the M1 transition is the mirror image of the line shape of the E1 transition. The rate is enhanced on the high frequency side and suppressed on the low frequency side of the line.

Using an imaging system we studied how the transition lineshape changes as the atoms cross through the laser beam. In this system, we used a cylindrical collector to image the interaction region onto a movable slit. The slit was 0.013 cm × 3 cm, and could be moved along the direction of the cesium beam to allow us to observe the atomic transitions occurring at various points along the cesium path. In Fig.6-3 we plot D (the size of the asymmetry) and the transition signal as a function of the position of the slit; this data was obtained at a cavity power of 290 W.

The rise in D far from the center is an artifact of the experiment and is not significant. In this region, the signal from

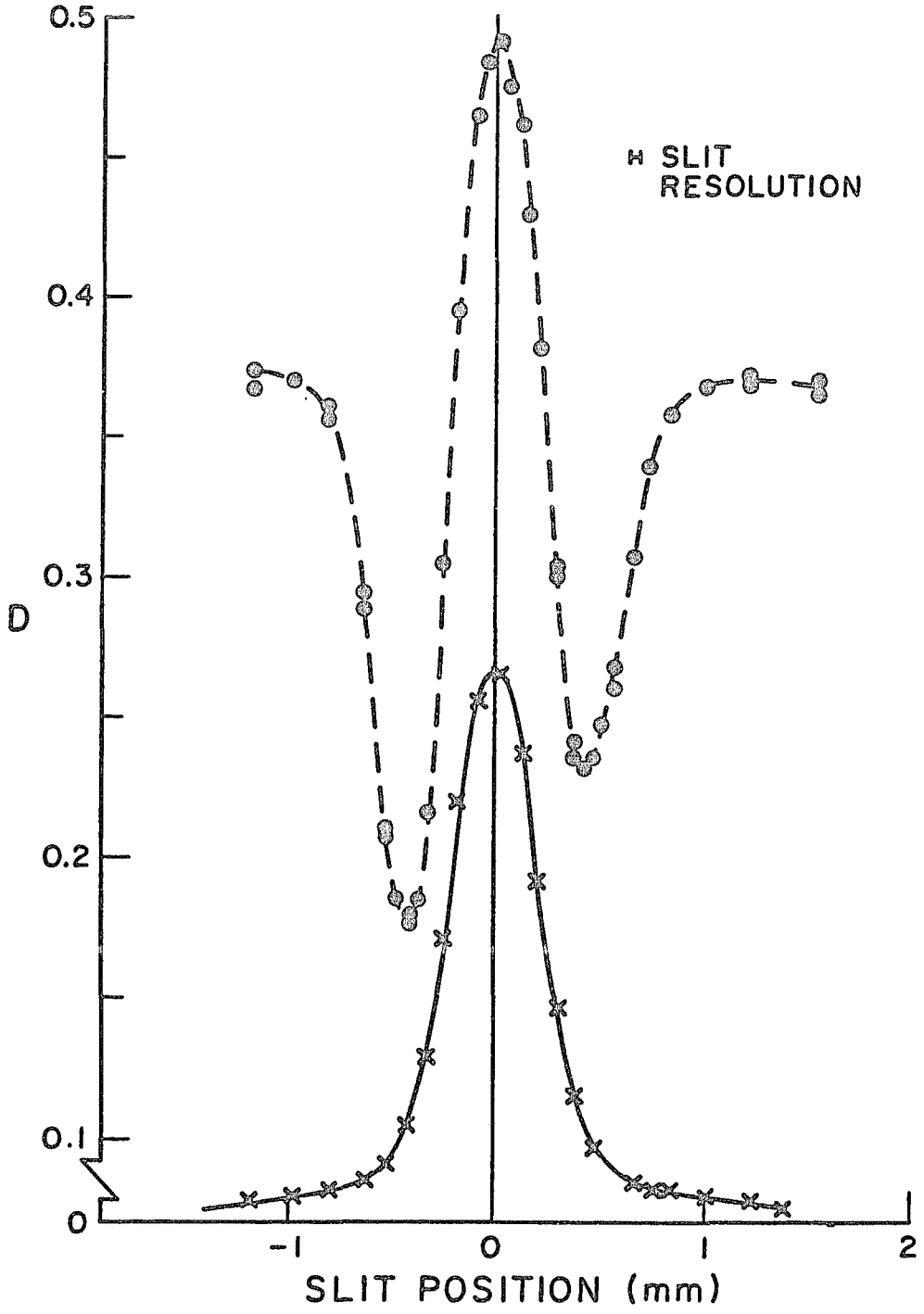

Fig.6–3. Fractional distortion D (dashed line) and transition signal versus imaging slit position.

the image falls below the level of the light scattered from the electric field plates; the resulting D value represents an average over the entire laser profile. We have used several different imaging systems with varying amounts of scattered light; in all cases, the same features appear in the center, and the data settles to the same value in the wings (although the wings begin at different places for each imaging system).

To first order, the distortion size D follows the curve of transition rate vs. slit position. On closer inspection, we see that the position of the maximum in D is slightly to the downstream side of the position of the maximum transition rate; furthermore, the final value of D (downstream) is slightly higher than the initial value. These features were consistent throughout our data. We were careful to ensure that these effects were not caused by optical pumping.

In Fig.6-4 we show the intensity dependence of D for three different positions of the slit. In all three curves, D initially rises linearly with intensity, but begins to deviate from linear at higher power, apparently indicating a saturation of the distortion.

The features of the line shape distortion are highly resistant to conventional explanations. The absorption of light by the atoms cannot affect the laser field since the absorption is between 10^{-8} and 10^{-12}. It cannot be a coherence of the m_F levels, since the effect was observed when the m_F levels were resolved in a magnetic field. It cannot be a conventional dipole force because that force is too small, and because its strength depends directly on the same

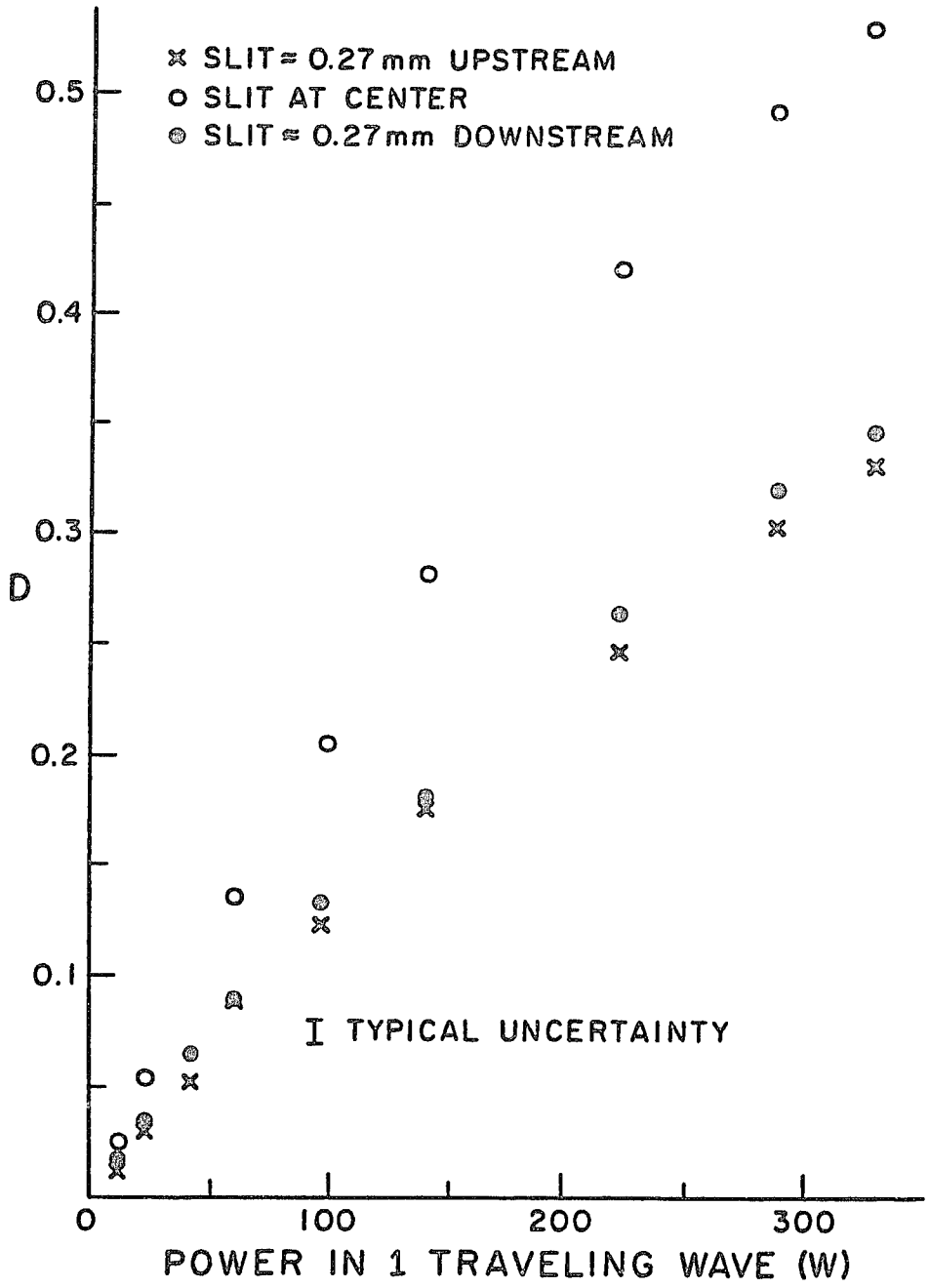

Fig.6-4. Fractional distortion D versus traveling wave power at three positions of the imaging slit.

dipole matrix element that determines the transition rate (on which the asymmetry does not depend).

6.2 Theory

Although the solution is somewhat subtle, these results can be explained by considering how the ac Stark shift in a standing wave affects the line shape. This Stark shift arises because the field couples both the 6S and 7S states with the P states of the atom. Since the coupling to all of the P states is far off resonance, the shift is essentially constant over our frequency range. Also it is independent of the polarization of the laser. Considering only the coupling to the P states with principal quantum numbers 6, 7, and 8, we calculate the ac Stark shift of the transition frequency to be $[6.8 \times 10^{-3}\ \mathrm{Hz/(V/cm)^2}]\cdot\epsilon^2$, or 21 $\mathrm{Hz\cdot cm^2/W}$ times the intensity in one traveling wave. There is an uncertainty in this result due to the contribution from higher states and errors in the calculated matrix elements, but we estimate that the result is accurate to within a few percent.

This shift was incorporated into the usual optical Bloch equations for a two-level system (see Appendix D) by simply replacing the frequency difference between the states, $(\nu_1 - \nu_2)$, by the Stark shifted difference, $(\nu_1 - \nu_2) + \delta(t)$. The ac Stark shift, $\delta(t)$, is proportional to $\epsilon^2\cos^2[k\cdot z(t)]$, where $z(t) = z_0 + v_z t$; z_0 is the initial position and v_z is the atomic velocity transverse to the laser wavefronts. Also ϵ still contains the Gaussian x and y dependence of the wavefront. We can neglect transitions to other

states in the system because the photoionization rate is much smaller than the 7S → 6P decay rate.[61]

We have solved the Bloch equations numerically to find the time-integrated population in the 7S state for an atom in the laser beam, as a function of laser frequency. The observed fluorescence is proportional to this population for constant velocity across the beam. The solution involves averaging over the distribution of transverse velocities and initial positions z_0 in the standing wave, while taking into account the Gaussian field distribution of $\epsilon(x,y)$ in the x–y plane. To simplify the solution, we assume that $\epsilon(x,y)$ is constant over distances in the x–y plane corresponding to that moved by an atom in an atomic lifetime, and that the atoms follow straight line trajectories. These assumptions are reasonably good since a typical atom takes more than 20 lifetimes to cross the laser beam and is only deflected by about 10^{-3} radians by the dipole force. The calculated line shapes, particularly the intensity-dependent distortions, agree very well with all our observations. Examples of this can be seen in Figs.6–1c and 6–2, in which the positions marked with an × have been calculated with no free parameters. The basic shape of the distortion matches surprisingly well with what we observe and the height matches to within the uncertainty of the calculated ac Stark effect. The calculated line shapes even reproduce subtle features in the difference curve such as the small difference in height between the positive and negative peaks and the slight power-dependent shift in the frequency at which the difference curve crosses through zero. We believe that the offset between the initial and final values of D as the atoms move through the laser

beam can be attributed to a small spatial redistribution of the atomic beam by the dipole force.

We can understand these results qualitatively by considering the relationship between the Doppler shift of an atom and the ac Stark shift it will have. If an atom has a large v_z it will move rapidly across the wavefronts of the standing wave. In one lifetime it will sample and thus average over many periods of the field, and hence of the ac Stark shift. The perturbed resonant frequency of this atom will then be the unperturbed energy difference shifted by the spatial average of the Stark shift. The spectrum for such an atom will be two Lorentzian peaks which have the natural linewidth and are Doppler-shifted symmetrically above and below the perturbed resonant frequency. All large velocities show similar behaviors; thus the wings of the line, which are due to these velocities, will be symmetric, and the shape of the wings (but not their central frequency) will be independent of the intensity.

For very low velocity atoms the spectrum is quite different. A slow atom's position is nearly constant during one lifetime ($z(t) \approx z_0$), so its resonant frequency will be shifted by the $\delta(t)$ determined by the field at that point in space. Because the high field regions have both the largest transition rate and the largest ac Stark shifts, the spectrum one obtains for a spatial average of such atoms is a single peak skewed toward the maximum value for $\delta(t)$. The combination of these two very different spectra for high and low velocity atoms results in the line shape we observe. The characteristic velocity that distinguishes between the high and low velocity regimes is the velocity at which an atom goes one wavelength

in a lifetime. At this velocity an atom will have a Doppler shift equal to the natural linewidth; this is why the characteristic frequency scale is the natural linewidth.

From this model it is also quite easy to understand the frequency dependence of the M1 transitions. In a standing wave the antinodes of the oscillating magnetic field occur at the position of the electric field nodes. This means the M1 transitions for low velocity atoms will occur primarily in regions of low electric field and hence the lineshape will be skewed toward small ac Stark shifts. Since this is just the opposite of the E1 case, the distortion of the line shape is reversed.

6.3 Conclusion

We have found that the simple case of a weak transition excited in a standing wave field does not have a symmetric line shape. The line shape has an intensity-dependent asymmetry with characteristics that are unlike previously observed distortions of spectral lines. However, these characteristics can be fully explained if one carefully considers the combined effects of the Doppler and ac Stark effects in a spatially varying laser field.

APPENDICES

APPENDIX A

$C_{Fm}^{F'm'}$ coefficients

$$C_{4m}^{4m} = \frac{+m}{4} \qquad C_{3m}^{3m} = \frac{-m}{4}$$

$$C_{4m\pm1}^{4m} = \pm \frac{1}{8}\sqrt{(5\pm m)(4\mp m)} \qquad C_{3m\pm1}^{3m} = \mp \frac{1}{8}\sqrt{(4\pm m)(3\mp m)}$$

$$C_{3m}^{4m} = \frac{\sqrt{16-m^2}}{4} \qquad C_{4m}^{3m} = \frac{\sqrt{16-m^2}}{4}$$

$$C_{3m\pm1}^{4m} = + \frac{1}{8}\sqrt{(3\mp m)(4\mp m)} \qquad C_{4m\pm1}^{3m} = - \frac{1}{8}\sqrt{(4\pm m)(5\pm m)}$$

$$C_{Fm+d}^{F'm} = -C_{F'm}^{Fm+d} \qquad C_{Fm}^{F'm} = C_{F'm}^{Fm}$$

$$C_{Fm}^{Fm} = g_F m \qquad C_{Fm+d}^{Fm} = \frac{g_F d}{2}\sqrt{(F+1+md)(F-md)}$$

$$C_{Fm}^{F'm} = \frac{+\sqrt{16-m^2}}{4} \qquad C_{Fm+d}^{F'm} = - \frac{g_F}{2}\sqrt{(F+1+fdm)(F+fdm)}$$

APPENDIX B

Power Buildup Cavity With Birefringence

This appendix contains a description of birefringence effects in systems with one or two birefringent elements, the equations that describe the laser fields in a PBC with birefringent mirror coatings, the basis for the $A_E \cdot A_M$ rate expressions in Appendix C, and the relationship between the tilted-collimator measurement and the normal M1 systematic term of Section 4.2.

B.1 General Birefringences

When a laser field with polarization $\vec{\epsilon}_1 \equiv \tilde{\epsilon}_x\hat{x} + \epsilon_z\hat{z}$ is incident on a birefringent plate with axes at some orientation θ, the emerging polarization vector ϵ_2 is

$$\begin{aligned}
\vec{\epsilon}_2 &= R(-\theta)\begin{pmatrix} 1 & 0 \\ 0 & e^{i\varphi} \end{pmatrix} R(\theta)\ \vec{\epsilon}_1 \\
&= \begin{pmatrix} 1 + \sin^2\theta(e^{i\varphi}-1) & -\sin\theta\cos\theta(e^{i\varphi}-1) \\ -\sin\theta\cos\theta(e^{i\varphi}-1) & 1 + \cos^2\theta(e^{i\varphi}-1) \end{pmatrix} \vec{\epsilon}_1 \\
&\cong r\vec{\epsilon}_1 + i\varphi r\begin{pmatrix} s^2 & -sc \\ -sc & c^2 \end{pmatrix} \vec{\epsilon}_1 \qquad \text{(B-1)}
\end{aligned}$$

where $s \equiv \sin\theta$, $c \equiv \cos\theta$, $R(\theta)$ is the coordinate rotation matrix, and φ, the magnitude of the birefringence, is taken to be small.

If there are two consecutive birefringent plates, we have

$$\vec{\epsilon}_2 = R(-\theta_1)\begin{bmatrix} 1 & 0 \\ 0 & e^{i\varphi_1} \end{bmatrix} R(\theta_1)\cdot R(-\theta_2)\begin{bmatrix} 1 & 0 \\ 0 & e^{i\varphi_2} \end{bmatrix} R(\theta_2)\ \vec{\epsilon}_1$$

$$\cong \begin{bmatrix} 1 & 0 \\ 0 & 1 \end{bmatrix}\epsilon_1 + i\varphi_1\begin{bmatrix} s_1^2 & -s_1c_1 \\ -s_1c_1 & c_1^2 \end{bmatrix}\epsilon_1 + i\varphi_2\begin{bmatrix} s_2^2 & -s_2c_2 \\ -s_2c_2 & c_2^2 \end{bmatrix}\epsilon_1$$

$$= (1+i\delta)\begin{bmatrix} 1 & 0 \\ 1 & 0 \end{bmatrix}\epsilon_1 + i\varphi_0\begin{bmatrix} s_0^2 & -s_0c_0 \\ -s_0c_0 & c_0^2 \end{bmatrix}\epsilon_1 \qquad \text{(B-2)}$$

where the new constants φ_0, θ_0, and δ are given by

$$\varphi_0^2 = \varphi_1^2 + \varphi_2^2 + 2\varphi_1\varphi_2 \cos 2(\theta_1-\theta_2)$$

$$\delta = \frac{\varphi_1 + \varphi_2 - \varphi_0}{2} \qquad \text{(B-3)}$$

$$\tan 2\theta_0 = \frac{\varphi_1 \sin 2\theta_1 + \varphi_2 \sin 2\theta_2}{\varphi_1 \cos 2\theta_1 + \varphi_2 \cos 2\theta_2}$$

This relation is valid for small φ. Thus the effect of two birefringent plates has essentially the same form as that of a single birefringent plate. The single-plate approximation is nearly exact ($\delta \approx 0$) for $\varphi_1 \gg \varphi_2$ or $\varphi_2 \gg \varphi_1$ or $\theta_1 = \theta_2 + n\pi/2$.

Let us consider the case of circularly polarized light incident on a birefringent plate. We can choose our x and z axes judiciously so that $\theta \equiv 0$. Then the emerging field is

$$\epsilon_2 = \begin{bmatrix} 1 & 0 \\ 0 & e^{i\varphi} \end{bmatrix}\begin{pmatrix} 1 \\ \pm i \end{pmatrix} = \begin{pmatrix} 1 \\ \pm i e^{i\varphi} \end{pmatrix} \qquad \text{(B-4)}$$

If we then analyze this light with a linear polarizer, we see the intensity as a function of the polarizer orientation ψ vary as

$$I(\psi) = \left|\sin\psi \pm ie^{i\varphi}\cos\psi\right|^2 = 1 \mp \sin 2\psi \cdot \sin\varphi \qquad \text{(B-5)}$$

There is a modulation of the intensity along the polarizer axis as the initial polarization reverses its helicity; it is a large effect, since it is linear in the angle φ. There are two important observations:

(1) This modulation did not appear in the polarization before the birefringent plate (by construction). Therefore if we wish to stabilize $\epsilon_z{}^2$ in front of the plate by monitoring $\epsilon_z{}^2$ after the plate, we will need to allow a modulation on the monitored intensity to account for this birefringent effect.

(2) The sign of the modulation (phase relative to the polarization flip) reverses when either the analyzing polarizer or the birefringence axes are rotated by 90° (changing ψ). Thus the modulation in intensity on any two orthogonal axes is equal and opposite. Furthermore, the modulation shows a sinusoidal dependence on the orientation of the birefringence axes. This behavior was helpful in locating the axes of the mirror coating birefringence in our earlier PNC measurement, when the coating birefringence was much larger; it is still the best way to null the systematic effects of a coating birefringence on the output mirror of the PBC (see Sections 4.2 and B.2).

If we add a second birefringent plate with orientation θ relative to the first, the polarization after the second is

$$I(\psi) = 1 \mp \varphi_2 \sin(2\theta + 2\psi) \mp \varphi_1 \cdot \sin 2\psi \qquad \text{(B-6)}$$

to first order in φ_1 and φ_2. It is important to note that the term $\varphi_1 \cdot \sin 2\psi$ appears in exactly the same way in Eq.B-5; that equation is still a valid expression for the field between the two plates.

The α ($\Delta F = 0$) and β ($\Delta F = \pm 1$) transition amplitudes essentially perform a linear polarization analysis of the resonating light along the x and z axes, respectively ($\alpha \sim (\vec{E} \cdot \vec{\epsilon})$ and $\beta \sim |\vec{E} \times \vec{\epsilon}|$). If we stabilize the x component of the light transmitted through the PBC and monitor the same polarization component <u>inside</u> the cavity using the $\Delta F = 0$ transition, we will not see any effect in the ΔP modulation of the transition signal from changes in the birefringences upstream from the PBC. Because the φ_1 term has the same sign in both expressions, the corresponding intensity modulation appears equally on the PBC transmitted light and the signal; but the intensity stabilization system compensates for that extra modulation by introducing a modulation of the total intensity sent into the PBC. (This does not eliminate the effects of φ_1: the overall modulation of the PBC input light doubles the modulation of the z component, which is not observed on the PBC transmission signal or the α transition signal).

B.2 Transition Amplitudes in the PBC

We start by calculating the laser electric and magnetic fields as a function of position y along the laser path:

$$\vec{\epsilon}(y) = \vec{\epsilon}_1 e^{iky} + \vec{\epsilon}_2 e^{-iky}$$
$$\vec{\mathcal{B}}(y) = \left[(+\vec{k}) \times \vec{\epsilon}_1\right] e^{iky} + \left[(-\vec{k}) \times \vec{\epsilon}_2\right] e^{-iky} \qquad \text{(B-7)}$$

where ϵ_1 is the electric field vector of the wave moving downstream (from the input coupler mirror to the high-reflectivity output mirror), and ϵ_2 is the electric field vector of the wave moving upstream. The relationship between these electric field vectors is completely determined by the quality of the reflection from the output mirror coating. We use a scalar reflectivity coupled with a birefringence (expressed as in Eq.B-1), and insert the resulting expression for ϵ_2 into Eq.B-7. This gives

$$\tilde{\epsilon}_x(y) = \cos ky\left[\tilde{\epsilon}_{x1}(1 + r + i\varphi rs^2) + \epsilon_{z1}(-i\varphi rsc)\right] \qquad \text{(B-8a)}$$
$$+ i \sin ky\left[\tilde{\epsilon}_{x1}(1 - r - i\varphi rs^2) + \epsilon_{z1}(i\varphi rsc)\right]$$

$$\tilde{\epsilon}_z(y) = \cos ky\left[\epsilon_{z1}(1 + r + i\varphi rc^2) + \tilde{\epsilon}_{x1}(-i\varphi rsc)\right] \qquad \text{(B-8b)}$$
$$+ i \sin ky\left[\epsilon_{z1}(1 - r - i\varphi rc^2) + \tilde{\epsilon}_{x1}(i\varphi rsc)\right]$$

$$\tilde{\mathcal{B}}_x(y) = i \sin ky\left[\epsilon_{z1}(1 + r + i\varphi rc^2) + \tilde{\epsilon}_{x1}(-i\varphi rsc)\right] \qquad \text{(B-8c)}$$

$$+ \cos ky\left[\epsilon_{z1}(1 - r - i\varphi rc^2) + \tilde{\epsilon}_{x1}(i\varphi rsc)\right]$$

$$\tilde{\mathcal{B}}_z(y) = i \sin ky\left[-\tilde{\epsilon}_{x1}(1 + r + i\varphi rs^2) - \epsilon_{z1}(-i\varphi rsc)\right] \qquad \text{(B-8d)}$$

$$+ \cos ky\left[-\tilde{\epsilon}_{x1}(1 - r - i\varphi rs^2) - \epsilon_{z1}(i\varphi rsc)\right]$$

We then use these expressions for $\vec{\epsilon}$ and $\vec{\mathcal{B}}$ to calculate A_E and A_M as given in Chapter 2:

$$A_E(y) = \alpha\left(\vec{E}\cdot\vec{\epsilon}(y)\right)\delta_{F,F'}\delta_{m,m'} + i\beta\left(\vec{E}\times\vec{\epsilon}(y)\right)_z C_{Fm}^{F'm}\delta_{m,m'}$$

$$+ i\beta\left[d\left(\vec{E}\times\vec{\epsilon}(y)\right)_x + i\left(\vec{E}\times\vec{\epsilon}(y)\right)_y\right]C_{Fm}^{F'm'}\delta_{m,m'+d} \qquad \text{(B-9)}$$

$$A_M(y) = M1\cdot\mathcal{B}_z(y)\cdot C_{Fm}^{F'm}\delta_{m,m'} + M1\left(d\mathcal{B}_x(y) + i\mathcal{B}_y(y)\right)C_{Fm}^{F'm'}\delta_{m,m'+d}$$

In the calculation of the interference term between $A_E(y)$ and $A_M(y)$ we find that the largest terms in the M1 amplitude are proportional to sin ky, whereas the largest terms in the E1 amplitude are proportional to cos ky. The spatial orthogonality of these two amplitudes is a direct consequence of the fact that the M1 amplitude changes sign as the laser propagation reverses.

The only E1·M1 rate terms which survive in an average over all y-positions in the standing wave are proportional to 1−r and φ. The final E1·M1 rates for all 6S→7S transition peaks are given in Appendix C.

The E1·M1 rate terms all contain one part proportional to (1−r) and one part proportional to ($\varphi \cdot \sin 2\theta$). The (1−r) term ostensibly comes just from the absorption, scattering, and transmission losses at the output mirror; however, this is only strictly true for the case of zero atomic Doppler shift and zero laser detuning. When we consider atoms with a Doppler shift interacting with a laser field that is detuned from the line center, the cancellation of the E1·M1 rate terms for each individual atom is no longer absolute. Then we must ensure that there are equal numbers of atoms with positive and negative E1·M1 contribution. The total contribution averaged over all atoms varies with the factor

$$R(\nu_L, \theta_T) = \int dv\ N(v, \theta_T) \left(\frac{1}{(\nu_L - kv)^2 + \Gamma^2/4} - \frac{1}{(\nu_L + kv)^2 + \Gamma^2/4} \right) \qquad (B\text{-}10)$$

where ν_L is the laser detuning, θ_T is the collimator tilt angle, kv is the Doppler shift of an individual atom, and $N(v, \theta_T)$ is the distribution of atomic Doppler shifts at a collimator tilt θ_T. The relative minus sign between the two terms in brackets is determined by the reversal of the E1·M1 term as the laser propagation direction is reversed.

We have calculated this integral numerically using a Gaussian velocity distribution as a reasonable approximation; collimator tilt was expressed as an offset of the center of the velocity distribution. We found that the calculated lineshapes for $R(\nu_L, \theta_T)$ as a function of ν_L are dispersion-shaped. In fact, they are well

approximated by the derivative of the Gaussian (dN/dv). The peak-to-peak size of this dispersion curve is proportional to the collimator tilt angle used; since the slope at the central zero-crossing is fairly constant, the functional form of $R(\nu_L, \theta_T)$ is approximately

$$R(\nu_L, \theta_T) \approx (\text{constant}) \frac{\nu_L}{\nu_D} \frac{\theta_T}{\theta_D} \qquad \text{for } \nu_L \ll \nu_D,\ \theta_T \ll \theta_D \qquad \text{(B-11)}$$

where ν_D and θ_D are the Doppler width and half-angle divergence of the cesium beam, respectively.

The smooth dispersion shape is not affected by the addition of the AC Stark shift (which causes the distortion of the $E1^2$ and $M1^2$ peaks at high laser intensity). However, the distortion does introduce a frequency offset between the peak of the $E1^2$ curve (the point to which the laser locks) and the zero-crossing of the E1·M1 dispersion curve. This offset allows an average E1·M1 contribution to appear which is proportional to the collimator tilt angle; at this point in the discussion, this E1·M1 term is not a PNC systematic, since polarization reversals have not been introduced. A discussion of the nulling of the E1·M1 contribution and the control of possible PNC systematic effects is given in Chapter 4.

The E1·M1 term proportional to φ is responsible for the so-called normal M1 systematic contribution to the PNC measurements. We can measure the factor $\varphi \cdot \sin 2\theta$ directly in the measurements taken with the collimator tilted far to one side (see Section 4.2). In this case, the transition peak splits into a doublet, with each peak corresponding to excitation of the atoms by one of the two travelling waves in the PBC. The two travelling waves are nearly identical in

polarization; the relationship is given by Eq.B–1, where the relevant birefringence is that of the output mirror coating. We use the $\Delta F = 0$ transition because of the simplicity of its transition rate contributions and because we can easily set a high transition amplitude, so that the main α rate term proportional to $(E_x \epsilon_x)^2$ heavily dominates (i.e. the small contributions from other rate terms are lost in the noise). We stabilize the x component of the PBC transmission. The difference in the ΔP modulation for the two peaks is then just the ϵ_x^2 modulation introduced by the birefringence of the output mirror (given by Eq.B–5): $\varphi \cdot \sin 2\theta$.

Since the ϵ_x^2 modulation from all birefringence sources preceding the PBC is regulated by the intensity stabilization system, the drift in those birefringences during the tilted-collimator measurement does not appear directly in the ΔP differences. Birefringences after the PBC can introduce a modulation into the transmission signal which is used to stabilize the PBC intensity; this leads to drift in the ΔP modulation of the overall intensity sent into the PBC, and hence a drift in the ΔP modulation of the transition signal.

B.3 Birefringence of a Resonant Cavity

When we treat the PBC including birefringence, we can use Eq.B–2 to write the round-trip birefringence in simpler form. We write the resonant field as an infinite sum of contributions from successive

round-trips of the photons:

$$\vec{\epsilon}_1 = \left\{1 + r_1 r_2\left[1 + i\delta + (e^{i\varphi}-1)M\right]e^{2ikL} + (r_1 r_2)^2\left[\cdots\right]^2 e^{4ikL} + (r_1 r_2)^3\left[\cdots\right]^3 e^{6ikL} + \cdots\right\} t_1\vec{\epsilon}_{in} \qquad \text{(B-12)}$$

$$= \left\{1 + \sum_{k=1}^{\infty} r^k\left[1 + i\delta + (e^{i\varphi}-1)M\right]^k\left[e^{2ikL}\right]^k\right\} t_1\vec{\epsilon}_{in}$$

where

$$M \equiv \begin{pmatrix} s^2 & -sc \\ -sc & c^2 \end{pmatrix} \quad \text{and} \quad r = r_1 r_2$$

and L is the distance between the mirrors. We can calculate the k^{th} power of the birefringence matrix to first order in φ and verify it by recursion:

$$\left[1 + i\delta + (e^{i\varphi}-1)M\right]^k = 1 + ki\delta + M(e^{ik\varphi}-1) + ki\delta M\left[e^{ik\varphi}e^{-i\varphi}-1\right] \qquad \text{(B-13)}$$

Then

$$\vec{\epsilon}_1 = \left\{ \frac{1}{1 - re^{2ikL}} + i\delta \frac{re^{2ikL}}{(1 - re^{2ikL})^2} \right.$$

$$+ M\left[\frac{re^{2ikL} e^{i\varphi}}{1 - re^{2ikL} e^{i\varphi}} - \frac{re^{2ikL}}{1 - re^{2ikL}} \right] \qquad \text{(B-14)}$$

$$\left. + i\delta M\left[\frac{re^{2ikL}}{(1 - re^{2ikL} e^{i\varphi})^2} - \frac{re^{2ikL}}{(1 - re^{2ikL})^2} \right] \right\} t_1 \vec{\epsilon}_{in}$$

On resonance, $e^{2ikL} = 1$; Then

$$\vec{\epsilon}_2 \cong \frac{F_0}{r} \left\{ 1 + i\delta F_0 - \frac{2\delta\varphi F_0^2}{(1 - i\varphi F_0)^2} \begin{pmatrix} s^2 & -sc \\ -sc & c^2 \end{pmatrix} \right. \qquad \text{(B-15)}$$

$$\left. + \frac{i\varphi F_0}{1 - i\varphi F_0} \begin{pmatrix} s^2 & -sc \\ -sc & c^2 \end{pmatrix} \right\} t_1 \vec{\epsilon}_{in}$$

where $F_0 \equiv \frac{r}{1-r} = \frac{F^* \sqrt{r}}{\pi}$ (F^* = cavity finesse)

This expression is similar to that in Eq.B-2, with the substitution of $F_0\varphi$ for the variable φ. Thus the effective birefringence of the resonant cavity is F_0 times the combined birefringence of the two mirrors. Since F^* is usually a large number, this means the birefringence effect is greatly enhanced.

We are oversimplifying when we say $e^{2ikL} = 1$, since the resonance is defined by the minimization of the denominator expression: in some cases $1 - re^{2ikL}$ and in others $1 - re^{i\varphi}e^{2ikL}$. The presence of the factor $e^{i\varphi}$ indicates that parts of Eq.B-15 are "on resonance" when others are slightly detuned. This is the origin of the birefringence detuning effect referred to in Section 3.7.

APPENDIX C

AMPLITUDE AND RATE CONTRIBUTIONS

Refer to Chapter 2 for the definition of symbols.

Stark Amplitudes

(C-1) $\Delta F = 0,\ \Delta m = 0$

$$A_E = \alpha\left[(bE_x+\Delta E_x)(\epsilon_R+ia\epsilon_I) + \Delta E_z\epsilon_z\right] + i\beta\left\{-(bE_x+\Delta E_x)\epsilon_z\left(\frac{cB_y+\Delta B_y}{cB}\right)\right.$$

$$- (bE_y+\Delta E_y)(\epsilon_R+ia\epsilon_I) + (bE_y+\Delta E_y)\epsilon_z\left(\frac{cB_x+\Delta B_x}{cB}\right)$$

$$\left. - \Delta E_z(\epsilon_R+ia\epsilon_I)\left(\frac{cB_y+\Delta B_y}{cB}\right)\right\} \times \left[C_{Fm}^{Fm} + cf(\delta_6+\delta_7)\left(C_{Fm}^{F'm}\right)^2\right] \delta_{m,m'}$$

(C-2) $\Delta F = 0,\ \Delta m = \pm 1$

$$A_E = \beta\left\{(bE_x+\Delta E_x)\epsilon_z + icd'(bE_y+\Delta E_y)(\epsilon_R+ia\epsilon_I)\left(\frac{cB_x+\Delta B_x}{cB}\right)\right.$$

$$- \Delta E_z(\epsilon_R+ia\epsilon_I) - (bE_y+\Delta E_y)(\epsilon_R+ia\epsilon_I)\left(\frac{cB_y+\Delta B_y}{cB}\right)$$

$$\left. + icd'(bE_y+\Delta E_y)\epsilon_z + (bE_x+\Delta E_x)\epsilon_z\left(\frac{B_x^2+2cB_x\Delta B_x}{B^2}\right)\right\} \times$$

$$\left[C_{Fm}^{Fm'} + cf\left(\delta_6 C_{Fm}^{F'm}C_{F'm}^{Fm'} + \delta_7 C_{Fm}^{F'm'}C_{F'm'}^{Fm'}\right)\right] \delta_{m,m'+cd'}$$

(C-3) $\Delta F = \pm 1,\ \Delta m = \pm 1$

$$A_E = \beta\Big\{(bE_x+\Delta E_x)\epsilon_z + icd'(bE_y+\Delta E_y)(\epsilon_R+ia\epsilon_I)\left(\frac{cB_x+\Delta B_x}{cB}\right)$$

$$- \Delta E_z(\epsilon_R+ia\epsilon_I) - (bE_y+\Delta E_y)(\epsilon_R+ia\epsilon_I)\left(\frac{cB_y+\Delta B_y}{cB}\right)$$

$$+ icd'(bE_y+\Delta E_y)\epsilon_z + (bE_x+\Delta E_x)\epsilon_z\left(\frac{B_x^2+2cB_x\Delta B_x}{B^2}\right)\Big\} \times$$

$$\left[C_{Fm}^{F'm'} + cf\left\{\delta_6 C_{Fm}^{F'm}C_{F'm}^{F'm'} - \delta_7 C_{Fm}^{Fm'}C_{Fm'}^{F'm'}\right\}\right]\ \delta_{m,m'+cd'}$$

(C-4) $\Delta F = \pm 1,\ \Delta m = 0$

$$A_E = \alpha\left[(bE_x+\Delta E_x)(\epsilon_R+ia\epsilon_I) + \Delta E_z\epsilon_z\right] \times \left[cf(\delta_6-\delta_7)C_{Fm}^{F'm}\right]\ \delta_{m,m'}$$

$$+ i\beta\Big\{-(bE_x+\Delta E_x)\epsilon_z\left(\frac{cB_y+\Delta B_y}{cB}\right) + (bE_y+\Delta E_y)\epsilon_z\left(\frac{cB_x+\Delta B_x}{cB}\right)$$

$$- (bE_y+\Delta E_y)(\epsilon_R+ia\epsilon_I) - \Delta E_z(\epsilon_R+ia\epsilon_I)\left(\frac{cB_y+\Delta B_y}{cB}\right)\Big\} \times$$

$$\left(C_{Fm}^{F'm}\right)\left(1 - cf\ C_{Fm}^{Fm}(\delta_6+\delta_7)\right)\ \delta_{m,m'}$$

Stark Rate Expressions

(C-5) $\Delta F = 0,\ \Delta m = 0$

$$\frac{R}{\alpha^2 E_x^2 |\tilde{\epsilon}_x|^2} = \left[1 + 2b\frac{\Delta E_x}{E_x} + 2b\frac{\Delta E_z}{E_x}\frac{\epsilon_R \epsilon_z}{|\tilde{\epsilon}_x|^2}\right] \times (2F+1)$$

$$+ 2\frac{\beta}{\alpha}\left\{-\left(1 + 2b\frac{\Delta E_x}{E_x}\right)\left(\frac{B_y}{B} + c\frac{\Delta B_y}{B}\right)\frac{a\epsilon_I \epsilon_z}{|\tilde{\epsilon}_x|^2} + b\frac{E_y}{E_x}\frac{\Delta E_z}{E_x}\frac{a\epsilon_I \epsilon_z}{|\tilde{\epsilon}_x|^2}\right.$$

$$\left. - \left(\frac{E_y}{E_x} + b\frac{\Delta E_y}{E_x}\right)\left(\frac{B_x}{B} + c\frac{\Delta B_x}{B}\right)\frac{a\epsilon_I \epsilon_z}{|\tilde{\epsilon}_x|^2}\right\} \times \left[cf(\delta_6+\delta_7)\cdot\sum_m \left(C_{Fm}^{F'm}\right)^2\right]$$

(C-6) $\Delta F = 0,\ \Delta m = \pm 1$

$$\frac{R}{\beta^2 E_x^2 \epsilon_z^2} = \left\{1 + 2b\frac{\Delta E_x}{E_x} - 2b\frac{\Delta E_x}{E_x}\frac{\epsilon_R}{\epsilon_z} - 2abcd'\frac{E_y}{E_x}\frac{\Delta E_z}{E_x}\frac{\epsilon_I}{\epsilon_z}\right.$$

$$- 2acd'\left(\frac{E_y}{E_x} + b\frac{\Delta E_y}{E_x}\right)\left(\frac{B_x}{B} + c\frac{\Delta B_x}{B}\right)\frac{\epsilon_I}{\epsilon_z} + 2\left(\frac{B_x^2}{B^2} + 2c\frac{B_x \Delta B_x}{B^2}\right)$$

$$\left. - 2\left(\frac{E_y}{E_x} + b\frac{\Delta E_y}{E_x}\right)\left(\frac{B_y}{B} + c\frac{\Delta B_y}{B}\right)\frac{\epsilon_R}{\epsilon_z}\right\} \times$$

$$\left[\sum_m \left(C_{Fm}^{Fm'}\right)^2 + 2cf\cdot\sum_m C_{Fm}^{Fm'}\left(\delta_6 C_{Fm}^{F'm} C_{F'm'}^{Fm'} + \delta_7 C_{Fm}^{F'm'} C_{F'm'}^{Fm'}\right)\right]$$

(C-7) $\Delta F = \pm 1, \quad \Delta m = \pm 1$

$$\frac{R}{\beta^2 E_x^2 \epsilon_z^2} = \Bigg[1 + 2b\frac{\Delta E_x}{E_x} - 2b\frac{\Delta E_z}{E_x}\frac{\epsilon_R}{\epsilon_x} - 2abcd'\frac{E_y}{E_x}\frac{\Delta E_z}{E_x}\frac{\epsilon_I}{\epsilon_z}$$

$$+ 2\left(\frac{B_x^2}{B^2} + 2c\frac{B_x \Delta B_x}{B^2}\right) - 2acd'\left(\frac{E_y}{E_x} + b\frac{\Delta E_y}{E_x}\right)\left(\frac{B_x}{B} + c\frac{\Delta B_x}{B}\right)\frac{\epsilon_I}{\epsilon_z}$$

$$- 2\left(\frac{E_y}{E_x} + b\frac{\Delta E_y}{E_x}\right)\left(\frac{B_y}{B} + c\frac{\Delta B_y}{B}\right)\frac{\epsilon_R}{\epsilon_z}\Bigg\} \times$$

$$\left[\left(C_{Fm}^{F'm'}\right)^2 + 2cf \cdot C_{Fm}^{F'm'}\left(\delta_6 C_{Fm}^{F'm} C_{F'm}^{F'm'} - \delta_7 C_{Fm}^{Fm'} C_{Fm'}^{F'm'}\right)\right]$$

(C-8) $\Delta F = \pm 1, \quad \Delta m = 0$

$$\frac{R}{\beta^2 E_x^2 \epsilon_z^2} = \left(\frac{\alpha}{\beta}\right)^2 \Bigg[\left(1 + 2b\frac{\Delta E_x}{E_x}\right)\frac{|\tilde{\epsilon}_x|^2}{\epsilon_z^2} + 2b\frac{\Delta E_z}{E_x}\frac{\epsilon_R}{\epsilon_z}\Bigg]\left(C_{Fm}^{F'm}\right)^2 (\delta_6 - \delta_7)^2$$

$$+ 2\frac{\alpha}{\beta}\Bigg\{-\left(1 + 2b\frac{\Delta E_x}{E_x}\right)\left(\frac{B_y}{B} + c\frac{\Delta B_y}{B}\right)\frac{a\epsilon_I}{\epsilon_z} + a\left(\frac{E_y}{E_x} + b\frac{\Delta E_y}{E_x}\right)\left(\frac{B_x}{B} + c\frac{\Delta B_x}{B}\right)\frac{\epsilon_I}{\epsilon_z}$$

$$+ ab\frac{E_y}{E_x}\frac{\Delta E_z}{E_x}\frac{\epsilon_I}{\epsilon_z}\Bigg\} \cdot \left(C_{Fm}^{F'm}\right)^2 \cdot cf(\delta_6 - \delta_7) \cdot \left(1 - cf \cdot C_{Fm}^{Fm}(\delta_6 + \delta_7)\right)$$

$$+ \Bigg\{\left(\frac{B_y^2}{B^2} + 2c\frac{B_y \Delta B_y}{B^2}\right) - 2\left(\frac{E_y}{E_x} + b\frac{\Delta E_y}{E_x}\right)\left(\frac{B_y}{B} + c\frac{\Delta B_y}{B}\right)\frac{\epsilon_R}{\epsilon_z}\Bigg\} \times$$

$$\left(C_{Fm}^{F'm}\right)^2 \left(1 - 2cf \cdot C_{Fm}^{Fm}(\delta_6 + \delta_7)\right)$$

Stark·M1 Interference

(C-9) $\Delta F = 0, \quad \Delta m = 0$

$$2\mathrm{Re}\langle A_E A_M^* \rangle = -4\alpha M1 \cdot bE_x \left[|\tilde{\epsilon}_{x1}|^2 (1-r) + a\epsilon_{I1}\epsilon_{z1}\varphi sc \right] \left(\sum C_{Fm}^{Fm} \right) = 0$$

(C-10) $\Delta F = \pm 1, \quad \Delta m = 0$

$$2\mathrm{Re}\langle A_E A_M^* \rangle = -4\alpha M1 \cdot bE_x \left[|\tilde{\epsilon}_{x1}|^2 (1-r) + a\epsilon_{I1}\epsilon_{z1}\varphi sc \right] \left(C_{Fm}^{F'm} \right)^2 |\delta_6 - \delta_7| cf$$

$$= |A_E|^2 \cdot \frac{-2M1}{\alpha E_x} \frac{bcf}{|\delta_6 - \delta_7|} \left((1-r) + a \frac{\epsilon_{I1}\epsilon_{z1}}{|\tilde{\epsilon}_{x1}|^2} \varphi sc \right)$$

(C-11) $\Delta F = 0, \quad \Delta m = \pm 1$

$$2\mathrm{Re}\langle A_E A_M^* \rangle = 4\beta M1 \cdot bE_x \cdot d \sum_m \left(C_{Fm}^{Fm'} \right)^2 \left(\epsilon_{z1}^2 (1-r) - a\epsilon_{I1}\epsilon_{z1}\varphi sc \right)$$

$$= |A_E|^2 \cdot \frac{2M1}{\beta E_x} \cdot bcd' \left((1-r) - a \frac{\epsilon_{I1}}{\epsilon_{z1}} \varphi sc \right)$$

(C-12) $\Delta F = \pm 1, \quad \Delta m = \pm 1$

$$2\mathrm{Re}\langle A_E A_M^* \rangle = 4\beta M1 \cdot bE_x \cdot dC_{Fm}^{F'm'} \left[\epsilon_{z1}^2 (1-r) - a\epsilon_{I1}\epsilon_{z1}\varphi sc \right]$$

$$= |A_E|^2 \cdot \frac{2M1}{\beta E_x} \cdot bcd' \left[(1-r) - a \frac{\epsilon_{I1}}{\epsilon_{z1}} \varphi sc \right]$$

Derivation of PNC Systematic Terms

1) The second term in the second line of Eq.C-7 is

$$- |A_E|^2 \, 2acd' \left(\frac{E_y}{E_x} + b\frac{\Delta E_y}{E_x}\right)\left(\frac{B_x}{B} + c\frac{\Delta B_x}{B}\right)\frac{\epsilon_I}{\epsilon_z}$$

The part proportional to $\Delta E_y/E_x$ and B_x/B flips with all four of our flipping variables a, b, c, and d'. This term appears in Eq.4-7.

2) The fourth term on the first row of Eq.C-7 is

$$- |A_E|^2 \, 2abcd' \frac{E_y}{E_x}\frac{\Delta E_z}{E_x}\frac{\epsilon_I}{\epsilon_z}$$

This term appears in Eq.4-8.

3) The second term in the second line of Eq.C-12 is

$$|A_E|^2 \, abcd' \frac{M1}{\beta E_x}\frac{\epsilon_{I1}}{\epsilon_{z1}} \varphi \sin 2\theta$$

This term appears in Eq.4-3.

4) The first term in this same expression is

$$bcd' \frac{2M1}{\beta E_x}(1-r)$$

The average value of the factor 1-r in the presence of Doppler shifts and laser detuning is given by Eq. B-10. For small values of laser detuning and collimator tilt, Eq. B-11 is a valid approximation.

Then we have

$$\text{bcd}' \frac{M1}{\beta E_x} \frac{\nu_L}{\nu_D} \frac{\theta_T}{\theta_D} \text{ (lineshape factor)} \qquad \text{(C-13)}$$

This expression gives the largest E1·M1 contribution, which flips with E, B, and m_F, but not with polarization. This is the contribution which normally gives us an indication of the alignment of the collimator.

Polarization imperfections as described in Sections 4.2 and B.1 can cause modulation of the intensity along z or x. If there is a modulation of the z intensity ($\Delta\epsilon_z^2$), this can lead to P-flip modulation of the expression in Eq.C-13. The portion that modulates with the polarization flip then modulates with a, b, c, and d', and thus is a PNC systematic (see Eq.4-2):

$$\text{abcd}' \frac{M1}{\beta E_x} \frac{\Delta\epsilon_z^2}{\epsilon_z^2} \frac{\nu_L}{\nu_D} \frac{\theta_T}{\theta_D} \text{(lineshape factor)}$$

5) The first term in the second line of Eq.C-10 is

$$|A_E|^2 \frac{-2M1}{\alpha E_x} \frac{bcf}{|\delta_6 - \delta_7|} (1-r)$$

But this A_E is the $\alpha E_x \epsilon_x$ amplitude rather than the $\beta E_x \epsilon_z$ amplitude. Since this systematic only occurs in our experiment when we are studying the "β" amplitude (and hence we are stabilizing ϵ_z^2), it is more relevant to refer this modulation to the main rate term on the

nearby $\Delta m = \pm 1$ peak. Scaling to this rate we have

$$|\beta E_x \epsilon_z|^2 \frac{-2M1}{\beta E_x} \frac{\alpha}{\beta} \frac{\epsilon_x^2}{\epsilon_z^2} \frac{bcf}{|\delta_6 - \delta_7|} (1-r) \qquad (C-14)$$

As discussed above, the factor 1-r is modified by Doppler shift and laser detuning; the resulting average value of this factor over the full Doppler distribution of the atoms is given by Eq.B-10. In the present case, the large Zeeman detuning of the $\Delta m = 0$ peak from the $\Delta m = \pm 1$ peak ($\Delta\nu = g_F \mu_B B$) requires the atoms to have equally large Doppler shifts in order to be excited at the $\Delta m = \pm 1$ laser frequency. Thus we are dealing with Doppler shifts that are large compared to the Doppler width of the transition peak. In this regime, Eq.B-11 no longer gives the correct dependence on laser detuning; however, the linear dependence on collimator tilt is still approximately correct.

We still can calculate a reasonable approximation to the frequency dependence of R, the integral in Eq.B-10. This type of calculation shows that the integral has a dispersion shape as a function of laser detuning; thus because the Zeeman detuning of the nearby $\Delta m = 0$ peak from the $\Delta m = \pm 1$ peak reverses as we tune from the one end of the Zeeman multiplet to the other, the factor R also changes sign. This amounts to an implicit m-flip in the 1-r factor (which can be represented as a factor d' in the rate term). Then we have

$$|\beta E_x \epsilon_z|^2 bcd'f \frac{-2M1}{\beta E_x} \frac{\alpha}{\beta} \frac{\epsilon_x^2}{\epsilon_z^2} \frac{1}{|\delta_6 - \delta_7|} \frac{\theta_T}{\theta_D} \text{ (lineshape factor)} \qquad (C-15)$$

Improper setting of the polarization can make the modulation of ϵ_x^2 large, as described above. Then there is a portion of Eq.C-15 which modulates with the polarization also. This gives a PNC-mimicking term

$$|\beta E_x \epsilon_z|^2 abcd'f \frac{-2M1}{\beta E_x} \frac{\alpha}{\beta} \frac{\Delta(\epsilon_x^2)}{\epsilon_z^2} \frac{1}{|\delta_6 - \delta_7|} \frac{\theta_T}{\theta_D} \text{ (lineshape factor)}$$

which appears in Eq.4-4.

APPENDIX D

LINESHAPE CALCULATIONS

Here we present the density matrix formulation of the calculation of the dependence of transition rate on laser frequency for the weak 6S→7S transition in a strong standing wave laser field.

We can define a projection operator $\hat{\rho}$ which finds the projection of any wave function onto a particular wave function ψ:

$$\hat{\rho} \equiv |\psi\rangle\langle\psi| = \sum_{mn} \rho_{mn} |m\rangle\langle n| \tag{D-1}$$

where the states $|m\rangle$ are the eigenstates of the zero-order hamiltonian. The time dependence of this operator is given by the usual formula

$$i\hbar \frac{d}{dt} \hat{\rho} = [H, \hat{\rho}] = [H_0, \hat{\rho}] + [H', \hat{\rho}] \tag{D-2}$$

The time dependence of the individual matrix elements ρ_{mn} is then

$$i\hbar\dot{\rho}_{mn} = \hbar(\omega_m - \omega_n^*)\rho_{mn} + \sum_k \left[H'_{mk}\rho_{kn} - \rho_{mk}H'_{kn} \right] \tag{D-3}$$

where H'_{mn} is the matrix element of the H′ operator between states $\langle m|$ and $|n\rangle$, and we allow ω_n to be complex, to allow for radiative decay of the state. In a three-state system such as ours, the equations

for the matrix elements ρ_{mn} become

$$\dot{\rho}_{11} = -\Gamma_1\rho_{11} + i\epsilon(t)\left[d_{10}\rho_{11}e^{-i\omega_\ell t} - \rho_{10}d_{01}e^{i\omega_\ell t}\right] \qquad (D-4a)$$

$$\dot{\rho}_{10} = -\frac{\Gamma_1}{2}\rho_{10} - i\omega_{10}\rho_{10} + i\epsilon(t)d_{10}e^{i\omega_\ell t}(\rho_{00} - \rho_{11}) \qquad (D-4b)$$

$$\rho_{10} = \rho_{01}^{*} \qquad (D-4c)$$

$$\dot{\rho}_{22} = -\Gamma_2\rho_{22} + \Gamma_1\rho_{11} \qquad (D-4d)$$

where state 0 is the ground state (e.g.6S), state 1 is the excited state (e.g.7S), and state 2 is the third state lying between them in energy (e.g.6P). Also, ω_ℓ is the laser frequency and $\epsilon(t)$ is taken to be a slowly-varying laser field amplitude (the amplitude-modulation envelope of the laser field). The diagonal matrix elements correspond to the density of atoms in a particular state. With the assumption that the excitation rate is low compared to the decay rate of the upper state (i.e. $\rho_{00}\approx 1$, $\rho_{11}\approx 0$), these equations are the optical Bloch equations. As the atom moves through the nodes and antinodes of the standing wave, $\epsilon(t)$ will vary sinusoidally at a frequency equal to the size of the Doppler shift. Now we must also insert the ac Stark shift of the levels by the laser field. Then Eq.D-4b becomes

$$\dot{\rho}_{10} + \left(\frac{\Gamma_1}{2} + i\omega_{10} + i\delta_S(t)\right)\rho_{10} = i\epsilon(t)d_{10}e^{-i\omega_\ell t} \qquad (D-5)$$

where $\delta_s(t)$, the Stark shift of the resonance frequency, varies in the same way that $\epsilon(t)$ does. Integrating this equation, we get

$$\rho_{10}(t) = \int_0^t dt' \left\{ \exp\left[-(\Gamma_1/2 + i\omega_{10})(t-t') + i\int_{t'}^t dt'' \delta_s(t'') \right] \times \right.$$

$$\left. i\epsilon(t') d_{10} e^{-i\omega_\ell t'} \right\} \qquad \text{(D-6)}$$

We use

$$\delta_s(t) \equiv -\Delta \cos^2(kx + kvt) \qquad \text{(D-7)}$$

$$\epsilon(t) \equiv \epsilon_0 \cos(kx + kvt),$$

where x is the atom's position in the standing wave and v is its velocity across the wavefronts. Then the integral of $\delta_s(t)$ is

$$\int_{t'}^t dt'' \delta_s(t'') = -\frac{\Delta}{2}\left[(t-t') + \frac{\sin(2kx+2kvt) - \sin(2kx+2kvt')}{2kv} \right] \qquad \text{(D-8)}$$

This quantity, when placed in the exponent in Eq.D-6, makes that integral quite intractable. That integral (Eq.D-6) was performed numerically to verify that the properly calculated line shapes were indeed quite similar to the experimentally observed line shapes.

We can also make certain simplifications that allow us to proceed further in this calculation and derive a simpler algorithm for calculating the line shape; this result is less trustworthy, but still gives quite good results, and allows much easier qualitative understanding. When we look at Eq.D-6, we see that the $\Gamma_1/2$ term in the exponential effectively causes the integral to cut off at

$(t-t')\Gamma_1/2 \approx 1$. If we take the step of cutting off the integral of $\delta_s(t")$ in the same way, we can substitute a simpler expression into the exponential in Eq.D-6:

$$\int_{t'}^{t} dt"\delta_s(t") \rightarrow -(t-t')\cdot\Delta\cdot G(x,v) \tag{D-9}$$

where

$$G(x,v) \equiv \frac{\int_0^\infty \cos^2(kx+kvt)e^{-(\Gamma_1/2)t}\,dt}{\int_0^\infty e^{-(\Gamma_1/2)t}\,dt} \tag{D-10}$$

$$= \frac{1}{2}\left[1 + \frac{\cos 2kx - (4kv/\Gamma_1)\sin 2kx}{1 + (4kv/\Gamma_1)^2}\right]$$

Then the quantity $-\Delta\cdot G(x,v)$ is just another frequency offset which happens to depend on the position and velocity of the atom. The function $G(x,v)$ can be interpreted as the proportional to the average intensity seen by an atom in one atomic lifetime; thus it is also proportional to the average ac Stark shift and transition rate in one lifetime.

The limit of the expression in Eq.D-9 for $v\rightarrow 0$ is the same as for the original integral Eq.D-8:

$$\lim_{v\rightarrow 0}\int_{t'}^{t} dt"\delta_s(t") = \lim_{v\rightarrow 0}\left[-(t-t')\Delta G(x,v)\right] = -\Delta(t-t')\cos^2 kx \tag{D-11}$$

With this simplification, we can integrate Eq.D-6 to get

$$\rho_{11}(t) = |d_{10}|^2\epsilon_0^2\left\{\left[\frac{1}{(\Gamma_1/2)^2+(\Delta\omega+kv)^2} + \frac{1}{(\Gamma_1/2)^2+(\Delta\omega-kv)^2}\right]\right. \qquad \text{(D-12)}$$

$$\left. + \mathrm{Re}\left[\frac{e^{2i(kx+kvt)}}{\Gamma_1+2ikv}\left(\frac{\Gamma_1+2ikv+2i\Delta\omega}{(\Gamma_1/2)^2+(\Delta\omega+kv)^2} + \frac{\Gamma_1+2ikv-2i\Delta\omega}{(\Gamma_1/2)^2+(\Delta\omega-kv)^2}\right)\right]\right\}$$

where $\Delta\omega \equiv \omega_{10} - \omega_\ell - \Delta G(x,v)$. Recall that the time average of ρ_{11} (the excited state density) is proportional to the observed fluorescence. In this expression, we still have rapid variations in ρ_{11} (in exp[2ikx+2ikvt]), which we must average over in order to get the observed fluorescence. Since Eq.D-4d shows that decay from state 1 into state 2 (on the way back down to state 0) occurs on a time scale characterized by the decay constant Γ_1, it is appropriate to average the fast variations in ρ_{11} in the same way that we averaged the Stark shift $\delta_S(t)$. Thus we can write $\langle\rho_{11}\rangle$ in terms of G(x,v):

$$\frac{\langle\rho_{11}\rangle}{|d_{10}|^2\epsilon_0^2} = \frac{2G(x,v)}{(\Gamma_1/2)^2+(\Delta\omega+kv)^2} + \frac{2G(x,v)}{(\Gamma_1/2)^2+(\Delta\omega-kv)^2} \qquad \text{(D-13)}$$

$$+ \frac{\Delta\omega\cdot[2G(x+x',v)-1]}{\left[\Gamma_1^2 + (2kv)^2\right]^{1/2}}\left[\frac{1}{(\Gamma_1/2)^2 + (\Delta\omega+kv)^2} - \frac{1}{(\Gamma_1/2)^2 + (\Delta\omega-kv)^2}\right]$$

where again $\Delta\omega \equiv \omega_{10} - \omega_\ell - \Delta G(x,v)$. Note that the factor G(x,v) appears both in the numerator and inside the Lorentzian factors in each expression. This feature causes the asymmetry in lineshapes calculated using this method.

We found very satisfying line shapes when we integrated the first two terms over x and v, using a Gaussian velocity distribution as a reasonable first approximation to the observed distribution. A similar calculation of the line shape of the E1·M1 term shows that the spatially varying terms in the E1·M1 calculation (which would cause a distortion of that line shape) drop out altogether; thus the E1·M1 lineshape is undistorted. A calculation of the $M1^2$ term uses the same G(x,v) to express the ac Stark shift of the transition frequency, but uses a different G'(x,v) calculated with $\sin^2[y(t)]$ in place of $\cos^2[y(t)]$. The resulting $M1^2$ curve shows the opposite distortion.

REFERENCES

REFERENCES

1. S. L. Glashow, Nucl. Phys. 22, 579 (1961); S. Weinberg, Phys. Rev. Lett. 19, 1264 (1967); A. Salam, Elementary Particle Physics, N. Svartholm, ed. (Almqvist and Wiksell, Stockholm, 1968),p. 368

2. G. Arnison et al., Phys. Lett. 122B, 103 (1983); M. Banner et al., Phys. Lett. 122B, 476 (1983); G. Arnison et al., Phys. Lett. 126B, 398 (1983)

3. F. J. Hasert et al., Phys. Lett. 46B, 121 (1973)

4. C. Y. Prescott et al., Phys. Lett. 84B, 524 (1979)

5. M. A. Bouchiat and C. Bouchiat, J. Phys. (Paris) 35, 899 (1974); 36, 493, (1975)

6. U. Amaldi et al., Phys. Rev. D 36, 1385 (1987)

7. W. J. Marciano and A. Sirlin, Phys. Rev. D 27, 552 (1983)

8. R. R. Lewis and W. L. Williams, Phys. Lett. 59, 70 (1975)

9. R. W. Dunford, R. R. Lewis, and W. L. Williams, Phys. Rev. A 18, 2421 (1978)

10. M. A. Bouchiat et al., Opt. Commun. 56, 100 (1985); 62, 97 (1987)

11. J. Sapirstein, private communication (1987)

12. P. E. G. Baird et al., and E. N. Fortson et al., Nature (London) 264 (1976) p. 528. These results were described as preliminary; strong systematic effects were noted.

13. L. L. Lewis et al., Phys. Rev. Lett. 39, 795 (1977)

14. G. A. Apperson, Ph.D. Thesis (University of Washington, Seattle, 1979)

15. J. H. Hollister et al., Phys. Rev. Lett. 46, 643 (1981)

16. E. N. Fortson and L. L. Lewis, Physics Reports 113, 289 (1984)

17. M. J. Macpherson et al., 1987 (to be published)

18. P. E. G. Baird et al., Phys. Rev. Lett. 39, 798 (1977)

19. P. E. G. Baird et al., Proc. VII Vavilov Conf., Novosibirsk, S. G. Routian, ed. (1982) Part 1, p. 22

20. J. D. Taylor et al., 1987 (to be published)

21. L. M. Barkov and M. S. Zolorotev, JETP Lett. 28, 521 (1978)

22. L. M. Barkov, I. B. Khriplovich, and M. S. Zolorotev, Comments At. Mol. Phys. 8, 79 (1979)

23. L. M. Barkov and M. S. Zolorotev, JETP 52, 360 (1980)

24. Yu. V. Bogdanov et al., JETP Lett. 31, 214 and 522 (1980)

25. G. N. Birich et al., JETP 60, 442 (1984)

26. T. P. Emmons et al., Phys. Rev. Lett. 51, 2089 (1983)

27. R. Conti et al., Phys. Rev. Lett. 42, 343 (1979)

28. E. Commins et al., Phys Rev. Lett. 46, 640 (1981)

29. P. S. Drell and E. D. Commins, Phys. Rev. Lett. 53, 968 (1984)

30. M. A. Bouchiat et al., Phys. Lett. 117B, 358 (1982)

31. M. A. Bouchiat et al., Phys. Lett. 134, 463 (1984)

32. M. A. Bouchiat et al., J. Phys. (Paris) 47, 1709 (1986)

33. S. L. Gilbert, M. C. Noecker, R. N. Watts, and C. E. Wieman, Phys. Rev. Lett. 55 (1985) 2680

34. S. Chu, E. D. Commins, and R. Conti, Phys. Lett. A 60, 96 (1977)

35. C.Tanner, PhD. Thesis (University of California, Berkeley, 1985)

36. C. E. Loving and P. G. H. Sandars, J. Phys. B 8, L336 (1975)

37. D. V. Neuffer and E. D. Commins, Phys. Rev. A 16, 1760 (1977)

38. B. P. Das et al., Phys. Rev. Lett. 49, 32 (1982)

39. C. Bouchiat, C. A. Piketty, and D. Pignon, Nucl. Phys. B 221, 68 (1983)

40. V. A. Dzuba et al., Phys. Scr. 36, 69 (1987)

41. W. R. Johnson et al., to be published

42. C. Bouchiat and C. A. Piketty, Europhys. Lett. 2, 511 (1986)

43. Z. W. Liu and W. R. Johnson, Phys. Lett. A 119, 407 (1987)

44. J. Hoffnagle et al., Phys. Lett. 85A, 143 (1981)

45. S. L. Gilbert, R. N. Watts, and C. E. Wieman, Phys. Rev. A 27, 581 (1983)

46. M. A. Bouchiat et al., Opt. Commun. 45, 35 (1983)

47. V. V. Flambaum, I. B. Khriplovich, and O. P. Sushkov, Phys. Lett. 67A, 177 (1978)
48. J. Hoffnagle et al., Phys. Lett. 85A, 143 (1981)

49. S. L. Gilbert, Ph.D. Thesis (University of Michigan, Ann Arbor, 1984)

50. J. Hoffnagle, dissertation (Swiss Federal Institute of Technology, Zurich, 1982)

51. Our capillary arrays are supplied by Galileo Electro-Optics Corp.

52. Hughes product data

53. R. W. P. Drever et al., Appl. Phys. B 31, 97 (1983); R. V. Pound, Rev. Sci. Instrum. 17, 490 (1946)

54. T. W. Hänsch and B. Couillaud, Opt. Commun. 35, 441 (1980)

55. EG&G sales literature

56. V. N. Novikov et al., Sov. Phys. JETP 46, 420 (1977)

57. P. A. Frantsuzov and I. B. Khriplovich, Z. Phys. D 7, 297 (1988)

58. L. S. Durkin and P. Langacker, Phys. Lett. B 166, 436 (1986), and V. Barger, N. W. Deshpande, and K. Whisnant, Phys. Rev. Lett. 56, 30 (1986)

59. W. J. Marciano, to be published.

60. M. G. Prentiss and S. Ezekiel, Phys. Rev. Lett. 56, 46 (1986)

61. S. L. Gilbert, M. C. Noecker, and C. E. Wieman, Phys. Rev. A 29, 3150 (1984)